TECHNISCHE UNIVERSITÄT MÜNCHEN
Lehrstuhl für Zellbiophysik E27

Structure, Mechanics and Dynamics of Cytoskeletal Model Systems

Christine Wurm

Vollständiger Abdruck der von der Fakultät für Physik der Technischen Universität München zur Erlangung des akademischen Grades eines

Doktors der Naturwissenschaften (Dr. rer. nat.)

genehmigten Dissertation.

Vorsitzender: Univ.-Prof. Dr. M. Zacharias

Prüfer der Dissertation:
1. Univ.-Prof. Dr. A. Bausch
2. Univ.-Prof. Dr. J. O. Rädler, Ludwig-Maximilians-Universität München

Die Dissertation wurde am 30.03.2011 bei der Technischen Universität München eingereicht
und durch die Fakultät für Physik am 28.04.2011 angenommen.

Abstract

The precise adjustment of the structural and, thus, mechanical properties of living cells is essential for their functionality. These properties are mainly attributed to the cytoskeleton, a complex polymer network spanning the cytosol. Main constituents are the semiflexible actin filaments and numerous actin binding proteins (ABPs) which organize the filaments into a variety of higher order structures, ranging from networks of homogeneously crosslinked filaments to networks of small bundles of well-defined size or even very thick bundles and clusters build of hundreds of filaments.

The present work explores some remarkable mechanical and structural features of the actin network using *in vitro* actin model systems. The first series of experiments addresses the question of size control in actin bundles. *In vivo*, the functionality of cells relies on a tight control of cytoskeletal structures which is obtained by a fine tuning of the ABPs. Each cellular process features its individual set of ABPs resulting in a well-defined bundle width, optimized for this process. The size limiting mechanism remains elusive. *In vitro*, microscopy experiments revealed a finite size of reconstituted actin bundles formed by the ABP fascin. Motivated by these findings, small angle X-ray scattering experiments (SAXS) are performed on actin/fascin and actin/espin bundles to explore the microscopic structure of the bundles. It is shown that the filaments are arranged on a hexagonal lattice. Moreover, the SAXS data reveals an overtwist of the individual filaments in the bundle to adapt the helical symmetry of the filaments to the hexagonal arrangement in the bundle. The mismatch between the native actin helix and the hexagonal packing is discussed as a possible size limiting mechanism. Furthermore, a combination of different ABPs is shown to build larger bundle structures as observed *in vivo*.

The dynamic properties of the actin cytoskeleton are in the focus of the second part of the thesis. The tight control of assembly and disintegration of actin structures is an essential feature of cellular processes as e.g. cell migration. While various proteins are known to accelerate the polymerization or disintegration of actin filaments, the insight in the mechanisms guaranteeing the kinetic stability of the cytoskeletal structures remains relatively scarce. Multiple depolymerization methods demonstrate that crosslinking and bundling proteins effectively suppress actin depolymerization in a concentration dependent manner. Even the actin depolymerizing factor cofilin is not sufficient to facilitate a fast disintegration of highly crosslinked actin networks unless aided by molecular motors. This is postulated to be a generic effect for all ABPs which bind at least to two actin subunits. The presented results indicate that crosslinking ABPs do not only guarantee for the mechanical stability of a cell but also provide a powerful tool to stabilize distinct actin structures.

A third series of experiments addresses the mechanical properties of actin networks subjected to large external forces. It has been proposed that cells harness the nonlinear

response of the semiflexible actin network to rapidly adapt their local properties. The underlying physical mechanisms of the nonlinear response is still elusive. The simplest model system with yet challenging complexity is a purely entangled actin solution. Using a variety of different macro-rheological techniques, this work characterizes the nonlinear response of such systems. In contrast to previous publications, the nonlinear response is not found to be described by a universal power law determined by the entropic stretching of the filaments. Rather, a continuous transition from a regime of stress hardening to stress weakening is reported, dependent on various network parameters like temperature, salt concentration or filament length. These results are discussed and qualitatively explained by the recently introduced glassy worm-like chain model.

Cytoskeletal networks exhibit an enormous wealth of features in structure and dynamics. The combination of the different experimental approaches covering all the relevant length and time scales presented in this thesis allows the investigation of the underlying principles governing cytoskeletal processes. Further, reconstituted actin networks can not only help to unravel the complexity of cellular organization but may also serve as a model system for self-organizing systems.

Contents

Chapter 1

Introduction

The cytoskeleton of eukaryotic cells is a complex polymer network which maintains the shape of the cell like a scaffold. Beyond the simple determination of the cell morphology, it provides mechanical stability and integrity when an external force is exerted. Furthermore, it plays an important role in dynamical processes as cell motility, cell division or even intracellular transport, to state just a few of its most prominent tasks. The basic modules of the cytoskeleton are three major classes of biopolymers: intermediate filaments, microtubuli and actin. The actin network governs the mechanical properties of the cell to a large extent. This present work is centered on its experimental characterization.

Besides these basic polymers, there exists a myriad of accessory proteins which organize the filaments into higher order structure. The broad range of requirements to the cytoskeleton is matched by the diversity of these "helper molecules": they can crosslink, bundle, sever, cap, branch or stabilize the filaments and also anchor them to other cellular structures as the plasma membrane. Dependent on the combination of the attached actin binding proteins (ABPs), the network assumes very different shapes as depicted in fig. 1.1: stress fibers are embedded in the actin cortex spanning through the cell, the lamellipodium forms a two-dimensional dense network at the leading edge of the cell while spike-like structures as microvilli, stereocilia or filopodia protrude the cellular membrane.

The variety of actin structures relies on a fine tuning of the ABPs; each cellular process features its individually adjusted set of proteins [1]. The mechanical properties of actin bundles are modulated by a change of crosslinker type or concentration. However, the question remains how the cell develops the morphology of these structures *in vivo*. What mechanism does control the well-defined lengths or thicknesses of these bundle structures? Loss of one of the ABPs usually affects either the organization or the thickness of the bundles [2, 3]; mutations often result in diseases [4, 5].

Actin structures are not stable over time. Opposing to the term "skeleton" the cytoskeleton is not a fixed scaffold but highly dynamic. This corresponds to the need of the cytoskeleton not only to guarantee for mechanical stability but also to allow for a morphological reorganization during cell movement or division. In this, the dynamic properties of the cytoskeletal filaments are of particular importance. Assembly and decomposition of cytoskeletal structures are ever on-going, while stress bearing elements stay intact.

These conflicting demands reflect the complexity of the cytoskeleton: The network must not be a rigid frame to fulfill the dynamic needs of the cell but it has to be able to

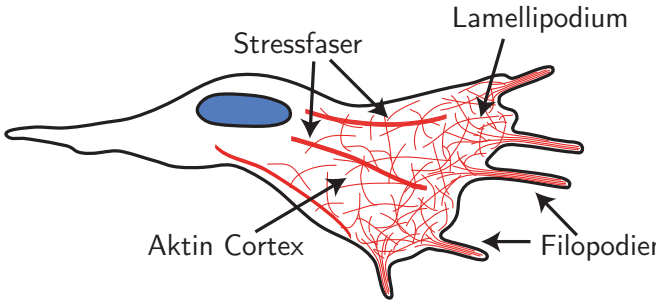

Figure 1.1: Schematic representation of different cellular actin structures: Stress fibres are antiparallel bundles spanning the cell. They are embedded in the actin cortex, a homogenously crosslinked network which provides mechanical support for the plasma membrane. At the leading edge of the cell, the lamellipodium forms a dense, two-dimensional network. Filopodia are parallel actin bundles which extend beyond the lamellipodium, protruding the cell membrane.

withstand external forces without disrupting it. This cushioning of sudden mechanical impacts is assured by a combination of elastic stiffening and viscoplastic kinematic hardening [6]. Former investigations have shown that prestressed actin networks reflect these mechanical properties [7]. However, the precise molecular mechanism underlying this stiffening could not be identified.

A common strategy for tracing back the diverse features of the cytoskeleton to the properties of its elementary constituents is to reassemble the system step by step from simpler subunits [8]. This *in vitro* reconstitution of the actin cytoskeleton is an important step towards systematic and quantitative studies of cell organization. The type and concentrations of the ABPs and the filament density can be tuned independently from each other. The approach allows to investigate one by one how biochemical or physical parameters like the salt concentration or ambient temperature influence the biophysical properties of cytoskeletal networks. Hence, functional modules of increasing complexity are adequate model systems promoting the understanding of living matter.

This work explores some remarkable features of the actin network using *in vitro* actin model systems. First, the actin and the related proteins used in this work are introduced briefly (chapter 2). Chapter 3 gives a short theoretical introduction to the diffraction on helical molecules. This technique is used in chapter 4 to analyze the microscopic structure of actin bundles to address the question of size limiting mechanisms in actin bundles. In chapter 5, the influence of ABPs on the depolymerization kinetics of actin filaments is investigated. The mechanical properties in the nonlinear regime of entangled actin solutions are in the focus of chapter 6. Using a variety of different rheological approaches, it is shown that the nonlinear response is very sensitive to experimental conditions including temperature, actin and salt concentration, and even filament length. The outlook in chapter 7 demonstrates that *in vitro* actin networks are not only a powerful tool to gain insights in cellular mechanisms but are a well-suited model system for other physical objectives, e.g. self-organizing processes.

Chapter 2

Materials

Actin is the key component in the cell cortex and the cytoskeleton and therefore an essential element for structural and mechanical processes in eukaryotic cells. A large number of actin binding proteins effect the structural organization as well as the polymerization kinetics of actin filaments. This chapter gives a short overview of the most important properties and functions of actin (sec. 2.1) and the actin binding proteins (sec. 2.2) used in this work. Furhermore, a section on preparation and storage of the individual molecules completes the chapter (sec. 2.3).

2.1 Actin

Actin, one of the principal components of the cytoskeleton, is the most abundant intracellular protein in eukaryotic cells. Monomeric actin is a globular protein (G-actin) with a molecular weight of 42 kDa (Fig. 2.1(a)). In the presence of adequate salt conditions actin can polymerize above the critical concentration c_{crit} into helical filaments (F-actin). The polymerized actin filament has a linear charge density of $\lambda_A \approx -4\,\mathrm{e/nm}$ [9].

The structure of the F-actin helix could so far not be resolved on an atomic level. However, it was possible to crystalize monomeric actin and its atomic structure could be determined [10]. In fiber diffraction experiments it was possible to derive a model of the F-actin helix based on the monomeric crystal structure [11]. The F-actin filament was modeled as a helical arrangement of unperturbed G-actin monomers. The model was fitted to fiber-diffraction data by varying the helical symmetry, monomer spacing, three-dimensional monomer orientation and monomer radial position. The native F-actin helix was thus determined to have a monomer distance of 27.6 nm and a helical symmetry of -13/6 , i.e. the structure repeats exactly after 6 turns and 13 monomers [11]. The negative sign indicates a left-handed helix. As the offset angle is approximately 166°, the filament appears as two right-handed steep helices which twine slowly around each other (Fig. 2.1(b)). Recently, it was possible to derive a high resolution structure of an actin filament using X-ray fiber diffraction intensities obtained from highly oriented F-actin solutions [12]. It revealed that the monomer flattens in the transition to the filamentous state due to a rotation of two subdomains. Thus, the filament diameter is smaller than in the original Holmes model, but quite close to recently revised models [13]. The determined symmetry of -331/153 is in very good agreement with the former model.

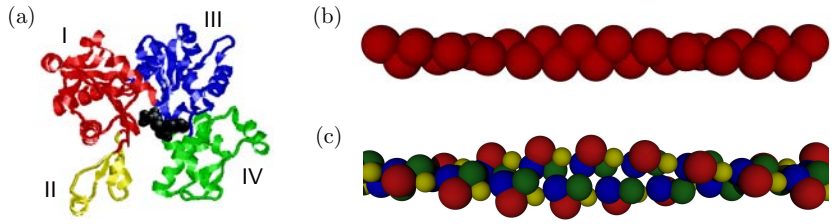

Figure 2.1: (a) Crystal structure of the G-actin monomer [14]. The four domains are labeled, the bound ADP is colored black. (b) Simple model of the actin filament (c) 4-bead model of the actin filament. The four different spheres correspond to the four domains in the actin monomer as indicated in (a).

actin domain	radius of gyration a[nm]	helical radius r[nm]	offset angle ψ[°]	pitch along helical axis z[nm]
I	1.681	2.833	56.92	0.879
II	1.053	2.142	69.85	3.252
III	1.492	1.380	0	0
IV	1.426	1.510	-34.41	2.358

Table 2.1: Coordinates of the 4-bead model according to [15]

Certainly, it would be very complex to model the diffraction pattern of a 42 kDa protein on the level of individual atoms. A widely-used simplification is the 4-bead model of Al-Khayat *et al.* [15], where each subdomain of the actin monomer is modeled by a solid sphere (Fig. 2.1(a) and (c)). The size of each sphere is determined by the radius of gyration, and the position corresponds to the center of mass calculated from the Holmes atomic model. The coordinates and radii are listed in table 2.1.

Due to the orientation of the monomers in the filament, actin filaments are polar. Hence, the assembly kinetics are different at the two ends; the faster growing end is called barbed or plus end, while the other one is called pointed or minus end. The critical concentration under ATP conditions is lower at the plus end than at the minus end; the exact value is highly dependent on the buffer salt concentration and is in the range of $c_{\mathrm{crit}} = 0.1 - 3\,\mu\mathrm{M}$ for the plus end [16]. At intermediate monomer concentrations between the critical concentration of the two ends, the plus end grows while the minus end shrinks. The steady-state at which the speed of growth at the plus end is the same as the shrinkage at the minus end is termed treadmilling, a process driven by a continuous ATP hydrolysis. This dynamic behavior of actin filaments (and the whole cytoskeleton respectively) is essential for the motility of cells, their ability for morphological reorganizations and cell division [17, 18].

2.2 Actin Binding Proteins

Depending on the exact definition, there are between 60 and 200 types of actin binding proteins (ABPs) which have different effects on polymerization kinetics, structural

organization of the filaments or anchoring of the network to the membrane to name just a few (see [19] for a review). For instance, actin binding proteins can sever, cap, crosslink or bundle actin filaments. By the local activation of such ABPs, cells have a powerful tool to manipulate their microstructure and their micromechanical properties and thus to adapt their local properties to the diverse tasks in a cell.

An important control parameter in the investigation of reconstituted actin networks is the molar ratio R between the ABP and actin concentration, $R = c_{\mathrm{ABP}}/c_{\mathrm{actin}}$. In some cases, it is even necessary to consider the relative concentration of actually bound ABPs, R^*, regarding the equilibrium dissociation constant K_{d}:

$$R^* = \frac{1}{2}\left(\left(1 + R + \frac{K_{\mathrm{d}}}{c_{\mathrm{actin}}}\right) - \sqrt{\left(1 + R + \frac{K_{\mathrm{d}}}{c_{\mathrm{actin}}}\right)^2 - 4R}\right) \tag{2.1}$$

Deviations of R^* from R become apparent at high R values or low actin concentrations, thus for comparing results at different actin concentration or for different values of K_{d} it is import to transfer R into R^*. A derivation of expression (2.1) can be found in appendix A.

2.2.1 Crosslinking Proteins

There is a myriad of actin binding proteins which can crosslink adjacent filaments and thus organize them into a variety of different structures ranging from a homogeneously crosslinked network of single filaments over a network of small bundles of well defined size to very thick bundles and clusters. Fig. 2.2 provides an overview of the crosslinker used in this work and the resulting actin network structure.

Fascin is a relatively small actin crosslinking protein with a molecular weight of about 55 kDa. It is mainly found in dynamic, cortical cell protrusions like spikes, filopodia or oocyte microvilli and, thus, it plays a major role in cell migration [20]. *In vitro*, fascin organizes (above a critical concentration) actin in a network of very straight, parallel bundles where no single filament can be observed (fig. 2.2(a)) [21, 22].

The addition of espin (MW $\approx$ 30 kDa) results in a similar network architecture as that caused by fascin (fig. 2.2(b)): Espin, too, forms long, straight and parallel actin bundles. *In vivo*, espin is located in parallel actin bundle structures such as brush border microvilli and hair cell stereocilia [1]. Although the structure is not yet resolved, espin is thought to be an asymmetric molecule with a Stoke's radius of about 3.4 nm [23].

Monomeric vertebrate filamin has a high molecular mass of about 260 kDa and can associate at its C-termini to large, flexible dimers (fig. 2.2(d)). Filamin is omnipresent in cells: It is found in stress bearing structures like the contractile ring and stress fibers, but is also reported to be involved in signaling processes [24]. Below a certain threshold concentration, filamin crosslinks actin filaments into an orthogonal network, above this concentration filamin builds actin bundles [25]. In contrast to fascin and espin, these bundles are curved and branched. The filaments are no longer parallel (fig. 2.2(d)). Bundle network formation results in a kinetically trapped structure where internal stresses in the bundles are present. The local network structure depends on distinct connection events during polymerization and is thus dependent on the polymerization

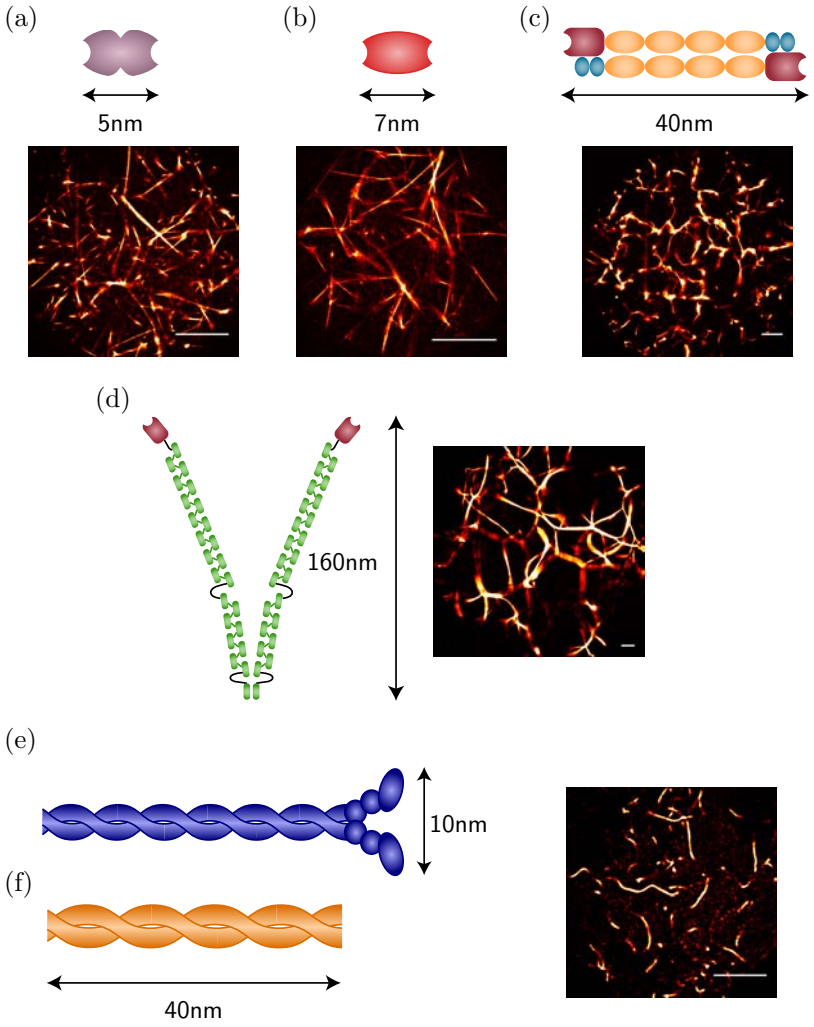

Figure 2.2: Overview of the used crosslinking proteins and the resulting network structure: (a) Fascin is a small crosslinking protein which forms long and straight actin bundles. (b) Similar to fascin, espin is a rather small crosslinking molecule and also results in straight and parallel actin bundles. (c) α-actinin consist of two antiparallel strands with a calponin homologue actin binding domain and spectrin-like spacers. It builds complicated branching bundle structures which depend sensitively on protein concentrations and preparation history. (d) Filamin is a large dimeric molecule with a binding domain similar to α-actinin and 24 ig-domains interrupted by one or two hinges. The bundles are highly curved and form branches. (e) HMM, a fragment of myosin II, contains the head domains and the coiled coil region where the two heavy chains dimerize. In the rigor state (without ATP), HMM can form interfilamental crosslinks but does not bundle. (f) Tropomyosin is a coiled coil dimer which binds end to end to actin filaments. Both, HMM and tropomyosin, result in a homogenous single-filament network – crosslinked or entangled, respectively. The networks are polymerized at $c_A = 3\,\mu M$ and in the presence of the respective crosslinker at $R = 1$. For the single filament network ((e) and (f)), only 1 % of the filaments is labelled. The scalebars denote 20 µm.

velocity [26]. As a consequence, filamin bundle networks cannot be pipetted without destroying the network morphology.

α-actinin is the most prominent actin bundling protein in stress fibers. The α-actinin molecule is composed of two identical anti-parallel peptides with a molecular mass of about 120 kDa (fig. 2.2(c)). Caused by the EF-motifs, the binding activity is calcium and temperature dependent. Similar to filamin, α-actinin builds an orthogonally crosslinked actin network at low concentrations; increasing R leads to bundling of actin. These bundle networks are – as in the case of filamin – not equilibrated and the local structure depends on the preparation history [27].

Heavy meromyosin (HMM) is the larger subfragment obtained by chymotrypsin digestion of the molecular motor myosin II [28]. HMM contains the ATPase region and the actin binding center of the motor while the light chains responsible for myosin II assembly are removed, thus inhibiting the formation of filamentous structures as found *in vivo* (fig. 2.2(e)). In the absence of ATP, HMM molecules bind to actin filaments in the rigor state and thus can act as a crosslinking molecule by forming interfilamental crosslinks beside decorating single filaments. These networks were shown to be homogeneously and isotropically crosslinked without any embedded bundle structures [29].

Tropomyosin is not an actin crosslinker in the basic sense. Tropomyosin is an alpha-helical coiled coil dimer which binds to the side of actin filaments spanning over six to seven actin subunits along the filament (fig. 2.2(f)) [30] . *In vivo*, it regulates the interaction of the filaments with myosin in dependence of the Ca^{2+} concentration. Due to its disability to form interfilamental crosslinks, actin/tropomyosin networks consist of single, entangled actin filaments.

2.2.2 Filament Length Influencing Factors

Beside the actin crosslinking proteins, there are various ABPs that influence the filament length or polymerization properties.

Latrunculin is an actin binding toxin produced by various sponges. It binds to G-actin monomers near the nucleotide binding cleft between subdomain II and IV and thus prevents conformational changes in the actin monomer necessary for polymerization [31]. This results in depolymerization of actin filaments without interactions with the actin filaments and accompanied changes in the polymerization/depolymerization rates.

Gelsolin (MW $= 82 - 86$ kDa) consists of six homologous subdomains and is one of the most potent actin filament severing proteins [32]. It severs pre-existing actin filaments and caps them, thus preventing polymerization at the plus end. Beside this F-actin interaction, there are two G-actin binding sites. Paradoxically, this leads to a nucleating activity of gelsolin under polymerizing conditions stimulating actin filament formation. The relation between gelsolin concentration and actin filament length *in vitro* is given by [33]:

$$\langle L \rangle = \frac{1}{370 R_{\mathrm{G:A}}} \mu\mathrm{m} \tag{2.2}$$

Another actin disassembling protein is cofilin (MW ≈ 15 kDa). The precise mechanism by which cofilin interacts with actin filaments is diverse and still under discussion

[34]. It has not only been reported to sequester actin monomers preventing polymerization but also to increase depolymerization kinetics by two mechanisms: increasing the depolymerization rates [35] and severing actin filaments [36–38].

2.3 Protein Purification

Actin Preparation

G-actin is obtained from rabbit skeletal muscle by a modified protocol of [39], where an additional gel filtration (Sephacryl S-300 HR) as well as an additional polymerization-depolymerization step is carried out. The actin is stored in lyophilized form at −20 °C [39]. For measurements, the actin is dissolved in water, dialysed against G-buffer (2 mM TRIS, 0.2 mM $CaCl_2$, 0.2 mM DTT, 0.005 %NaN_3, pH 8) , stored at 4 °C and used within ten days after preparation. Polymerisation was induced by adding 10-fold F-buffer (20 mM TRIS, 20 mM $MgCl_2$, 2 mM $CaCl_2$, 2 mM DTT, 5 mM ATP, 1 M KCl, pH 7.5). For fluorescence microscopy and stabilization against depolymerisation, the filaments were labelled with TRITC- and Alexa488-phalloidin, respectively. If the filament dynamics were in the center of interest, the individual monomers were labelled with the amine-reactive dye Alexa Fluor 555 carboxylic acid succinimidyl ester (Invitrogen A20009). Therefor, G-actin is dialyzed against Borat-buffer (50 mM boric acid, 0.2 mM $CaCl_2$, 0.2 mM ATP, pH 8). After polymerization induced by addition of 10-fold polymerization buffer (100 mM Imidazol, 10 mM ATP, 30 mM $MgCl_2$, 2 mM $CaCl_2$, 0.05 % NaN_3, pH 7.2) the dye (dissolved in DMSO) is added in 1-2 fold molar excess. After centrifugation the pellet is resuspended in G-buffer and dialyzed against G-buffer. The sample is clarified by centrifugation and the supernatant is stored in lyophilized form at −20 °C. A degree of labelling of about 20 % is achieved and used for all microscopy experiments. For pyrene assay experiments, the actin is labelled with pyrene by a modification of the method of [40] as described in [41].

Preparation of Actin Binding Proteins

Recombinant human fascin is expressed in E. coli BL21-codon$^+$ bacteria by a modification of the method of as [42] described before [21]. Human espin 3A is expressed in bacteria and purified as described in [43]. Muscle filamin is isolated from chicken gizzard and further purified as reported in [44]. α-actinin is isolated from turkey gizzard smooth muscle following [45], dialyzed against G-buffer and stored at 4 °C for several weeks. HMM is prepared from myosin II by chymotrypsin digestion and tested using motility assays as in [46]. Tropomyosin troponin is prepared from the residue of rabbit muscle acetone powder left after the actin extraction [39] and separated into tropomyosin and troponin by hydroxyl apatite column chromatography [47].

Latrunculin B (Sigma-Aldrich) dissolved in DMSO (5 mM) is stored at −20 °C. Prior to use, it is diluted to 500 µM in G-buffer without ATP. Gelsolin is obtained from bovine plasma serum as reported in [48]. *Dictyostelium discoideum* cofilin is expressed as a GST fusion protein in E.Coli DH5alpha cells. The GST tag is removed by cleavage

with the factor Xa and cofilin is stored in 10 mM Tris, 0.2 mM $CaCl_2$, 0.2 mM DTT, pH 8.

Chapter 3

Diffraction on Arrays of Helical Molecules

X-Ray diffraction is the most powerful technique currently available for studying the structure of large molecules or assemblies of molecules. If it is possible to crystallize the protein, X-ray structure analysis yields the complete secondary and tertiary structure at a level of a few Å. Even if no crystal is available, Small Angle X-ray Scattering (SAXS) still provides a wealth of structural information. Though it is insufficient to determine the structure uniquely, this information can provide in many cases decisive tests of structural models. Concentrated gels of helical molecules, for example, can be analyzed in so-called fiber diffraction experiments to obtain information about the mutual arrangement of monomers in the bundle and the alignment of the fibers.

In this chapter, a short theoretical description of the diffraction on solutions of helical molecules is given. The first section provides a brief introduction to the basics of a SAXS experiment and a definition of the variables used in the theoretical description. Section 3.2 describes the scattering by an isolated helical molecule, starting from a continuous helical line extending to a "real" helix, including discontinuity along the helix and the structure of an individual monomer. Section 3.3 presents how different types of assembly of the filaments and their diffraction pattern are modeled. A discussion how continuous twisting and stretching of the helix will change the diffraction pattern is given in section 3.4.

The present chapter is limited to the theoretical description necessary for the evaluation of the scattering pattern by F-actin bundles in section 4. An easily understandable introduction is provided in [49], a quite detailed derivation can be found in [50].

3.1 Basics of SAXS Diffraction

In order to understand X-ray diffraction experiments one must understand how X-rays interact with the electrons in the atomic shells in a sample. There are a lot of different approaches to the theory of diffraction in nearly all solid state physics textbooks. This brief introduction omits several second-order complications to focus on the essential features of the method: Atoms are treated as motionless, X-rays are treated as monochromatic, even though a distribution of wavelengths is always used in practice, the polymers (or crystals) are treated as perfectly ordered (at least in the beginning), even though they may be ordered only in local domains, and so on.

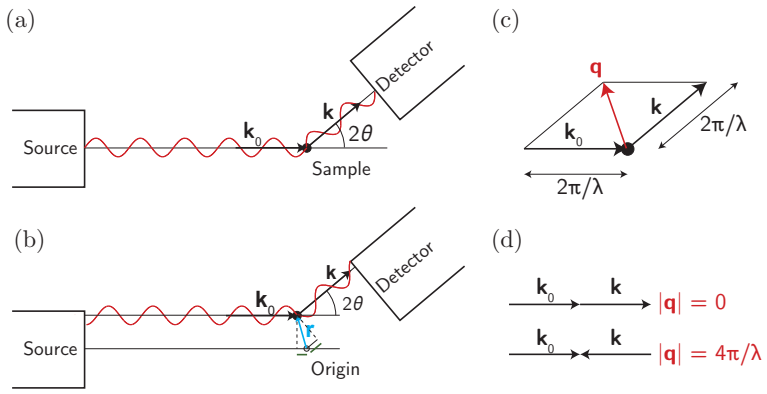

Figure 3.1: Basic geometry of a X-ray scattering experiment: (a) X-ray scattering on a single electron at the origin and (b) an electron located at position $\mathbf{r}$ relative to the origin with the same angle of deflection 2θ. The path length difference is indicated by the green lines. (c) Geometrical representation of the scattering vector $\mathbf{q}$. (d) Arrangements of $\mathbf{k}_0$ and $\mathbf{k}$ which lead to minimal and maximal values of |q|.

Like all other photons, X-rays can be treated by electromagnetic waves described

$$A = A_0 \mathrm{e}^{i(\mathbf{kr}-\omega t)} \tag{3.1}$$

where $\mathbf{k}$ is the vector of propagation direction with length $|\mathbf{k}| = \frac{2\pi}{\lambda}$. The geometry of a scattering experiment can be described by placing the sample (or rather the scattering electrons) at the origin (Fig. 3.1(a)). In a classical picture, the incoming plane wave accelerates the charge, which emits its own radiation at the same wavelength (elastic scattering, $|\mathbf{k}_0|=|\mathbf{k}|$) in the form of a spherical wave. If the distance to the detector is much larger than the wavelength, the spherical wave arrives as a plane wave at the detector position. The absolute radiation intensity can be computed by proper consideration of the quantum mechanics of photons interacting with matter.

However, X-ray scattering relies on the interference patterns that are created by a regular array of scattering centers. The relative phase difference in the spherical waves arriving at the detector can be obtained by moving the electron by a vector $\mathbf{r}$ away from the origin (Fig. 3.1(b)). For large sample-detector distances, the scattering angle, 2θ, can be regarded as identical as for the electron at the origin. The difference arises in the path length which can simply be calculated to be $\mathbf{kr} - \mathbf{k}_0\mathbf{r} = (\mathbf{k} - \mathbf{k}_0)\mathbf{r}$. It is convenient to define the momentum transfer from the X-ray radiation to the electron, the so-called scattering vector, $\mathbf{q} = \mathbf{k} - \mathbf{k}_0$, which plays a great role in diffraction theory (see Fig. 3.1(c) and (d)). The length of of the scattering vector is

$$q = 4\pi|\sin\theta|/\lambda \tag{3.2}$$

and varies from 0 to $4\pi/\lambda$. Thus, the vector $\mathbf{q}$ is described in a finite coordinate system in which each axis has the dimensions of a reciprocal distance. This coordinate system is called the reciprocal space.

As one is interested in the effect of relative electron position, the structure factor, $F(\mathbf{q})$, is defined by the phase shift obtained relative to the scattering on an electron

at the origin. Moving the electron to a position $\mathbf{r}$ causes a phase shift of $\mathbf{qr}$; thus, the structure factor is given by $F(\mathbf{q}) = \mathrm{e}^{i\mathbf{qr}}$.

A sample with many heterogenous scattering sites has a structure factor which is simply the sum over many individual structure factors, each weighted with an atomic scattering factor f_j, which is a measure of the scattering amplitude of a wave by the isolated atom:

$$F(\mathbf{q}) = \sum_j f_j \mathrm{e}^{i\mathbf{q}\mathbf{r}_j} \tag{3.3}$$

In the limit of a continuous electron distribution $\rho(\mathbf{r})$, this sum becomes the integral

$$F(\mathbf{q}) = \int \mathrm{d}\mathbf{r}\rho(\mathbf{r})\mathrm{e}^{i\mathbf{q}r} \tag{3.4}$$

which is exactly the Fourier transform of the electron density $\rho(\mathbf{r})$. Thus, the observed diffraction pattern of a sample is the Fourier transform of the electron density of the sample.

The Structure Factor of an One-Dimensional Array

Before calculation of the structure factor for a helical molecule, let us first consider the more basic example of a row of $2N + 1$ identical atoms, in which the central atom is located at the origin and the atoms are separated by the distance c. Thus, the position of the n^{th} atom in the array is $n\mathbf{c}$. The structure factor of this array is according to (3.3):

$$F_{tot}(\mathbf{q}) = f(\mathbf{q}) \sum_{n=-N}^{N} \mathrm{e}^{in\mathbf{q}\cdot\mathbf{c}} \tag{3.5}$$

where $f(\mathbf{q})$ is the form factor of the atoms. This geometric series can be rewritten into

$$\begin{aligned} F_{tot}(\mathbf{q}) &= f(\mathbf{q}) \frac{\mathrm{e}^{-iN\mathbf{q}\cdot\mathbf{c}}(1 - \mathrm{e}^{i(2N+1)\mathbf{q}\cdot\mathbf{c}})}{1 - \mathrm{e}^{i\mathbf{q}\cdot\mathbf{c}}} && (3.6) \\ &= f(\mathbf{q}) \frac{\sin\left((N + \frac{1}{2})\,\mathbf{q}\cdot\mathbf{c}\right)}{\sin\left(\frac{1}{2}\,\mathbf{q}\cdot\mathbf{c}\right)} && (3.7) \end{aligned}$$

As N becomes large, the intensity tends to zero everywhere except where $\mathbf{q}\cdot\mathbf{c}$ is integral which is called the *Laue condition*.

Assuming now – without loss of generality – $\mathbf{c} \parallel \hat{\mathbf{z}}$, it follows in the limit of large numbers of atoms N (see [50]) and neglecting constant prefactors

$$\lim_{N\to\infty} \frac{\sin\left((N + \frac{1}{2})\,cq_z\right)}{\sin\left(\frac{1}{2}\,cq_z\right)} = \sum_{n=-\infty}^{\infty} \delta\left(q_z - \frac{2\pi n}{c}\right) \tag{3.8}$$

The scattering amplitude of an one-dimensional array with spacing $\mathbf{c}$ is thus finite only in planes perpendicular to $\mathbf{c}$ with spacing $\frac{2\pi}{c}$ in the reciprocal space. This feature of the so-called layer lines persists in the pattern by any assembly of chain molecules in which the periodicity is preserved.

3.2 Diffraction on a Helical Molecule

Helical molecules are ubiquitous in biological systems: DNA, α-helical proteins, collagen or F-actin, to mention just a few of the most prominent examples. The diffraction pattern of a solution of such polymers reflects several contributions: firstly, the scattering from each individual molecule of the polymer, secondly the intermolecular scattering governed by their helical arrangement, and finally the influence of the packing of polymers: common types of assemblies include crystalline packing, alignment along the axial direction or an amorphous solution. To obtain structural information of self assemblies containing helical molecules, it is first of all necessary to understand the expected diffraction pattern caused by the helical nature of the molecules themselves. This section deals with the scattering on an ideal isolated helical molecule which has a certain symmetry and consists of a very large number of residues, which may be taken as infinite. As one is interested rather in relative intensities than the absolute values, constant prefactors are often neglected.

3.2.1 The Fourier Transformation in Cylindrical Coordinates

Due to their circular symmetry it is most convenient to describe the structure factor of helical molecules using the cylindrical coordinate system instead of the cartesian coordinates. The Fourier transform is then given by:

$$F(\mathbf{q}) = \int_{-\infty}^{\infty} \mathrm{d}z \int_0^{2\pi} \mathrm{d}\psi \int_0^{\infty} r\mathrm{d}r\rho(\mathbf{r})\mathrm{e}^{i(rq_r\cos(\psi-\Psi)+zq_z)} \tag{3.9}$$

The following relations between cartesian and cylindrical coordinates in real and reciprocal space are used:

$$x = r\cos\psi \quad y = r\sin\psi \quad z = z \tag{3.10}$$

$$q_x = q_r\cos\Psi \quad q_y = q_r\sin\Psi \quad q_z = q_z \tag{3.11}$$

Assuming a periodicity in $\hat{\mathbf{z}}$ with length c, the electron density distribution $\rho(\mathbf{r})$ can be described as convolution of a one-dimensional array along $\hat{\mathbf{z}}$ and the density distribution of the unit cell:

$$\rho(\mathbf{r}) = \rho_{uc}(\mathbf{r}) * \delta(x)\delta(y)\sum_n \delta(z-nc) \tag{3.12}$$

The scattering amplitude can be calculated using equation (3.8) and the convolution theorem, which states that the Fourier transform of a convolution is the pointwise product of Fourier transforms

$$\begin{aligned} F(\mathbf{q}) &= \mathrm{FT}[\rho_{uc}(\mathbf{r})]\cdot\mathrm{FT}[\delta(x)\delta(y)\sum_n\delta(z-nc)] \\ &= \mathrm{FT}[\rho_{uc}(\mathbf{r})]\cdot\sum_{n=-\infty}^{\infty}\delta\left(q_z-\frac{2\pi n}{c}\right) \end{aligned} \tag{3.13}$$

Combining equation (3.9) and equation (3.13) reveals

$$F(q_r, \psi, \frac{2\pi n}{c}) = \int_0^c \mathrm{d}z \int_0^{2\pi} \mathrm{d}\Psi \int_0^\infty r\mathrm{d}r\rho_{uc}(\mathrm{r})\mathrm{e}^{i(rq_r\cos(\psi-\Psi)+z\frac{2\pi n}{c})} \tag{3.14}$$

3.2.2 The Structure Factor of a Continuous Helical Line

Let us consider first the Fourier transform for a continuous helix of radius r_0 and pitch c. The z coordinate in the helical unit cell is proportional to ψ: $z = \psi c/2\pi$. Assuming the electron density to be unity along the helix, the distribution is given by the product of two δ-functions:

$$\rho_{ch} = \delta(r - r_0)\delta\left(z - \frac{\psi c}{2\pi}\right) \tag{3.15}$$

A continuous helix is periodic along the helical axis, the structure repeats exactly after the pitch c. Thus, its structure factor can be calculated using equation (3.14)

$$\begin{aligned} F_{ch}(q_r, \Psi, \frac{2\pi n}{c}) &= \int_0^c \mathrm{d}z \int_0^{2\pi} \mathrm{d}\psi \int_0^\infty r\mathrm{d}r\delta(r - r_0)\delta\left(z - \frac{\psi c}{2\pi}\right)\mathrm{e}^{i(rq_r\cos(\psi-\Psi)+z\frac{2\pi n}{c})} \\ &= \int_0^{2\pi} \mathrm{d}\psi r_0 \mathrm{e}^{i(r_0 q_r\cos(\psi-\Psi)+n\psi)} \end{aligned} \tag{3.16}$$

This integral resembles the Bessel function of the first kind. The Bessel function of n^{th} order is defined as

$$J_n(x) = (1/2\pi i^n)\int_0^{2\pi} \mathrm{e}^{ix\cos y + iny}\mathrm{d}y \tag{3.17}$$

Substitution by $x = r_0 q_r$ and $y = \psi - \Psi$ in equation (3.16) leads to (using the relation $i^n = \mathrm{e}^{ni\pi/2}$ and neglecting constant prefactors)

$$F_{ch}(q_r, \Psi, \frac{2\pi n}{c}) = r_0\mathrm{e}^{in(\Psi+\pi/2)}J_n(r_0 q_r) \tag{3.18}$$

The structure factor of a continuous helical line with radius r_0 and pitch c is therefore a set of Bessel functions, where the function of order n is positioned on a layer line at $q_z = \frac{2\pi n}{c}$ (Fig. 3.2(a)). The first maximum of the Bessel function is shifted to higher values of q_r with increasing order. This results in the characteristic X-shaped scattering pattern for a helical line as it is known for DNA (Fig. 3.2(b)).

3.2.3 The Structure Factor of a Discontinuous Helix

A discontinuous helical polymer consists of one type of molecule repeated (in first approximation) infinitely by a screw axis of symmetry. Thus, the structure factor will be given by

$$F_{tot}(\mathbf{q}) = f(\mathbf{q})F_{dh}(\mathbf{q}) \tag{3.19}$$

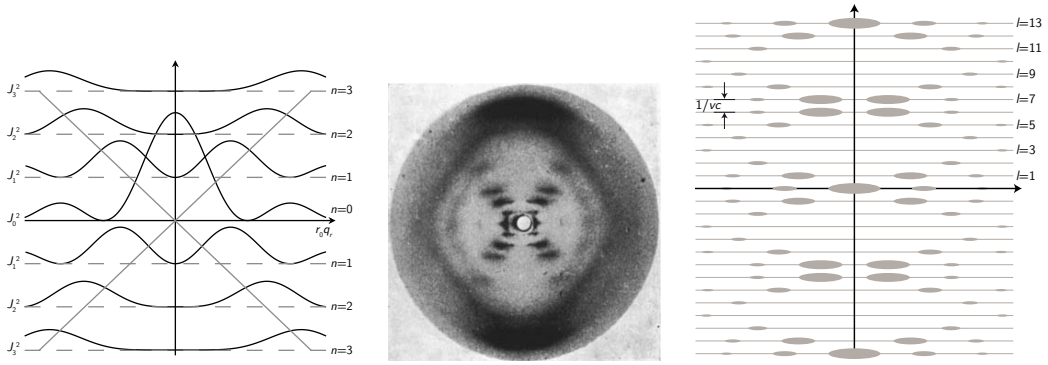

(a) (b) (c)

Figure 3.2: (a) Bessel functions which contribute to the scattering of helices. Shown are $J_n^2(r_0 q_r)$ for $n = 0$ to $n = 3$. Note the continuous shift and decrease in intensity of the first maximum with increasing order n. (b) This progressive shift results in the typical X-shaped diffraction pattern of DNA, as can be seen in the famous Photo 51 of Rosalind Franklin [51]. (c) Distribution of the main peaks in the Bessel functions over the layer lines for an -13/6 helix as it is expected for F-actin.

where $f(\mathbf{q})$ is the monomeric form factor and $F_{dh}(\mathbf{q})$ is the sampling function of the helical lattice, i.e. a system of points arranged along a helical line with distance h along the z axis . This can be described mathematically by forming the product (intersection) of a helical line with a set of parallel planes (cf. Fig. 3.3)

$$\rho_{dh}(r, \psi, z) = \rho_{ch}(r, \psi, z)\rho_{pp}(r, \psi, z) \tag{3.20}$$

According to the convolution theorem, the structure factor of a discontinuous helix can be calculated by convolution of the transforms of the two functions in reciprocal space. The transform for a continuous helix is already derived (equation (3.18)). Furthermore, we have deduced a system of planes as the Fourier transform of an one-dimensional array of points (cf. equation (3.8)). Following the reversibility of the Fourier transformation, the structure factor of a set of parallel planes perpendicular to $\hat{\mathbf{z}}$ with spacing h is a set of points in reciprocal space with spacing $2\pi/h$.

$$F_{pp}(q_r, \Psi, q_z) = \sum_{m=-\infty}^{\infty} \delta(q_z - \frac{2\pi m}{h})\delta(q_r - q_{r0})\frac{\delta(\Psi)}{q_{r0}}, m \in \mathbb{Z} \tag{3.21}$$

Using this result and equation (3.18), the structure factor of a discontinuous helix

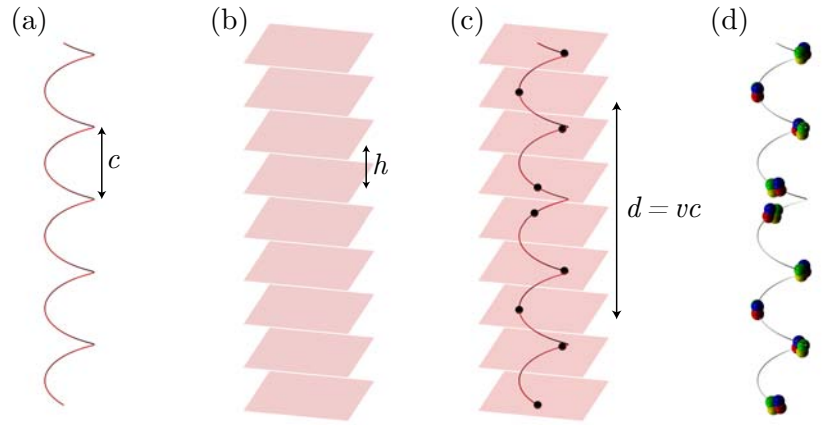

Figure 3.3: The discontinuous helix can be generated mathematically by forming the product (intersection) of (a) a continuous helical line with pitch c with (b) a set of planes with distance h, corresponding to the distance of residues along the helical axis. (c) The points of intersection represent the position of single residue units. (d) Considering the complex structure of each residue, the structure of the helical polymer can be described as convolution of the point lattice as derived in (c) with the structure of one residue.

can be calculated

$$\begin{aligned} F_{dh}(q_r, \Psi, q_z) &= F_{ch} * F_{pp} = \\ &= \sum_{n=-\infty}^{\infty} \sum_{m=-\infty}^{\infty} \int\int\int \mathrm{d}q_r' \mathrm{d}q_z' \mathrm{d}\Psi' \mathrm{e}^{in(\Psi'+\pi/2)} J_n(r_0 q_r') \delta(q_z' - \frac{2\pi n}{c}) \\ &\quad \delta(q_z - q_z' - \frac{2\pi m}{h}) \delta(q_r - q_r' - q_{r0}) \frac{\delta(\Psi - \Psi')}{q_{r0}} \\ &= \sum_{n=-\infty}^{\infty} \sum_{m=-\infty}^{\infty} \mathrm{e}^{in(\Psi+\pi/2)} J_n(r_0 q_r) \delta\left(q_z - 2\pi\left(\frac{n}{c} + \frac{m}{h}\right)\right) \end{aligned}$$

$$F_{dh}\left(q_r, \Psi, 2\pi\left(\frac{n}{c} + \frac{m}{h}\right)\right) = \sum_{n,m=-\infty}^{\infty} \mathrm{e}^{in(\Psi+\pi/2)} J_n(r_0 q_r) \tag{3.22}$$

The sum is done over all values of $m, n \in \mathbb{Z}$ which satisfy the constraint:

$$q_z = 2\pi\left(\frac{n}{c} + \frac{m}{h}\right) \tag{3.23}$$

Thus, several Bessel functions contribute for each layer line, instead of only one for a continuous helix. Due to the decrease in amplitude, it is often sufficient to take into account only the Bessel function terms up to a certain order depending on the radius of the molecule and the distance to the meridian [52]. In the case of actin, this is in first approximation often the lowest-order term.

Many of the helical proteins do not have an integral number of residues per turn. However, most of them can be described as a helix with k residues in v turns. The

overall structure repeats in this case after the length $d = vc$ (cf. Fig. 3.3(c)), the spacing between adjacent residues along the helical axis is given by $h = vc/k$. Substituting these assumptions in equation (3.23) directly reveals for the layer lines a spacing of $2\pi/vc$:

$$\begin{aligned} q_z &= 2\pi\left(\frac{n}{c} + \frac{km}{vc}\right) = 2\pi\frac{vn + km}{vc} \\ &= \frac{2\pi l}{vc}, \quad \text{with } l = km + vn \end{aligned} \tag{3.24}$$

As k, v, m and $n \in \mathbb{Z}$, l also has to be an integer.

F-actin can be described in its native state by a helical symmetry of $-13/6$ (see 2.1). The selection rule results in

$$l = 13m - 6n \tag{3.25}$$

In this case of a non-integral number of residues per turn, the diffraction pattern is more finely spaced, the layer lines appearing every $1/vc$. The diffraction pattern repeats every k^{th} layer line and the distribution of Bessel functions is no longer characterized by the X-shape, but by a complex pattern described by the selection rule given in equation (3.24). An example is shown in Fig. 3.2(c).

3.2.4 The Structure Factor of a Real Helical Molecule

The residues of a helical polymer are not sufficiently well described by a δ-function or just a single sphere. In fact, they consist of many atoms, which each form their own helical polymers with the corresponding atoms in the other residues along the polymer. Thus, the whole molecule can be described as a sum of many helices, which have the same pitch c, but different radii r_j and which are shifted by the relative position (r_j, ψ_j, z_j) of each atom in the monomer. Since the structure factor is the Fourier transform of the electron density distribution and the Fourier transform of a sum is just the sum of the Fourier transforms of each summand, equation (3.22) is generalized to:

$$F_l(q_r, \Psi) = \sum_n \sum_j f_j J_n(r_j q_r) \mathrm{e}^{i(n(\Psi - \psi_j + \pi/2) + \frac{2\pi l}{c} z_j)} \tag{3.26}$$

where r_j, ψ_j and z_j are the coordinates and f_j the form factor of the j^{th} atom.

As described in section 2.1, the actin monomer is described sufficiently by the 4-bead model. Hence, it is not necessary to sum over all atoms in the monomer but only over the four beads corresponding to the four domains of the monomer. The atomic form factor f_j is replaced by the form factor of a solid sphere of radius a:

$$f_{sphere,j}(q) = \frac{4}{3}\pi a_j^3 \frac{3\sin(a_j q) - a_j q\cos(a_j q)}{(a_j q)^3} \tag{3.27}$$

3.3 Scattering on Assemblies of Filaments

Since an assembly of filaments will not generally form regular crystals, the often powerful methods of conventional crystallographic analysis is in this case not applicable.

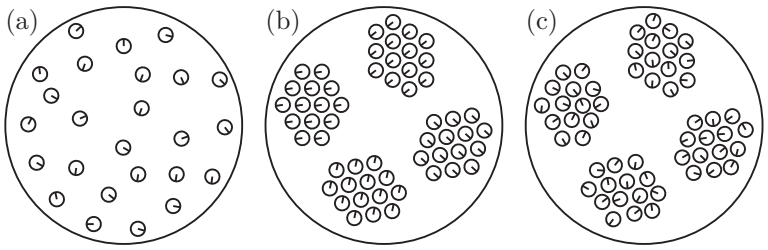

Figure 3.4: Crosssections of a (a) non-crsytalline, (b) polycrystalline and (c) polycrystalline specimen with significant disorder. The small circles represent the fiber, the angular orientation is indicated by the line.

However, in some samples, the filaments are oriented approximately in parallel along their long axis, but randomly rotated about and shifted along this axis (Fig. 3.4(a), e.g. the B-form of DNA). There is only a slight correlation between the positions of neighboring filaments so that each filament scatters independently. Due to the absent azimuthal correlation between the fibers, the cylindrically averaged diffraction pattern of a single fiber is observed. As shown above, the diffraction patterns of such *non-crystalline* specimens contain diffracted intensity distributed continuously along the layer lines.

In some cases, the fibers organize laterally into small regions of three-dimensional crystallinity, where the rotational orientation of the crystallites about their long axis is random (Fig. 3.4(b), e.g. the A-form of DNA). The resulting diffraction pattern of such *polycrystalline* specimens is equivalent to the pattern of one crystal cylindrically averaged, and the scattered intensity is restricted to discrete points (Bragg points) on the layer lines in reciprocal space.

Non-crystalline and polycrystalline ordering are the limiting cases usually observed in fiber diffraction. A diffraction pattern which contains both, Bragg peaks and continuous intensity, indicates a more complex assembly of the molecules. Possible configurations are a two-phase system where quite perfect crystalline domains are embedded in amorphous regions, or a substitutional disorder in the packing of the polymers in the polycrystalline ordering (Fig. 3.4(c)) [53].

The diffraction pattern of such an assembly of helices includes the scattering effects for the isolated molecule together with effects caused by deviation from the ideal molecular structure due to variations in orientation, in their packing, in the size and their mutual disposition. These effects complicate the derivation of the real structure from the observed diffraction pattern for a solution or array of helices. The most fruitful approach uses the comparison of calculated intensity patterns of trial models with the measured data. Clearly then, an accurate calculation of the diffraction pattern from the model is essential, including all effects of assembly and disorder.

3.3.1 Diffraction by Non-Crystalline Specimens

In a non-crystalline specimen, the molecules are approximately aligned in parallel, but randomly oriented in the sample, meaning that all orientations of he real space

angle ψ appear at random. Given the typical fiber diameter of some nanometers and the typical beam size of several hundred micrometers, the recorded intensity is the cylindrical average of the scattering pattern of a single molecule. This is computed by averaging the scattering intensity for an isolated fiber over the corresponding angle Ψ in reciprocal space.

Until now we have dealt with the structure factors, whereas one can measure only the scattering intensity. For an isolated helix this is – according to equation (3.22) – given by

$$\begin{aligned} I_l(q_r,\Psi) &= F_l F_l^* \\ &= \sum_{n=-\infty}^{\infty} \mathrm{e}^{in(\Psi+\pi/2)} J_n(r_0 q_r) \sum_{n'=-\infty}^{\infty} \mathrm{e}^{-in'(\Psi+\pi/2)} J_{n'}(r_0 q_r) \\ &= \sum_n \sum_{n'} J_n(r_0 q_r) J_{n'}(r_0 q_r) \mathrm{e}^{i(n-n')\pi/2} \mathrm{e}^{i(n-n')\Psi} \end{aligned} \tag{3.28}$$

where each sum is carried out over the values of n and n' allowed by the selection rule (3.24). By azimuthally averaging this equation over Ψ, one derives

$$\langle I_l(q_r)\rangle = \sum_n \sum_{n'} J_n(r_0 q_r) J_{n'}(r_0 q_r) \mathrm{e}^{i(n-n')\pi/2} \int_0^{2\pi} \mathrm{d}\Psi \mathrm{e}^{i(n-n')\Psi} \tag{3.29}$$

The integral over Ψ is zero unless $n = n'$. Thus, it follows

$$\langle I_l(q_r)\rangle = \sum_n J_n^2(r_0 q_r) \tag{3.30}$$

This is what was actually plotted in Fig. 3.2 and is shown in Fig. 3.5(a) for the polynucleotide duplex poly(dA)·poly(rU), which has 11/1 helical symmetry and a trigonal unit cell packing.

Equation (3.30) can be generalized for helices with several atoms per unit cell:

$$\langle I_l(q_r)\rangle = \sum_n \left| \sum_j f_j J_n(r_j q_r) \mathrm{e}^{i(-n\psi_j + \frac{2\pi l}{c} z_j)} \right|^2 \tag{3.31}$$

3.3.2 Diffraction by Bundles

A major part of this work focuses on the characterization of F-actin bundles. This section describes how bundling effects the diffraction pattern of helical filaments. First an ideal infinitely large array of molecules is regarded before the effects of finite size and inaccuracy are included.

Diffraction by a Perfect Crystal

In the following, we consider helical filaments which are arranged in an ideal two-dimensional array without any rotation or inclination. The electron density of this

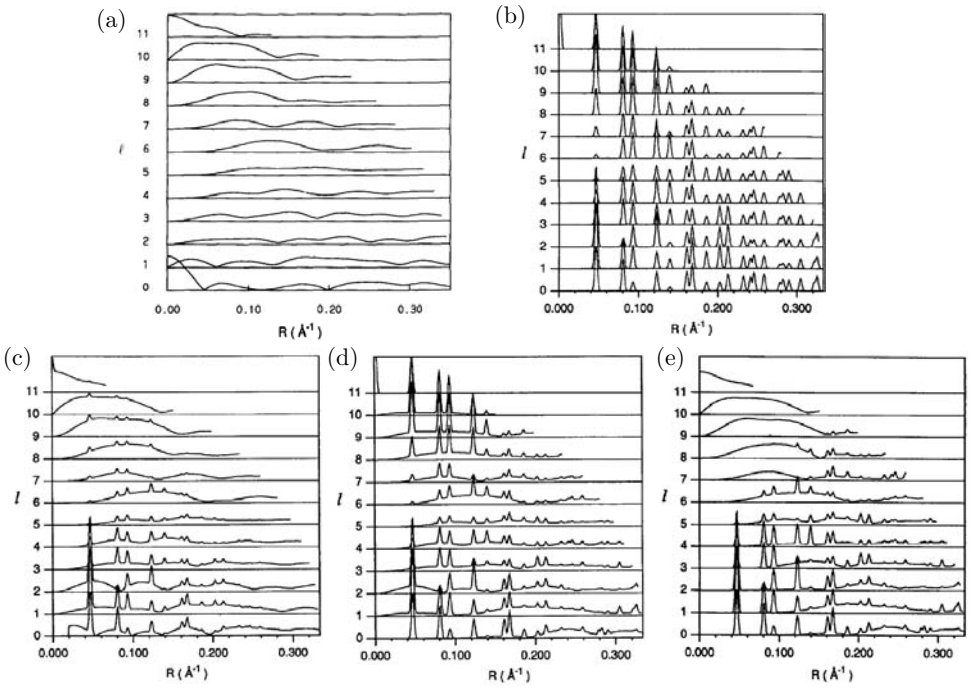

Figure 3.5: Calculated layer line amplitudes of the polynucleotide duplex poly(dA)·poly(rU), which has 11/1 helical symmetry and a trigonal unit cell, in a (a) non-crystalline, (b) polycrystalline and (c)-(e) polycrystalline specimen with distinct disorder (from [54] and [53]). While the scattering of a perfect non-crystalline sample shows the continuous layer line pattern of the single fiber, bundling results in a splitting up in different sharp Bragg peaks. Disorder leads to a mixed diffraction pattern with Bragg peaks superimposed on a continuous pattern: Lattice distortion suppresses Bragg reflections at high q_r and q_z values (c), rotational disorder decreases Bragg reflections in higher-order Bessel functions (d), and random screw disorder suppresses the peaks in higher order layer lines (e).

arrangement can be calculated by a convolution of the density of an individual filament ρ_{fil} with the one of the two-dimensional array ρ_{lattice}, which we call the disposition function:

$$\rho = \rho_{\text{fil}} * \rho_{\text{lattice}} \tag{3.32}$$

According to the convolution theorem, the structure factor is simply the product of $F_{\text{fil}}(\mathbf{q})$ and $B(\mathbf{q}) = \mathcal{FT}[\rho_{\text{lattice}}]$

$$F(\mathbf{q}) = F_{\text{fil}}(\mathbf{q})B(\mathbf{q}) \tag{3.33}$$

The measured intensity is the absolute square of the structure factor:

$$\begin{aligned} I(\mathbf{q}) &= [F_{\text{fil}}(\mathbf{q})B(\mathbf{q})][F_{\text{fil}}(\mathbf{q})B(\mathbf{q})]^* = F_{\text{fil}}(\mathbf{q})B(\mathbf{q})F_{\text{fil}}(\mathbf{q})^*B(\mathbf{q})^* \\ &= [F_{\text{fil}}(\mathbf{q})F_{\text{fil}}(\mathbf{q}^*)][B(\mathbf{q})B(\mathbf{q})^*] = |F_{\text{fil}}(\mathbf{q})|^2|B(\mathbf{q})|^2 \end{aligned} \tag{3.34}$$

The simple rearrangement of the factors shows that the scattering intensity of a set of filaments can be found by multiplication of the intensity for an isolated molecule and the scattering intensity for a set of points specified by the disposition function. Remember that this is deduced only on the assumption of parallel transfer of molecules with no lateral or rotational change.

The structure factor of the filaments were calculated in the previous section; the three-dimensional Fourier transform of a two-dimensional lattice is an array of infinite lines arranged on the corresponding two-dimensional lattice. These transforms are in general well known [55].

The most usual packing for helices is hexagonal, more rare is the quadratic array. The periodicity in these packings will produce diffraction spots lined up on the equator ($l = 0$). The characteristic distances between the spots are determined by the distances appearing in the corresponding reciprocal lattice (see Fig. 3.6). The reciprocal lattice of a hexagonal array (with lattice constant d) is again hexagonal with the lattice constant $\frac{4\pi}{\sqrt{3}d}$. In the case of a quadratic array, the reciprocal lattice is quadratic with the lattice constant $\frac{2\pi}{d}$. As indicated in fig. 3.6, the sequence of relative distances between the peaks will be $1, \sqrt{3}, 2, \sqrt{7}$,... and $1, \sqrt{2}, 2, \sqrt{5}$,... for a hexagonal and a quadratic array, respectively.

However, the bundling does not only effect the scattering on the equator. Due to the convolution, also the layer line pattern is visible only as spots aligned along q_z in columns located at q_r values which correspond to the hexagonal lattice vectors. This results in a splitting up in several sharp peaks (see Fig. 3.5(b)).

Diffraction by a Polycrystalline Sample

In a polycrystalline specimen, several smaller crystallites are randomly oriented but aligned parallel to the long axis of the fibers (Fig. 3.4). The shape of these objects is not infinitely large but can be described by the shape functions $\Phi(\mathbf{r})$ which is equal to unity within the object and zero outside. Analogous to equation (3.32), the electron density of such a crystallite is:

$$\rho(\mathbf{r}) = \rho_{\text{fil}}(\mathbf{r}) * [\rho_{\text{lattice}}(\mathbf{r})\Phi(\mathbf{r})] \tag{3.35}$$

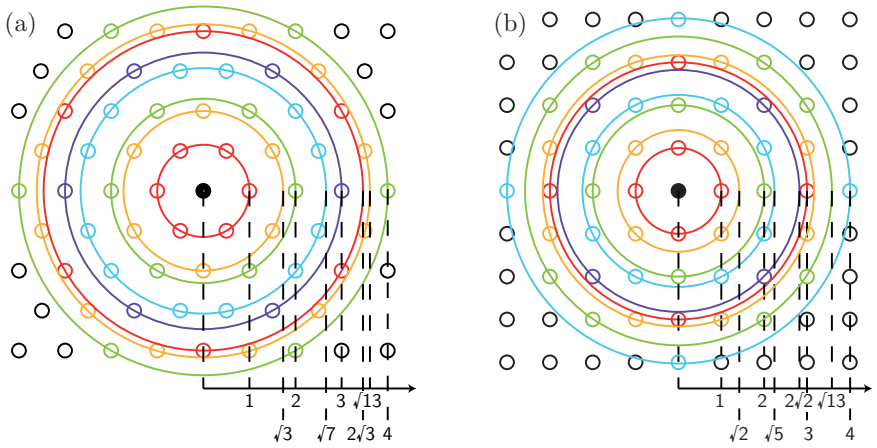

Figure 3.6: Comparison of the expected pattern for (a) a hexagonal and (b) a quadratic array. The sequence of relative distances between peaks is characteristic for each two-dimensional lattice and is determined by the distances appearing in the corresponding reciprocal lattice.

Similar to non-crystalline specimens, averages over many crystallites with random orientation will be regarded in a scattering experiment. As a result, the recorded intensity is the cylindrical average of the intensity pattern of a single crystallite. Thus, the Bragg peaks become rings in the $q_x q_y$-plane centered on the q_z axis. [50]

Effects of Finite Size and Coherence Length

The theory discussed so far assumed a perfect polycrystalline sample in which the constituent crystallites are composed of structurally regular molecules of infinite length. Furthermore, the shape of the crystallites was not included in the calculation so far.

The most important of the shape effects is the finite size of the object. It is possible to estimate the domain size d of a bundle by fitting the peak width Δq (FWHM) of the diffraction peak using the Scherrer-equation [56]:

$$d = \frac{0.9\lambda}{\cos\theta_0 \Delta(2\theta)} \tag{3.36}$$

Using the relation $\Delta(2\theta) = \frac{2\lambda}{4\pi}\Delta q$ (following from (3.2) small-angle-approximation), this can be rewritten to

$$\begin{aligned} d &= \frac{0.9 \cdot 2\pi}{\cos\left(\frac{\lambda q_0}{4\pi}\right)\Delta q} \\ &\approx 1.8\frac{\pi}{\Delta q} \end{aligned} \tag{3.37}$$

where $\lambda = 0.995\,\text{Å}$ and $q_0 = 0.057\,\text{Å}^{-1}$ (see experimental section) and thus $\cos\left(\frac{\lambda q_0}{4\pi}\right) = 1$ is used.

In very rigid bundles, where the inter-filamental correlation holds over large scales, this domain size is a good approximation of the bundle size. In quite loose bundles, it is

a measure of disorder in the lateral rod-rod positions. Note, that the width in equation (3.37) has to be corrected for the limited resolution of the system. The measured width has two contributions: First the contribution of finite bundle or domain size and secondly, the resolution limitation, which are connected by convolution. For a discussion of the resolution limit see 4.1.

The same effect of finite correlation length influences the pattern along q_z. A real helical molecule is not a perfect crystal, and so the measured intensity will not consist of δ-shaped layer lines. This results in a finite width of these layer lines along q_z. It is common, to model them with Gaussian profiles $\exp\left(-\pi p^2\left(q_z - \frac{2\pi l}{vc}\right)^2\right)$ where p is the coherence length of the helix along q_z [57].

Disorder in the Bundle

The effect of disorder on the diffraction pattern is quite complicated and depends on the kind and degree of disorder. It is convenient to classify the different types into lattice disorders, which describes deviations in the fiber positions from the ideal lattice, and substitutional disorders, which consists of shifts along the helical axis, orientational, directional or screw disorder. All these types can appear as small random disorders about a mean value, completely random displacements, switching between distinct states or continuous shifts.

There is a huge amount of literature on the various models and their effect on the diffracted intensity. A general expression of the intensity can be found in [50], in [54] a detailed analysis for different types of disorder in finite crystallites cylindrically averaged is presented. The special case of a two-dimensional raft is discussed in [58]. Here, a short overview of the most important effects is given.

As stated above, the diffraction pattern of a disordered polycrystalline sample can be written as the sum of Bragg and continuous components,

$$I = I^B + I^C \tag{3.38}$$

with

$$I^B = |\langle F\rangle|^2 \mathscr{Z} \tag{3.39}$$

$$I^C = N\langle|F|^2\rangle - |\langle F\rangle|^2 \tag{3.40}$$

where N is the number of fibers in the crystal. The interference function $\mathscr{Z}$ is the square of the Fourier transform of the infinite crystal lattice times the shape function, $\Phi(\mathbf{r})$ (cf. equation (3.35)), and describes the position and amplitude of the Bragg peaks. The peak amplitudes are proportional to N^2, so that the Bragg component is approximately N times the intensity of the continuous contribution. Thus, the continuous component contributes significantly only for small crystallite sizes.

The particular diffraction pattern will depend on the type of disorder. Fig. 3.5 exemplifies the layer line amplitudes for three different models of disorder. Lattice distortions, which include a small normally distributed lateral and axial disorder, suppress the Bragg intensities with increasing q_r and q_z, accompanied by an increase of

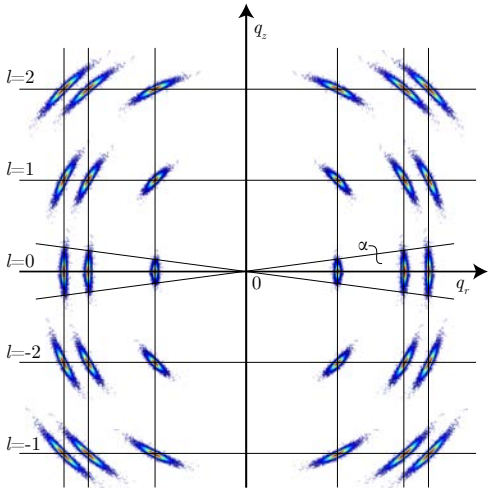

Figure 3.7: Schematic diffraction pattern of a crystalline sample for a gaussian distribution of disorientation. The Bragg reflections become arcs proportional to the angular spread in $D(\alpha)$ centered on the origin of the reciprocal space.

the continuous intensity (Fig. 3.5(c)). Rotational and screw disorder affect the pattern rather differently (Fig. 3.5(d) and (e)): Bragg reflections in higher-order Bessel terms are suppressed, while peaks close to the meridian are unaffected for rotational disorder. In contrast, random screw disorder decreases the Bragg intensities in higher-order layer lines, but Bragg reflections persist further from the meridian [54]. In a "real" sample, these different forms of disorder do not appear separately, but rather a combination of them will occur. This leads to a further decrease of the Bragg intensities, dependent on the particular degree and combination of the disorder types. This unavoidably leads to an uncertainty in their analysis, as due to the cylindrical average, different types of disorder can lead to the similar diffraction pattern.

It is important to note, that, while these disorders change the relative amplitudes of the Bragg reflections and increase the continuous pattern, the peak positions remain unaffected. As soon as the Bragg peaks are discernible contributions to the diffraction pattern, they can be used to extract information on the layer line positions, and therefore the symmetry of the fibers.

3.3.3 The Effect of Disorientation – The Powder Average

The description so far assumed a perfectly parallel array of molecules. If the molecular axes are oriented about a texture axis in accordance with a distribution function $D(\alpha)$, the Bragg reflections of a polycrystalline sample become arcs or – in the case of completely random distribution, where $D(\alpha) = \text{const.}$ – rings centered on the origin of the reciprocal space (fig. 3.7).

As simple as this problem is in general, as complicated is the correct calculation of the scattering pattern of such a disoriented sample. Some limiting or simple cases have been considered in literature [59–61], but a general solution is not available.

In the case of a polycrystalline sample, where the bundles are straightened but randomly oriented, the diffraction pattern is affected in the same way as it is by a powder average in classical crystal diffraction: The spots become rings with a radius which is the same as the distance to the origin for the single spot. To calculate the one-dimensional

diffraction intensity, one has to angularly average the cylindrically averaged diffraction pattern of the polycrystalline sample by substituting $q_r = q\cos\chi$ and $q_z = q\sin\chi$ and integrating over χ.

The opposing case is the most highly disordered of chain molecules, which is called the amorphous phase. In contrast to the bundled specimen, the chains in an amorphous phase are not straightened but coiled up depending on the persistence length of the molecule. Such unoriented specimens give a few diffuse rings with a strong background. There is no model how to calculate the diffraction pattern, except for some crude simplifications and assumptions about the flexibility (and thus mutual interference) or arrangement of the filaments.

Partial Alignment

As discussed above, the success of a SAXS experiment will depend on the quality of sample preparation, in particular in reducing the disorder and disorientation as best as possible. A perfectly parallel alignment of filaments or bundles is experimentally challenging. Due to the diamagnetic anisotropy of the α-helical regions of the actin monomer, it is possible to produce highly well-oriented crystalline sols of F-actin in high magnetic fields with a strength of $>10\,\mathrm{T}$ [62]. However, actin filaments or their bundles spontaneously align with one another when concentrated above a certain threshold concentration. This effect is amplified by the spatial confinement in the capillary and the increase in persistence length for bundled networks.

This partial alignment has one important advantage over a randomly oriented sample: It opens up the possibility to distinguish between intra-filament and inter-filament correlation peaks. As illustrated in fig. 3.7, the inter-filament correlation peaks are located symmetrically around the equator, while the peaks on the off-equator layer lines do not touch the equator as soon as the partial alignment is good enough. Integrating in the diffraction pattern wedges along q_r will therefor contain almost exclusively inter-filament correlation peaks.

3.4 Continuous Twisting and Stretching of the Helix

The selection rule (3.24) directly reveals that even a small change in the helical symmetry will drastically effect the diffraction pattern. Since the description of the twist by k residues in v turns is "discrete", even small changes in the symmetry lead to enormous changes in the characteristic parameters. The layer line distance $d = vc$ for example changes while overtwisting the actin filament by only 1° per monomer ending up in a symmetry of -28/13 by a factor of 6/13 ($= v_1/v_2$). The redefinition of the selection rule practically doubles the layer line density in reciprocal space (Fig. 3.8). This discontinuity in the diffraction pattern as response to a continuous twist of the helix complicates the analysis.

A way out of this dilemma is provided by the fact that Bessel functions of higher order contribute only weakly to the diffraction pattern. Fortunately, it turns out that the Bessel functions contributing the most are the same for all helical symmetries.

Moreover, also the parameter m has a corresponding conserved pattern. This is exemplarily shown in table 3.1 and illustrated in Fig. 3.8 for two different symmetries. The only layer lines which will contribute significantly to the scattered pattern in fiber diffraction experiments will be the layer line with $n = 0$ positioned at the equator and the $n = \pm 1$ layer lines located at around $q_z \approx 1.2\,\mathrm{nm}^{-1}$.

The continuous twisting and stretching turns l into an inappropriate parameter. It is more convenient to re-express l, which appears only in the calculation of the layer line position along q_z (see (3.24)), by using the conserved parameters n and m and the monomer spacing h.

$$q_z = 2\pi \frac{m + nv/k}{h} \tag{3.41}$$

Based on this, modeled diffraction patterns can be calculated by continuously changing the helical symmetry v/k and the monomer spacing h.

-13/6			-28/13		
l	m	n	l	m	n
0	0	0	0	0	0
			1	-6/7	-13/15
1	1	2	2	1	2
			3	-5	-11
2	2	4	4	2	4
			5	-4	-9
3	3/-3	6/-7	6	3	6
			7	-3	-7
			8	4	8
4	-2	-5	9	-2	-5
			10	5	10
5	-1	-3	11	-1	-3
			12	6	12
6	0	-1	13	0	-1
			14	7/-6	14/-14
7	1	1	15	1	1
			16	-5	-12
8	2	3	17	2	3
			18	-4	-10
9	3	5	19	3	5
			20	-3	-8
			21	4	7
10	-2/4	-6/7	22	-2	-6
			23	5	9
11	-1	-4	24	-1	-4
			25	6	11
12	0	-2	26	0	-2
			27	7/-6	13/-15
13	1	0	28	1	0

Table 3.1: Comparison of the layer line contributions for two different helical symmetries. Small changes in the symmetry (here only 1° per monomer) drastically alter the layer line density. While the pattern in n and m is conserved.

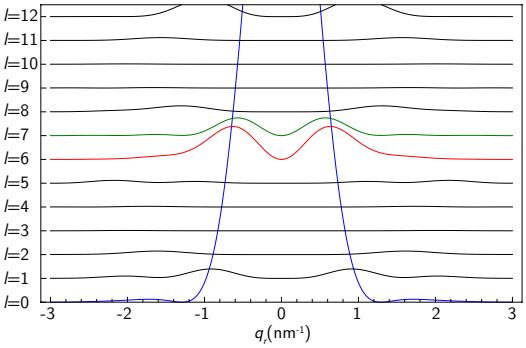

(a) Symmetry -13/6

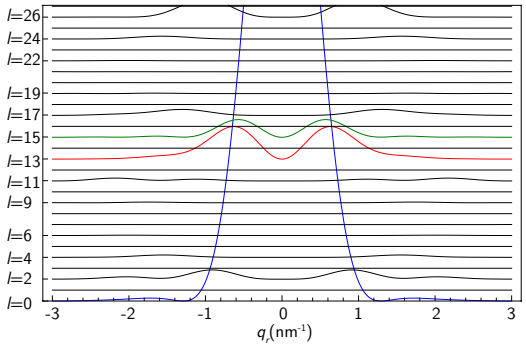

(b) Symmetry -28/13

Figure 3.8: Comparison of the layer line contributions for two different symmetries, generated using the 4-sphere model of the actin monomer (3.2.4). The layer line number is labeled on the left l, the order of the corresponding Bessel function can be found in table 3.1. The most intense contributions (highlighted in color) are found in layer lines 0, 6 and 7 corresponding to $n = 0, 1, -1$ in the case of (a). Changing the symmetry slightly (b), the 1^{st} order Bessel functions are positioned at $l = 13$ and $l = 15$, respectively.

Chapter 4

Finite Size of F-actin Bundles

Bundles of filamentous actin are key components of the eukaryotic cytoskeleton and are generally used for mechanical support. In filopodia, microvilli and stereocilia, F-actin bundles fortify cellular protrusions, in stress-fibers they help to maintain cellular integrity. The appearance of parallel F-actin bundles is tightly controlled by a myriad of actin binding proteins (ABPs). Moreover, cytoskeletal processes that involve F-actin bundles typically all employ their own complements of multiple ABPs [1]. Although this is probably at least partly related to the specific mechanical requirements of the different structures [63], the well-defined length, thickness and organization of the various cytoskeletal F-actin bundles might necessitate the use of a combination of different ABPs. Loss of one of the ABPs usually affects either the organization or the thickness of the bundles [3, 64], mutations often result in diseases [4, 5]. This finely matched interplay of actin and ABPs is a fascinating example for the morphological self-organization in living cells [65].

However, the finite size effect of bundle structures is not restricted to living organisms. *In vitro*, charged biopolymers such as F-actin, microtubules, or DNA generally form a phase of bundles of well-defined thickness in the presence of non-adsorbing polymer and/or multivalent counter-ions [9, 66–69]. Several concurring mechanism have been discussed to define bundle length and thickness: The stabilization mechanism of counter-ion induced bundles has been proposed to be similar to that of colloidal clusters [70, 71]; steric and short range electrostatic interactions or frustration within the bundles prevent charge neutralization and limit the bundle size [72]. Alternatively, the finite size of chiral biopolymers might be due to a build up of in-plane shear elastic stresses [73] which sometimes result in braided structures [74].

In this chapter, the experimental results on an *in vitro* actin model system are reported. They suggest an altogether novel mechanism limiting the bundle size: The frustration is caused by a mismatch between the helical structure of individual actin filaments and the geometric packing constraints within bundles. The first section gives some experimental details about SAXS experiments on actin bundle networks (sec. 4.1). In section 4.2, the results of preceding microscope experiments performed by M.M.A.E Claessens are presented. TEM micrographs and fluorescence experiments in confined volume show that actin/fascin bundles feature a well-defined size in dependence of the fascin concentration and are limited to a maximal thickness of about 20 filaments. Motivated by these findings, the assembly of filaments in the bundle has been studied by Small Angle X-ray Scattering (SAXS) in the course of this thesis. For fascin (sec. 4.3) and espin (sec. 4.4), the filaments build a hexagonally organized bundle where the single

filaments are overtwisted to overcome the mismatch between the chirality of the single filaments and the hexagonal packing in the bundle. In sec. 4.5, the energetic trade-off between filament twisting and crosslinker binding within a bundle is discussed as a possible mechanism to precisely control the bundle size. A combination of different ABPs allows building the thicker bundles that are observed in living cells (sec. 4.6).

4.1 SAXS Experiments

Sample preparation For Small Angle X-Ray Scattering (SAXS) experiments, the actin networks were polymerized in 1.5 mm quartz capillaries[1] and sealed with vacuum grease or using a Bunsen burner to prevent evaporation. For the second beam time (sc2386), the sample polymerized for 1 h before they were centrifuged for 2 h at 5000 g. This sediments the F-actin into a dense pellet in order to enhance the scattering signal. Only networks in the bundle regime formed pellets. Control experiments revealed that there were no structural differences between pelleted and non-pelleted samples (cf. fig. 4.6).

Data acquisiton The SAXS experiments were performed at the ID-02 beamline at the ESRF in Grenoble. The scattering was done with X-rays of 0.995 Å($\widehat{=}$ 12.47 keV) and a sample-to-detector distance of 1 m and 7 m. Scans were performed with an exposure time of 0.5-6 s, always checking if radiation damage or saturation occurred. The scattered radiation was detected by a FReLoN Kodak CCD camera. The beam center and exact detector distance were calibrated using a silver behenate (AgBE) sample and fitting circles to the diffraction pattern. For the second beam time at the ESRF (sc2386), this calibration failed due to a small drift in the detector position. In this case, the beam center was fitted individually for each sample, where rings of scattered intensity appeared in the 2D pattern, based on the *tilt* function in Fit2d[2]. The diffraction data was analyzed and integrated wedges along the radial direction q_r and axial direction q_z were obtained using the matlab based *EDFplot* and *datatools* in *SAXSutilities*[3]. For samples featuring shifted beam centers, the customized script *ccd_recenter.bat* written by the ESRF beamline scientist M. Sztucki was used for angular integration. The multiple exposures of the same sample were averaged, using the corresponding exposure times as weight factors.

Limitations on resolution The typical diffraction patterns of biomolecular self-assemblies are usually quite broad if compared to the resolution-limited Bragg peaks of perfect crystals. However, the calculation of domain sizes in scattering crystallites requires to correct for the instrumental resolution limit. This depends on various factors: the divergence of the X-ray source, the relative cross-sections of beam and sample, the finite pixel size on the detector, and non-monochromaticity of the X-ray beam.

[1] Glas-Technik & Konstruktion, Müller & Müller OHG, Germany
[2] http://www.esrf.eu/computing/scientific/FIT2D/
[3] http://www.sztucki.de/SAXSutilities/

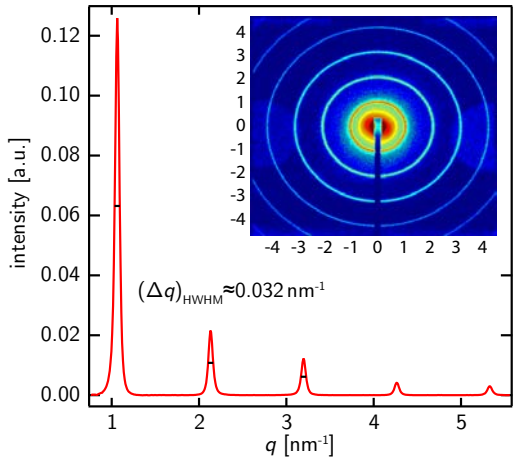

Figure 4.1: Circularly averaged and background subtracted intensity profile of an AgBE sample for calibration issues. Beside fitting the beam center and detector distance from the well known peak positions, one can use the peak widths to estimate the resolution limit of the system. The inset shows the corresponding 2D diffraction pattern.

Thus, the measured peak width results from two contributions: the finite domain size of the sample itself (or effects of lateral disorder) and the resolution limitation of the measuring system, which are connected by convolution (sec. 3.3.2).

$$(\Delta q)_{\text{measured}} = \sqrt{(\Delta q)^2_{\text{sample}} + (\Delta q)^2_{\text{system}}} \tag{4.1}$$

An approximation of the systematic limitation can be derived from the peak width of an silver behenate sample which is used for detector calibration issues. Due to the rather small crystallite sizes of around 90 nm, AgBE is not ideally suited to calibrate the instrumental broadening, but it provides a rough estimate of $(\Delta q)_{\text{system}}$ [75]. After subtraction of backgrounds, the remaining intensity profile is fitted by the sum of several Gaussians (fig. 4.1). Based on their average width of $(\Delta q)_{\text{HWHM}} \approx 0.032\,\text{nm}^{-1}$, the instrumental broadening can be calculated to $(\Delta q)_{\text{system}} \approx 0.006\,\text{nm}^{-1}$ using the Scherrer equation (3.37). Compared to the typical peak widths in the diffraction patterns of actin bundles that are at least $0.04\,\text{nm}^{-1}$, the instrumental resolution can be neglected.

4.2 Finite Size in Microscopy Experiments

Although there are indications that, *in vitro*, the diameter of F-actin/ABP bundles is well defined, reconstructed actin/ABP bundles are usually embedded in a continuous isotropic background network. This prevents a clear description or quantitative analysis [8]. In contrast, the ABP fascin organizes actin filaments into a crosslinked network of bundles in which no single filaments can be observed [22]. This makes the reconstituted F-actin/fascin system ideally suited to resolve the mechanism underlying the finite size of F-actin bundles. Fascin bundles display a uniform thickness and are straight over long distances reflecting their high bending rigidity [63].

Fluorescence micrographs indicate that the bundle thickness is independent of the actin concentration and depends exclusively on the molar ratio between bound fascin and G-actin, R^* (cf. sec. 2.2): If the actin concentration is increased while $R = 1$ is kept

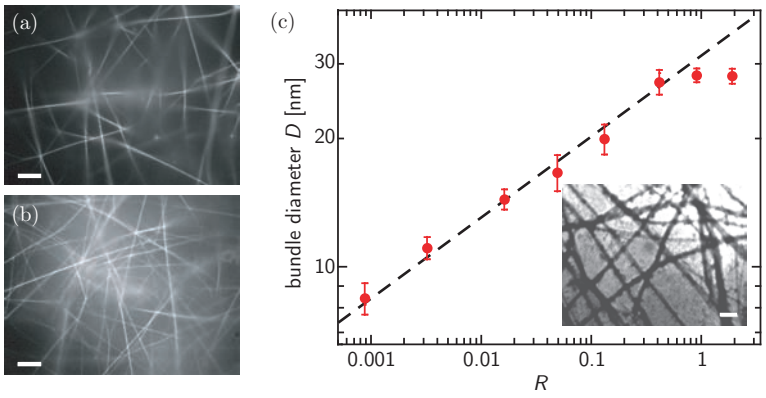

Figure 4.2: Finite and limited thickness of F-actin/fascin bundles. (a)-(b) Fluorescence micrographs of TRITC phalloidin-labeled actin/fascin bundles ($R = 1$). Increasing the actin concentration from $c_A = 0.04\,\mathrm{mg/ml}$ (a) to $c_A = 0.1\,\mathrm{mg/ml}$ (b) merely increases the number of actin bundles per unit volume and seems to have no effect on the bundle thickness. (Scale bars: 10 µm.) (c) Bundle diameters D obtained from TEM micrographs (Inset, scale bar: 0.2 µm) as a function of the relative fascin concentration R^* ($c_\mathrm{A} = 0.1\,\mathrm{mg/ml}$).

constant, the bundle thickness remains unchanged while the number of actin bundles per unit volume rises (fig. 4.2(a),(b)). The absolute values of the bundle diameter D as a function of R are extracted by Gaussian fits to the intensity profiles in electron micrographs (fig. 4.2 (c) Inset). For this, the fascin concentration R is varied while the actin concentration is kept constant. The bundle width distributions obtained in this way are very uniform and show a slight increase of D with the relative fascin concentration $D \sim R^{0.3}$ (fig. 4.2(c)). Interestingly, D reaches a plateau at $R \approx 0.25$; a further increase of the fascin concentration has no influence on the bundle diameter. The observed thickness of F-actin/fascin bundles is independent of the preparation procedure. Whether long or shortened filaments are incubated with fascin, or fascin is already present during the polymerization process does not affect the bundle thickness.

To precisely quantify the finite and limited thickness of actin bundles, a mesoscopic system is advantageous. A system of emulsion droplets is extremely well suited for this purpose due to the confined volume [76]. At small droplet diameters, D_d, F-actin filaments bundle into a single ring in the presence of fascin (fig. 4.3(a)) [63]. With increasing droplet diameter this ring splits up and side branches arise (fig. 4.3(b)). In the largest droplets, complicated structures built of several rings are found (fig. 4.3(c)). The total mass of F-actin within a drop is equivalent to its total length L. This can be computed very precisely from the actin concentration c_A and the droplet diameter D_d. The bundle radius can be measured and – for the case of a single ring – the number of filaments n_f aligned parallel in the bundle can be deduced assuming a homogenous bundle with along the actin ring. In this way, in dependence of c_A and D_d, a transition from single rings to more complicated structures can be observed (fig. 4.3(e)): The maximal number of filaments in a single bundle does not exceed ∼20 filaments. Instead of growing thicker rings, filaments rather organize into more bundles if the droplet diameter or the actin concentration increases.

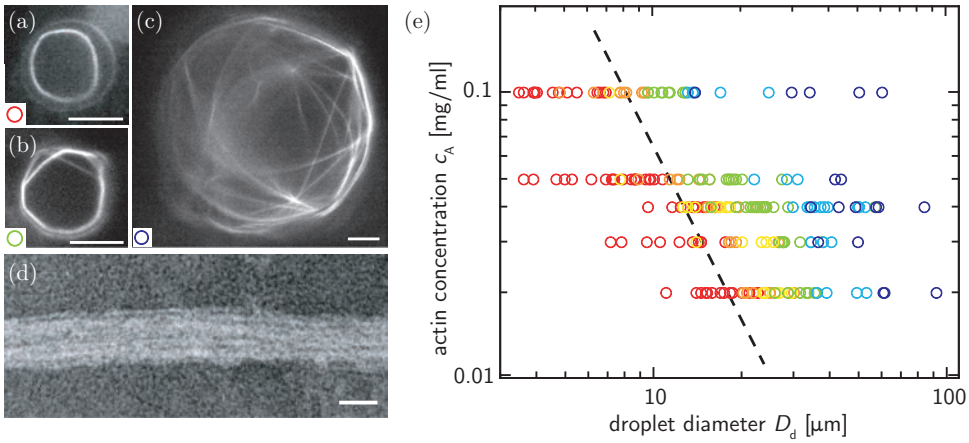

Figure 4.3: F-actin/fascin bundles in confinement. (a–c) Fluorescent micrographs of TRITC phalloidin-labeled F-actin/fascin bundles ($R^* = 1$). For small-droplet diameters filaments organize into a single ring (a), in larger droplets a second bundle appears (b), and in very large droplets more complicated structures are found (c). (Scale bars: 10 µm.) (d) TEM micrograph of a detail of an actin bundle obtained from the confined rings showing the typical bundle diameter of 5 filaments. (Scale bar: 20 nm.) (e) The organization of actin bundles as a function of the actin concentration c_A and emulsion droplet diameter D_d. The colors depicted in the diagram represent the different structures presented in (a)-(c). A single bundle does not grow thicker than 20 filaments, and the dotted line represents $n_f = 20$.

TEM micrographs of actin rings extracted from emulsion droplets show closely packed F-actin/fascin bundles with a typical diameter of five to six filaments (fig. 4.3(d)). Considering the expected hexagonal packing ([77] and sec. 4.3), this is in excellent agreement with the maximum of ∼20 filaments per bundle derived from fig. 4.3(e). This leads to the conclusion that the plateau in $D(R)$ for $R > 0.25$ is reached when the bundle contains ∼20 filaments (fig. 4.2(c)).

Based on the observed maximum bundle thickness of ∼20 filaments and the scaling of $D \sim R^{0.3}$ (fig. 4.2(c)) it is possible to derive that, for bundles with $n_f < 20$, not all possible crosslinker binding sites are occupied, while the maximum size observed experimentally corresponds to a full occupation of all possible binding sites. This is shown by a geometrical argument: The amount of ABPs that can bind to a filament is limited, fascin binding saturates at a ratio of 1 fascin molecule to ∼4.5 actins [78]. At saturation, an actin filament with 6 fascin binding sites therefore consists of ∼13–14 actin monomers. Assuming that all bundle have the same thickness, one can calculate the number of binding sites n_{ABP} and, thus, the maximal ratio R^* of bound ABPs to actin monomers n_a in dependence of the number of filaments in the bundle, n_f:

$$n_{ABP}/n_a = R^* = 1/u(3 \pm 3.5 n_f^{-1/2}), \tag{4.2}$$

where u is the number of actin monomers necessary to build one hexagonal unit. The ± sign refers to whether surface occupation is included or not. For building less but thicker bundles that are fully saturated with crosslinking molecules, decreasing

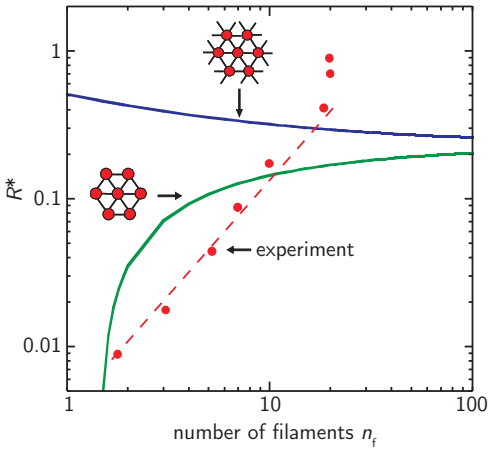

Figure 4.4: Maximal ratio R^* between bound ABP and actin monomers as a function of bundle thickness n_f. At a constant actin concentration, a system of fully saturated bundles would require decreasing amount of crosslinkers with increasing n_f (blue line). Inside occupation would require increasing amounts of ABP (green line). In the experimentally observed bundles, the fascin binding sites are not fully occupied for $n_f < 20$ (filled circles). u was held constant and was assumed to be 13.

amounts of crosslinkers are needed. To compare the R^* values corresponding to fully saturated bundles of n_f filaments to the experimentally observed values, the $D(R^*)$ curve depicted in fig. 4.2(c) has to be transformed into $R^*(n_\mathrm{f})$. Therefore, it is assumed that the maximal bundle thickness in TEM experiments corresponds to $n_\mathrm{f} \approx 20$ observed in confinement. The experimental results for $R^*(n_\mathrm{f})$ lie below the theoretical curves (fig. 4.4); for bundles with $n_\mathrm{f} < 20$, not all possible crosslinker binding sites between the filaments of the bundle are occupied. With increasing n_f, the degree of binding site occupation increases until full occupation is reached at $n_\mathrm{f} \approx 20$ (fig. 4.4).

It is not clear *a priori* why bundles of such well-defined diameters are observed, or what causes the bundle thickness to be limited. The bundle diameter could be constrained in principle either kinetically [79–81] or thermodynamically [72, 73]. However, the independence of the bundle diameter on the preparation method and the system used, strongly suggests an equilibrium mechanism. While charge accumulation has been suggested to prevent clusters of charged colloidal particles and counter-ion induced F-actin bundles to grow beyond a certain size [72, 82], this can not be the case for ABP/F-actin bundles. The surface separation between F-actin filaments bundled with fascin is approximately 5 nm (sec. 4.3), much larger than the Debye length at the ionic strength used. Decreasing the salt concentration to the minimum necessary for actin polymerization (2mM $MgCl_2$, no KCl or $CaCl_2$) has therefore no influence on the maximum F-actin/fascin bundle thickness. As electrostatic repulsion between actin filaments is too short ranged to affect bundle assembly, other mechanisms have to be responsible for preventing bundles from growing thicker.

4.3 Microscopic Structure of Fascin Bundles Using SAXS

The growth of the bundles is not prevented by a lack of ABP but instead seems to be physically limited to two hexagonal shells of actin filaments, comparable to those found in filopodia [83]. To investigate the microscopic bundle geometry and the underlying size limiting mechanism in more detail, the bundle structure is analyzed in SAXS

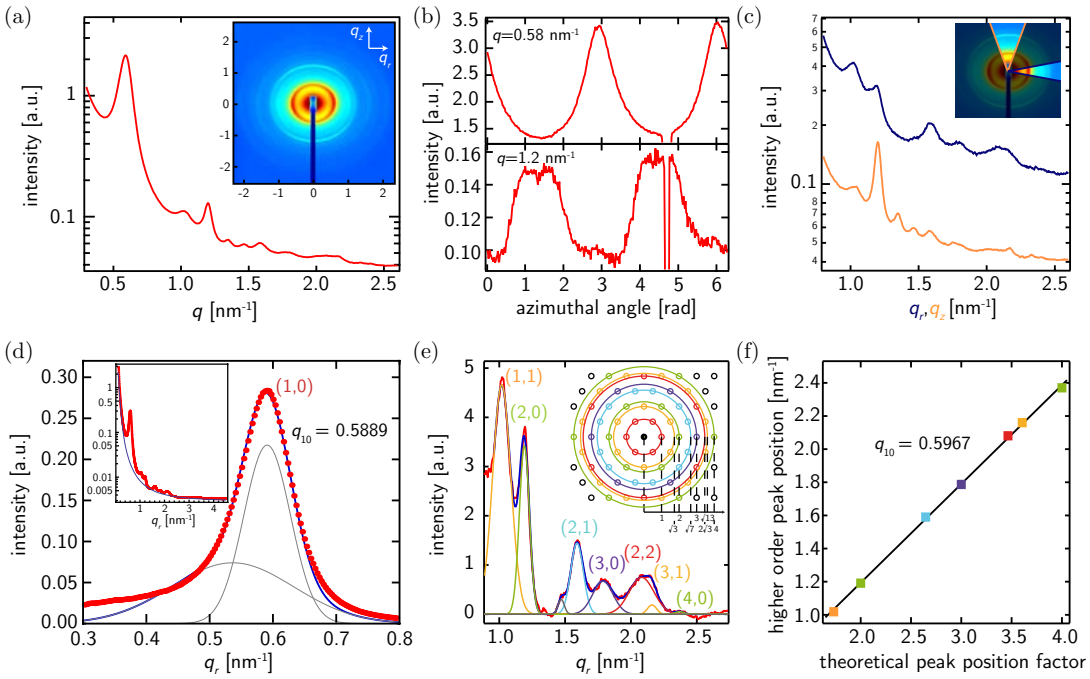

Figure 4.5: Scattering pattern of actin/fascin bundles ($R^* = 1$): (a) Circularly averaged scattering intensity of a partially aligned 2D diffraction pattern (inset). (b) The azimuthal dependence of the peaks at $q = 0.58\,\mathrm{nm}^{-1}$ and $q = 1.2\,\mathrm{nm}^{-1}$ reveals that they are positioned at axes perpendicular to each other. (c) Angularly averaged wedges along the radial (q_r) and the axial (q_z) directions of the diffraction pattern allows separation of the peak contributions. (d) Background subtracted intensity profile in q_r direction. The background was subtracted by a pseudo-Voigt fit to the data (blue curve, inset). Two Gaussian are needed to fit the peak profile due to improper background subtraction. (e) Gaussian fits to the higher order peaks in the background subtracted intensity profile reveal the hexagonal packing of the filaments in the bundle. (f) The higher order peak positions are plotted versus the theoretically expected factor to the q_{10} position in a hexagonal lattice. The slope returns a more precise determination of q_{10}.

experiments.

4.3.1 Hexagonal Packing of Fascin Bundles

Fig. 4.5(a) depicts a typical circularly averaged intensity profile of partially aligned F-actin/fascin bundles at $R = 1$. The inset shows the corresponding 2D diffraction pattern. The multitude of sharp peaks indicates that fascin forms well organized actin bundles. Due to the partial alignment, the peaks do not form homogenous rings but are centered around different directions. This allows distinguishing between inter- and intrafilamental correlations (cf. sec. 3.3.3). Comparison of the azimuthal dependence of the intensity of the peaks located at $q = 0.58\,\mathrm{nm}^{-1}$ and $q = 1.2\,\mathrm{nm}^{-1}$, respectively, shows that they are positioned at perpendicular orientations in the $q_r q_z$-plane, the first peak close to the q_r axis, the second close to the q_z axis (fig. 4.5(b)). This second

peak at $q = 1.2\,\mathrm{nm}^{-1}$ is not exactly centered at this axis but features two maxima in azimuthal dependence. This corresponds to the expectation for intrafilamental peaks around q_z (cf. sec. 3.3.3).

For a further analysis, the scattering intensity is averaged over wedges along q_r and q_z to minimize the crosstalk between the two directions (fig. 4.5(c)). This angular separation allows distinct allocation of the peaks to the q_r and q_z directions, respectively. To get the precise peak positions and widths, the continuous background is subtracted by fitting a pseudo-Voigt function to the continuous intensity profile without peaks (fig. 4.5(d) inset). The residual intensity profile is fitted by Gaussian functions. However, the first peak, q_{10}, is only insufficiently described by a single Gaussian (fig. 4.5(d)), probably due to improper background subtraction. Beyond the dependence on the form factors of filament and bundle, the continuous intensity profile accounts also for the Bessel function J_0 of the 0^{th} layer line. Beside modulating the intensity, the Bessel function may also distort the peak shape and influence the peak $q_{10} = 0.589\,\mathrm{nm}^{-1}$ position as reported before [84].

Besides the (1,0)-peak, several peaks of higher order can be identified by a sum fit of several Gaussians. The peak positions found at $q_{11} \approx \sqrt{3}q_{10}$, $q_{20} \approx 2q_{10}$, $q_{21} \approx \sqrt{7}q_{10}$, $q_{30} \approx 3q_{10}$, $q_{22} \approx 2\sqrt{3}q_{10}$, $q_{31} \approx \sqrt{13}q_{10}$ indicate the hexagonal packing of fascin bundles (sec. 3.3.2). This has been shown before for actin needles *in vivo* [77]. The higher order peak positions can be used to render the position of the (1,0)-peak more precisely, which is mandatory for an exact analysis of the intrafilamental symmetry (sec. 4.3.3). The curve progression of the form factor and the 0^{th} order Bessel function are more flat in this q-regime; therefore peak positions are less sensitive to changes in the background subtraction and the multiplication with J_0. In fig. 4.5(f) the peak positions are plotted versus the theoretically expected factor in the hexagonal lattice. The resulting $q_{10} \approx 0.597\,\mathrm{nm}^{-1}$ is slightly larger than the original value. Due to the robustness against changes in the bundle form factor and in the background subtraction, the fit through the higher order peaks is more reliable.

The result for q_{10} corresponds to a center-to-center distance between the individual actin filaments of the hexagonal lattice of $a = \frac{4\pi}{\sqrt{3}q_{10}} \approx 12.2\,\mathrm{nm}$. It is in good agreement with a filament diameter of about 7 nm [11], the size of the fascin molecule of 5 nm, and with measurements on actin needles extracted from sea urchin oocytes [77].

4.3.2 Concentration Dependence of the Bundle Domain Size

SAXS measurements also show the dependence of bundle thickness and fascin concentration. Decreasing R leads to distinct changes in the scattering pattern (fig. 4.6(a)): The peak amplitudes decrease and the peaks broaden until they nearly vanish around $R < 0.02$. This value is in good agreement with the bundling threshold ($R_{\text{crit}} \approx 0.01$) observed in fluorescence microscopy and macrorheology [22].

An analysis of the higher order peak positions shows that the bundles are still hexagonally packed. The q_{10} position does not change with changing fascin concentration and is perfectly reproducable (fig. 4.6(b)). Changes in the salt conditions (e.g. replacing NaCl by KCl or omitting this additional monovalent salt) also have no effect on bundle size and geometry.

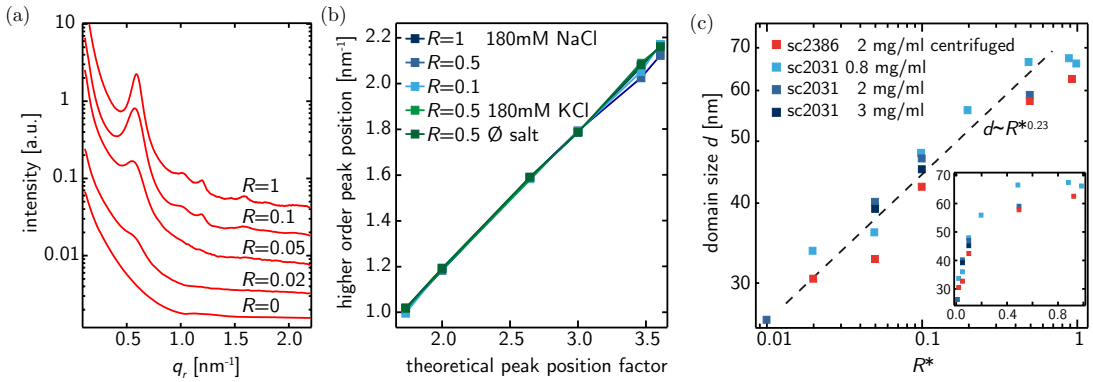

Figure 4.6: R dependence of actin/fascin bundles: (a) Angularly averaged intensity over wedges along the q_r direction. The peak amplitudes increase and the widths decrease with the fascin concentration R and completely vanish around $R \approx 0.02$. (b) The higher order peak positions are in good agreement with the theoretical values expected for hexagonal packing. The slope and thus the position of the q_{10} peak remains unaffected by changes in R or the salt conditions. (c) The bundle domain size d increases with increasing fascin concentration R^* until it saturates around 65 nm. Data of different beam times (sc2301 and sc2386) and thus different protein preparations and sample preparations collapse. The inset shows the same data in linear scale.

The width of the Gaussian q_r peaks does not correspond to the exact diameter of the bundle. Instead, it allows conclusions on the domain size in the bundle which reflects the finite size as well as the lateral disorder in the bundle (sec. 3.3.2). The multiplication with the 0^{th} order Bessel function and the insufficient background subtraction slightly disturbs the shape of the Gaussian (1,0)-peaks. This prevents a precise Gaussian fit and determination of the peak width. Less sensitive is the full width at half maximum or – even better – the dexter half width at half maximum (HWHM). According to the Scherrer equation, the bundle domain size can be derived from the resolution corrected $(\Delta q)_{\text{HWHM}}$ (cf. equation (3.37)):

$$d \approx 0.9 \frac{\pi}{(\Delta q)_{\text{HWHM}}} \tag{4.3}$$

The resulting d in dependence of the fascin concentration is displayed in fig. 4.6(c). Independently of the actin concentration and the preparation method (centrifuged or solution), the domain size d increases with R^* according to $d \sim R^{*0.23}$ until saturation occurs at $R^* \approx 0.4$. The qualitative behavior, the power-law exponent and the bundle saturation are in good agreement with the bundle thicknesses D measured by electron microcopy (fig. 4.2(c)).

Assuming the maximum of 20 filaments per bundle (fig. 4.3(e)), a hexagonal packing of the filaments in the bundle and an interfilamental distance of $a = 12.2$ nm, a bundle diameter of $D \approx 4a \approx 50$ nm is expected. However, the bundle thickness determined by electron microscopy is $D \approx 30$ nm (sec. 4.2). This slight mismatch to the SAXS data might be owed to several approximations in the data evaluation. In the case of the SAXS data, inaccuracies in background subtraction distort the Gaussian shape and

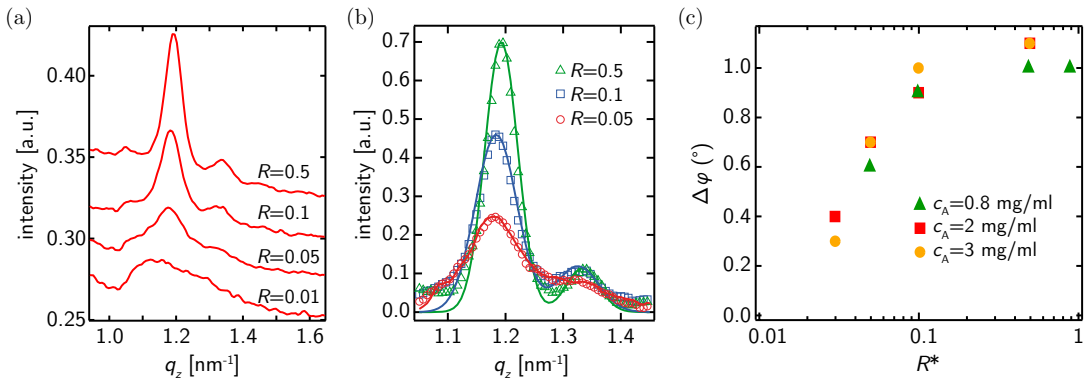

Figure 4.7: Helical twist of the actin filament in dependence of R: (a) Angularly averaged intensity over wedges along the q_z direction ($c_\mathrm{A} = 2\,\mathrm{mg/ml}$). The scattering profile changes from a continuous pattern to single peaks. (b) Background subtracted q_z data. The peak positions shift slightly with R. The continuous lines are fits to the data. (c) The overtwist angle per monomer obtained from fits to the diffraction pattern for various actin concentrations. It increases with R^* until it saturates at $\approx 1°$ for $R^* \gtrsim 0.5$.

tend to overestimate of d. Opposed to this, the measured value has to be corrected for the staining layer thickness in order to derive the actual bundle size from electron micrographs. An overestimated correction factor will lead to too small values for the bundle thickness.

4.3.3 Correlation of Filament Twist and Bundle Thickness

So far, only the intensity profile along q_r that corresponds to inter-filamental correlations has been regarded is analyzed. An evaluation of the scattering profile along q_z is presented in this section. It reveals information about the intra-filamental distances and thus about the helical symmetry of the actin filaments (sec. 3.3.3). Fig. 4.7(a) shows the intensity profile for actin fascin/bundles at various R values. The most remarkable change with increasing fascin concentration is the conversion from a broad diffraction pattern at low R to quite narrow Gaussian-like peaks for $R \gtrsim 0.01$. In the absence of fascin or at concentrations not sufficient for bundling, the scattered intensity reflects the continuous pattern of the 6^{th} and 7^{th} layer line ($n = 1$ and $n = -1$ Bessel functions) of the native -13/6 actin helix. Due to the decrease in amplitude with increasing order of the Bessel function, these layer lines dominate the diffraction pattern of partially aligned F-actin solutions (sec. 3.2.3).

As the filaments form bundles, the native layer line pattern is convoluted with the hexagonal bundle structure. The layer line pattern appears only at spots along q_z in columns located at q_r values which correspond to the hexagonal lattice vectors (sec. 3.3.2). This results in a splitting up into several sharp peaks.

At intermediate fascin concentration ($R = 0.05$), the pattern is a mixture of the continuous pattern and these Bragg reflections. This could either indicate a two-phase system where quite perfect bundles are embedded in an amorphous network or alternatively a substitutional disorder in the packing of the filaments in the hexagonal lattice

(sec. 3.3.2). Fluorescence and electron microscopy experiments show a sharp transition between crosslinked and bundled phase; no composite phase or microdomains can be observed [22]. This supports the disorder inside the bundle as the more likely explanation. As the amplitude of the Bragg peaks is approximately n_f times larger than the continuous contribution, where n_f denotes the number of filaments in the bundle, the continuous pattern is only discernible at small bundle sizes. Moreover, larger fascin concentration corresponds to a rising number of crosslinks per filament and will decrease the substitutional disorder.

Besides the drastic transition from the continuous to the peak-shaped pattern, an increase of fascin concentration slightly shifts the positions of the Bragg peaks. This indicates a change in the helical symmetry of the actin filament in the bundled phase. This is bets visible in the background subtracted data shown in fig. 4.7(b). In the analysis, the extracted helical symmetry is obtained by comparing the experimental data with theoretically modeled intensity patterns: The layer lines of the model are calculated starting from the Fourier transforms of the Holmes coordinates for the actin filament, combined with the standard four-sphere model. Substitutional disorder in the filament is incorporated by a Gaussian-shaped layer line thickness. For bundled networks, this is multiplied with the reciprocal hexagonal lattice. To account for powder averaging, the one-dimensional diffraction pattern is calculated by substituting $q_r = q\cos\chi$ and $q_z = q\sin\chi$ with $q = 4\pi|\sin\theta|/\lambda$ in equation (3.31) and numerically integrating over χ. Starting from the Holmes model with the native -13/6 symmetry, theoretical patterns are calculated for different values of monomer spacing, twist angle and peak width.

Minimizing the chi-square between the measured diffraction pattern and the calculated curves reveals an overtwisted state of the actin filament. The measured peak positions of 1.20, 1.35 and 1.46 nm^{-1} for high R values are in good agreement with the 13^{th} and 15^{th} layer line of a -28/13 symmetry. This corresponds to an overtwist of $\Delta\varphi \approx 1^\circ$ per actin monomer. This overtwist angle develops with increasing fascin concentration (fig. 4.7(c)): starting from the native -13/6 symmetry, the overtwist saturates at the maximum overtwist of -28/13 for $R^* \gtrsim 0.5$. This resembles the curve progression of the bundle thickness: Both, the bundle diameter measured by electron microscopy and the domain size obtained from the peak widths, saturate for similar R^* values. This indicates that the finite size of the fascin bundles correlates with the distortion of the actin filament in the bundle. A further discussion is given in sec. 4.5.

4.4 Microscopic Structure of Espin Bundles Using SAXS

The addition of the actin crosslinking protein espin results in a bundled network with an architecture resembling that of fascin networks. Both form long, straight and parallel actin bundles (sec. 2.2). The scattering pattern of espin bundles also shows very similar features as the fascin diffraction. Fig. 4.8(a) shows the 2D diffraction pattern of partially aligned actin/espin bundles at $R = 1$. Due to their distinct alignment, the numerous spots in the 2D pattern can be clearly assigned to the axial and radial contributions.

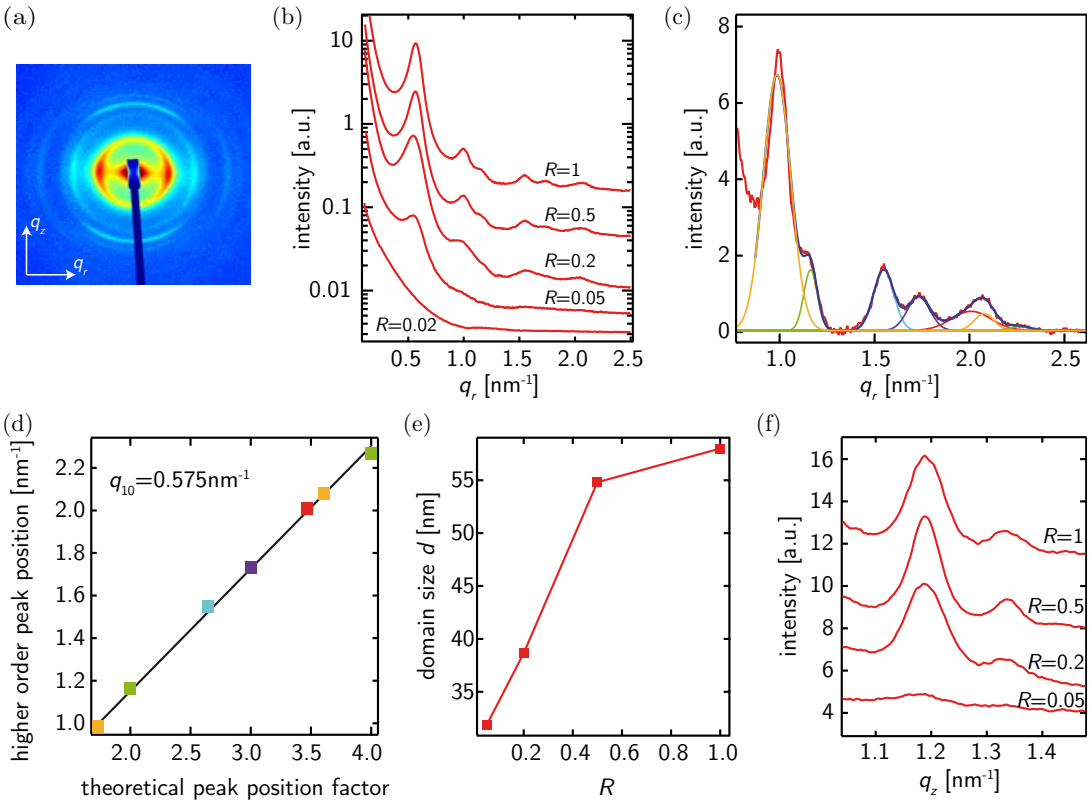

Figure 4.8: Diffraction on actin/espin bundles: (a) 2D diffraction pattern of partially aligned actin/espin bundles for $R = 1$. (b) Angularly averaged intensity over wedges along q_r for various R values. (c) Gaussian fits to the higher order peaks in the background subtracted radial data at $R = 1$. (d) The higher order peak positions obtained by the Gaussian fits in (c) are plotted versus the theoretically expected ratios to the (1,0) peak in a hexagonal lattice. (e) The bundle domain size d as a function of the espin concentration R. (f) Angularly averaged intensity over wedges along q_z. In the case of espin, the peak positions do not shift with R.

Following the analysis described in sec. 4.3, the intensity profile is averaged over angular wedges in q_r and q_z direction. As shown in fig. 4.8(b) for q_r, a peak at $\approx 0.57\,\mathrm{nm}^{-1}$ and several higher orders appear for $R \gtrsim 0.05$ and increase in amplitude with R. Fitting several Gaussians to the higher order peaks reveal again hexagonal packing of the filaments (fig. 4.8(c)): the peak positions are in excellent agreement with the theoretically expected ratios to the position of the (1,0)-peak in a hexagonal lattice (fig. 4.8(d)). The slope of the linear fit allows a precise determination of the peak position q_{10}. The value of $q_{10} = 0.575\,\mathrm{nm}^{-1}$ corresponds to an inter-filamental distance of $a_{\mathrm{esp}} = 12.6\,\mathrm{nm}$ in the hexagonal bundle, in good agreement with published data [43]. This value is slightly larger than $a_{\mathrm{fas}} = 12.2\,\mathrm{nm}$ observed for fascin.

The domain size d, that measures the bundle thickness convoluted with the substitutional disorder of the filaments in the bundle, can be derived by the Scherrer equation (3.37). The dependence of d on the espin concentration R is shown in fig. 4.8(e). The domain size increases with R and saturates for $R > 0.5$ around 55 nm. The qualitative

behavior as well as the quantitative values correspond to the fascin results.

A distinct difference to the fascin bundles is observed in the intensity profile along q_z. As discussed before, the q_z pattern reveals information about the intra-filamental symmetry and thus about the helical structure of the actin filament. Fig. 4.8(f) shows the intensity profile of the q_z-wedges as a function of R. The Gaussian peaks result from the convolution of the continuous intensity of the layer lines and the Bragg peaks of the hexagonal lattice. In contrast to the fascin measurements, the positions of these q_z peaks do not change with increasing espin concentration. As before, theoretical diffraction pattern for various helix parameters are calculated to obtain quantitative information about the helical symmetry. The helical lattice vectors had to be adapted to the larger inter-filamental distance. A comparison of these simulated patterns with the background subtracted intensity profiles returns a -28/13 symmetry as best fit. This corresponds to the results published in [43]. The measured overtwist of the actin helix is identical to the final state in the fascin bundles. However, it is the same for all espin concentrations and thus it does not correlate with the domain size or the bundle thickness.

4.5 Discussion

The SAXS experiments presented in the previous sections show that both ABPs, fascin and espin, form very similar bundle structures as already suggested by fluorescence micrographs. The intensity pattern along the radial direction q_r reveals the hexagonal packing of the filaments in the bundle. The characteristic inter-filamental distance a is very similar for both crosslinkers ($a_{\mathrm{fas}} = 12.2\,\mathrm{nm}$, $a_{\mathrm{esp}} = 12.6\,\mathrm{nm}$) and in good agreement with *in vivo* measurements of bundles where these ABPs dominate [77, 85]. For high R values, the Gaussian-shaped pattern without discernible continuous contributions found along q_z suggests quite rigid bundling; the domain size can be interpreted as a measure of the bundle thickness. This parameter also provides very similar results for both ABPs and reproduces the qualitative behavior of the bundle width measured by TEM: the domain size d increases with the crosslinker concentration until it saturates around 60 nm at $R^* > 0.5$.

Both crosslinkers drive a systematic overtwist in the actin filaments from their native -13/6 state. While fascin bundles feature a continuous spectrum of intermediate twist states, which seem to correlate with the bundle thickness, espin only allows one distinct twist state. The final -28/13 state of the fascin bundles is the same as the constant espin twist state. This value is in good agreement with the helical symmetry found in bundles from the acrosomal process in Limulus sperm [86], and it is slightly larger than the results obtained from stereocilia hair cells or extracts of F-actin needles from Sea Urchin ooyctes [77, 85].

Energetic estimate There is an ongoing discussion about disorder in the native actin helix and the width of the twist probability distribution observed by TEM for single actin filaments is quite broad [87, 88]. However, fixing the filaments in a new overtwisted position costs energy. The energetic cost involved in overtwisting F-actin is provided

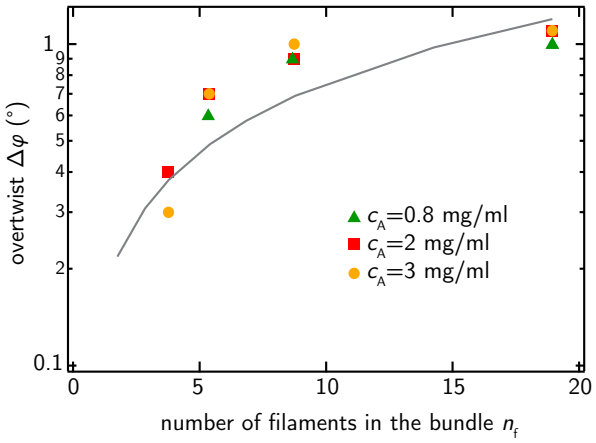

Figure 4.9: Energetic estimate of the gain in binding energy and the consumption for filament distortion in the case of fascin. The back line represents the maximal overtwist when all binding energy is converted into filament twisting.

by the binding energy released by the ABP. A rough estimate of the twist energy per actin residue as a function of R^* can be obtained from the torsional stiffness of a single actin filament, $\tau = 8 \cdot 10^{-26}\,\mathrm{Nm}^2$ [89], the residue spacing d_z and the observed increase in the overtwist $\Delta\varphi$:

$$E_{\mathrm{twist}} = \frac{\tau(\Delta\varphi)^2}{d_z} \tag{4.4}$$

The energy E_{ABP}, which each crosslinking molecule has to incorporate, ca be calculated by normalizing E_{twist} to the number of actually bound ABP: $E_{\mathrm{ABP}} = E_{\mathrm{twist}}/R^*$. In the case of fascin, E_{ABP} is approximately constant. Independent of the fascin and actin concentrations, the energy required for twisting is found to be $E_{\mathrm{ABP}} \approx 10 k_{\mathrm{B}}T$. Comparing this value to the binding energy of fascin, $\Delta G = k_{\mathrm{B}}T \ln(K_D) \approx 15 k_{\mathrm{B}}T$ [42], it turns out that the gain in binding energy is slightly larger than the loss in torsional energy.

Assuming that all binding energy is spent on filament twisting, the accessible overtwist can be calculated for each value of R^* or equivalently for its corresponding number of filaments in the bundle, n_{f}. $\Delta\phi(n_{\mathrm{f}})$ is shown in fig. 4.9: The calculations are in good agreement with the SAXS results for fascin bundles at different actin concentrations.

Finite Size The question remains what leads to the overtwist of the actin filaments and what is responsible for the different overtwist mechanisms for fascin and espin, despite of all the similarities of their bundles. In the native -13/6 helical symmetry of individual actin filaments, possible binding sites are not separated by exactly 60°, the optimum angle for hexagonal packing (fig. 4.10(a)). F-actin is therefore not ideally suited for this bundle geometry [67, 90]. To fit the filaments on a hexagonal lattice, ABPs have to twist and locally stretch the F-actin. The difference in angle between the hexagonal symmetry and the actual actin subunit position can provide a first measure for the geometric tension. A comparison of these values for the native -13/6 and the overtwisted -28/13 symmetry is shown in fig. 4.10. Here, the orientation of the hexagonal symmetry is chosen to minimize the maximal deviation. The maximal value as well as the mean deviation per binding site (which would not be affected by a

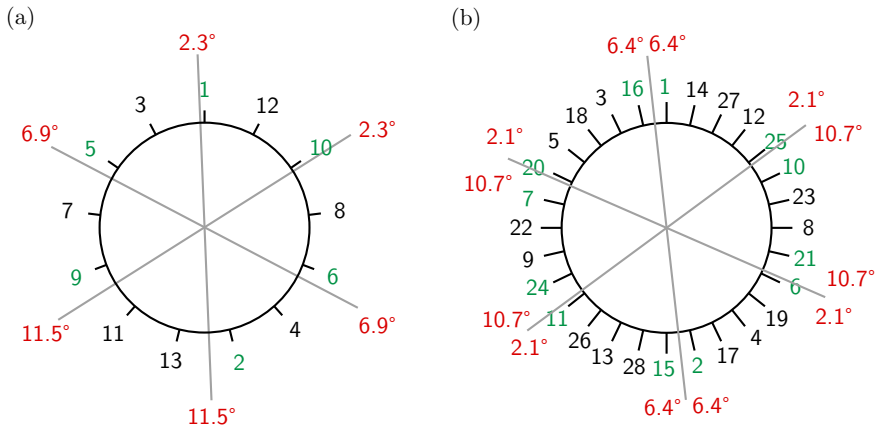

Figure 4.10: Projection of the actin filament in (a) -13/6 and (b) -28/13 symmetry. The grey lines represent the ideal positions for hexagonal packing. The next neighbours and hence the possible binding sites are marked in green. The red numbers indicate the difference in angle between the ideal and actual residue position. The lattice orientation is chosen to minimize the maximal deviation angle.

rotation of the filament relative to the hexagonal lattice) are reduced for the overtwisted -28/13 symmetry:

symmetry	max. deviation	mean deviation
-6/13	11.5°	6.9°
-28/13	10.7°	6.4°

The fully overtwisted state of -28/13 symmetry observed for espin and saturated fascin bundles is still suboptimal for hexagonal packing: a considerable mismatch between the actual and the "ideal" subunit position remains. However, for optimal packing on a hexagonal lattice, the filaments in the bundle would have to twist even more. This is impossible as all ABP binding sites are occupied at the bundle saturation (sec. 4.2). Thus, no additional binding energy can be converted into filament distortion. The suboptimal symmetry of the filaments results in build-up of stress in the bundle and can be considered as the primary reason for the limit on the bundle thickness. The described mechanism provides a molecular explanation for the finite sizes of F-actin bundles in the presence of ABPs or condensing agents that have been observed *in vitro* [66, 91, 92].

Theoretical models Although this simple model based on the estimate energetic contributions gives a basic explanation of the filament overtwist, it does not capture the complex interplay between the optimum geometry required for crosslinking in hexagonally organized bundles and the energetic cost for twisting the actin filaments. It does also not implement the role of the crosslinking protein, which will presumably cause the difference between the bundling mechanism of fascin and espin. A more detailed description by a coarse-grained model of parallel actin bundles is presented in [93, 94]:

The transition from the native state to the fully bundled geometry is discussed on a lattice model, which maximizes the number of perfectly aligned crosslinkers in the bundle, while the required distortion of the intrinsic twist of the filament is minimized. The abrupt and the continuous nature of these transitions for espin and fascin bundles, respectively, are not attributed to differences in linker affinity, but to differences in linker flexibility. While flexible crosslinkers smoothly distort the twist state of the filaments, allowing for intermediate configurations, rigidly crosslinked bundles are characterized by a phase transition. At a critical value of crosslinker concentration, the ABPs induce a highly cooperative switchlike transition from the native to the fully overtwisted geometry in the actin filaments. However, the bundles in this model are essentially unlimited in length and – especially – width. The properties of the modeled crosslinkers allow balancing the mismatch between the helical and the hexagonal symmetry. Therefore, no stress is built up with increasing bundle diameter allowing for bundles of any sizes.

In principle, the mechanical strain involved in bundling chiral polymers might also result in a supertwist of the bundle. Theoretical studies demonstrate that a global twist of chiral filaments around the central bundle axis can lead to thermodynamic frustration of the bundle diameter [95, 96]. Experimentally, this supertwist of the whole bundle has been observed in TEM micrographs for actin/fimbrin bundles and is suggested to limit their bundle thickness [97]. The supercoiling observed for filamin/actin bundle rings in vesicles might be another indication that there are some ABPs which supertwist the whole bundle rather than overtwist the individual filaments [98]. However, the experimental results for the fascin bundles described in this section do not give any indication that fascin-coupled filaments follow such a superhelical path: The SAXS data indicate that the filaments themselves are overtwisted. Moreover, the TEM micrographs show the fascin bundled filaments running in parallel over large distances and appearing straight over hundreds of micrometers.

Conclusion As shown in microscopy experiments, actin/fascin bundles feature a finite bundle thickness of about 20 filaments. The insensitivity of this bundle size on experimental conditions, like the precise preparation method, the salt concentration, or the filament length, indicates that this frustration is rather an equilibrium mechansim than a kinetically trapped state as discussed before [72, 80, 81]. The electrostatic charge accumulation suggested for charged colloidal particles and counterion induced F-actin bundles [72, 82] can not account for the limited bundle thickness in actin/fascin bundles: the separation between F-actin filaments bundled with fascin is approximately 5 nm, much larger than the Debye length at the ionic strength used. In addition, changing the salt conditions does not have any effect on the resulting network or bundle structure.

The SAXS experiments performed in the course of this thesis identify the mismatch between the chirality of the actin filament and the hexagonal symmetry of the bundle packing as a mechanism to tightly control the bundle thickness. The balance between costs of mechanical twisting energy and gains in binding energy can regulate the actin bundle formation and growth. The precise process might depend on the crosslinker properties as its affinity, flexibility and length. While a supertwist of the bundles is observed for fimbrin and indicated for filamin, espin and fascin overtwist the individual

filaments. However, beside all their similarities, fascin and espin seem to take different thermodynamic pathways to the same finale state of overtwisting.

The helical structure of actin filaments is affected by several ABPs [43, 86, 90], suggesting that this conformational variability of F-actin is exploited in many cytoskeletal processes. Thus, it seems that nature utilizes the mismatch between the pitch of individual helical polymers and the optimum value required for hexagonal packing to implement an intrinsic limit to bundle growth corresponding to the above-mentioned observations in microvilli, filopodia, and stereocilia.

4.6 Combination of Different ABPs

In contrast to the observations of the *in vitro* experiments presented above, much bigger bundles consisting of hundreds of filaments are found in several cytoskeletal processes. Interestingly, it has been shown that these thick F-actin bundles are typically linked by more than one ABP species [64]. Each cellular process has a characteristic set of two or more crosslinking proteins: in microvilli, villin and fimbrin are found; in *Drosophila* bristles, fascin and the forked proteins are used, and in stereocilia, fimbrin and espin cooperate in the bundle [1]. Genetic mutations suggest that one crosslinker may be used in early bundle formation to tie the filaments together in small bundles so that they can be subsequently zippered tightly into the precise hexagonal packing by the second ABP [64].

Combining espin and fascin Indeed, the use of multiple ABPs leads also in *in vitro* experiments to larger bundle structures. While TEM micrographs reveal approximately the same maximal bundle thickness for pure espin as observed for fascin, much thicker bundles are formed, if a combination of both ABPs is present (fig. 4.11(a),(b)). In the frame of this thesis, actin/fascin/espin bundles have been analyzed in SAXS experiments investigating the organization of the bundles and the question how a mixture of ABPs overcomes the geometric constraints limiting the bundle size for individual ABPs. Fig. 4.11(c) and (d) show the resulting q_r and q_z intensity patterns: The diffraction patterns for bundles polymerized in the presence of the same concentration of espin and fascin, $R_{\mathrm{e|f}} = R_{\mathrm{espin}} = R_{\mathrm{fascin}}$, show very similar features as the bundles formed by a single crosslinker type. An array of sharp peaks arises for $R_{\mathrm{e|f}} > 0.015$ at approximately the same positions as for espin or fascin (fig. 4.11(c),(d)).

An analysis of the higher-order peak positions in the diffraction pattern along the radial q_r direction confirms hexagonal packing of the filaments. The relative ratios of the peak positions (obtained by Gaussian fits to the background-subtracted data) are in excellent agreement with the theoretically expected values (fig. 4.11(e)). Interestingly, the slope of the relation is in-between the values found for fascin and espin alone. Consequently, the corresponding hexagonal lattice distance $a_{\mathrm{e|f}} = 12.4\,\mathrm{nm}$ is also an intermediate state between $a_{\mathrm{fas}} = 12.2\,\mathrm{nm}$ and $a_{\mathrm{esp}} = 12.6\,\mathrm{nm}$. Although this difference in a is quite small, it can be regarded as reliable. The uncertainty in determining the slope for each crosslinker type is much smaller than the measured difference between fascin, espin and a combination of those. This is shown in the inset of fig. 4.11(e) in

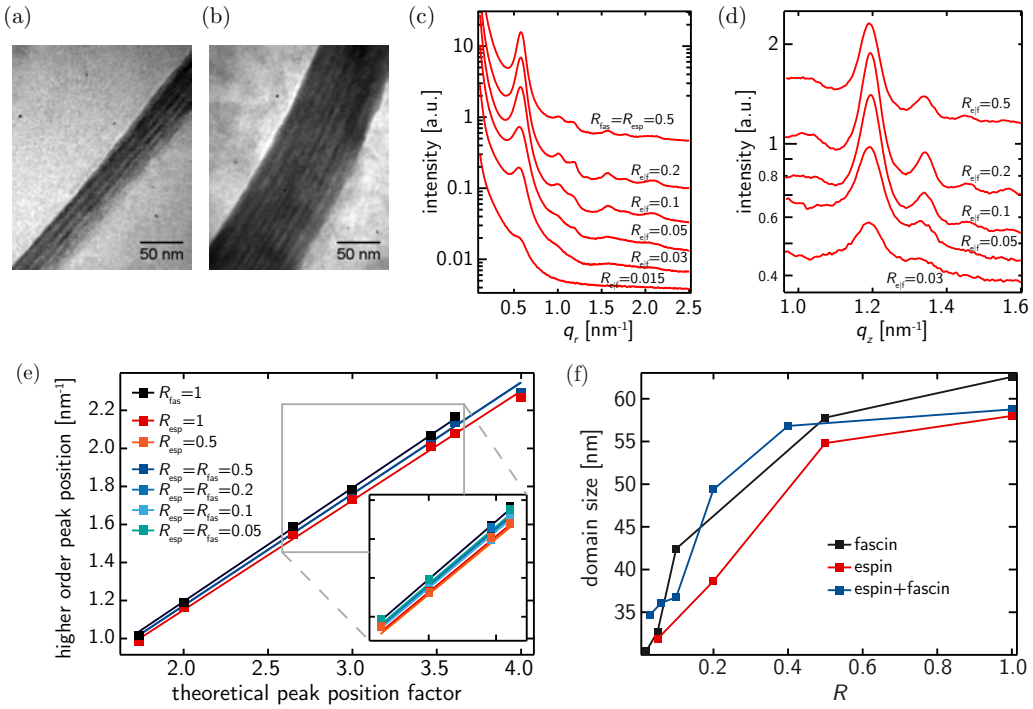

Figure 4.11: Combining fascin and espin: (a)+(b) TEM micrographs of (a) espin ($R_{\mathrm{esp}} = 4$, $c_{\mathrm{A}} = 0.95\,\mathrm{M}$) and (b) espin/fascin bundles ($R_{\mathrm{fas}} = 1$, $R_{\mathrm{esp}} = 4$, $c_{\mathrm{A}} = 0.95\,\mathrm{M}$). While espin alone forms bundles comparable with those formed by fascin, the combination of both leads to formation of much thicker bundles. (c)+(d) Angularly averaged diffraction intensity over wedges along (c) q_r and (d) q_z for various values of $R_{\mathrm{e|f}} = R_{\mathrm{espin}} = R_{\mathrm{fascin}}$. (e) The higher order peak positions reveal hexagonal packing of the filaments. The slope and thus the lattice distance a has an intermediate value between the single-crosslinker bundles. (f) The domain size d in dependence of $R = 2R_{\mathrm{e|f}}$ is the same for the espin/fascin bundle as for espin or fascin exclusively.

which the data for different values of R for one bundle type nicely collapse.

The domain size d extracted from the HWHM of the (1,0)-peak is a measure of the crystallite size convoluted with the substitutional disorder in the lattice. Only if the filaments are perfectly arranged, the domain size d is the same as the bundle thickness. Interestingly, the domain size for the espin/fascin bundles shows the same dependence on $R = 2R_{\mathrm{e|f}}$ as the single-crosslink-bundles, including the absolute values (fig. 4.11(f)). This is in contrast to the large bundle diameter observed in TEM experiments.

The diffraction pattern along q_z reflects information about the intra-filamental symmetry. As can be seen in fig. 4.11(d), the peak position do not change with the crosslinker concentration. Fitting the peaks with the theoretically calculated diffraction patterns of sec. 4.3.3 reveals a overtwisted symmetry of -28/13, the same as found for espin and saturated fascin bundles.

It yet remains unclear how the combination of espin and fascin, which build very similar bundle structures and use the same mechanism to overcome the discrepancy between chirality and hexagonal lattice packing are able to form bundles of larger widths, and how the filaments are arranged in these structures. In principle, one could think either of a cooperative bundling where both crosslinkers are homogeneously incorporated in the bundle or of a mechanism suggested by the *in vivo* experiments where bundles of bundles are formed [64]. The recorded hexagonal lattice distance $a_{\mathrm{e|f}}$ which is in-between the values found for espin and fascin supports the first hypothesis. As fascin and espin form very similar bundles, it seems likely that both can compensate the small difference in a and can cooporate in bundling the actin filaments. In contrast, the discrepancy between the domain size d obtained by SAXS and the bundle width obtained by TEM contradicts the hypothesis of homogenous bundles. It seems unlikely that the combination of both ABPs leads to an increase in substitutional disorder and that this disorder exactly compensates for the enhanced bundle thickness ending up in the same domain size d as the bundle formed by either fascin or espin. This suggests that the maximum crystallite size within the bundle is smaller than the overall bundle width.

A model of espin bundles which are subsequently bundled by fascin (or vice versa) would explain this discrepancy between the observed small domain size and larger bundle width. However, it is not in accordance with the found intermediate value for the lattice distance. Moreover, the comparison of d for the espin/fascin bundles and the bundles formed by only one of those ABPs contradicts this model: only one half of the crosslinker concentration would contribute to the first bundle formation ($R_{\mathrm{esp}} = R_{\mathrm{fas}} = 1/2R$); the curve in fig. 4.11(f) would shift by a factor of 1/2 to the left. The domain size would be significantly larger at comparable R values than for the single-crosslinker systems.

A third conceivable model is that both crosslinkers form bundles separately and these small crystallites are, however, subsequently crosslinked by the mixture of the ABPs. This would accomodate an intermediate lattice distance: the sum of two Gaussians peaks can be interpreted as a single peak at intermediate q_r position. Thereby, the width of the peak is overestimated, and the domain size would reflect too small values.

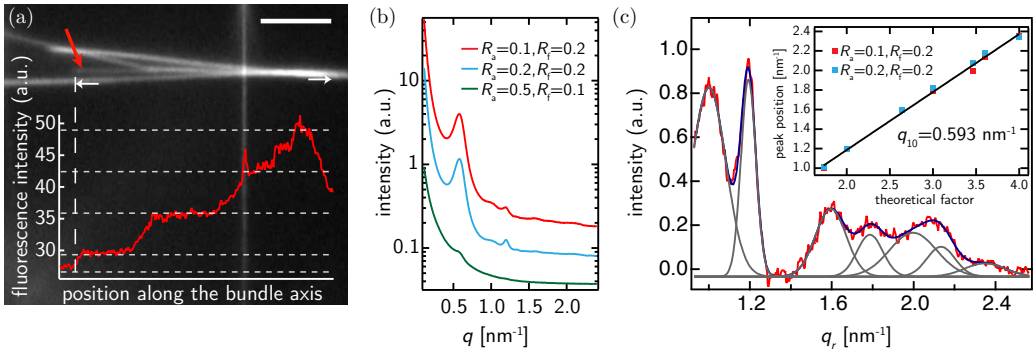

Figure 4.12: Combining α-actinin and fascin: (a) Fluorescence micrographs of α-actinin/fascin bundles. The intensity profile along the bundle indicated with the red arrow shows several steps, indicating that the final bundle consists of approximately seven equally sized bundles. The scale bar indicate 5 µm. (b) The circulary averaged diffraction pattern of α-actinin/fascin bundles for different crosslinker concentrations exhibits fascin-like properties. (c) Gaussian fits to the higher order peaks exhibit the same hexagonal packing as measured for pure fascin networks.

However, this contradicts the measured values for d which are – analogously to the second model – too large.

Obviously, this first series of experiments combining espin and fascin does not elucidate the organization of these bundles. A conceivable complication is the fact that espin and fascin have similar dimensions and form very similar bundle structures. Therefore, an approach using a combination of more different ABPs as filamin or α-actinin might facilitate the investigation of wide bundle formation.

Combining α-actinin and fascin Fluorescence microscopy shows that a replacement of espin by α-actinin leads to the formation of large bundle structures: The micrograph of fig. 4.12(a) shows bundles featuring frayed ends. This indicates that the bundle consists of many smaller bundles (fig. 4.12(a)). The smaller bundles are straight over long-length scales, reflecting their large bending rigidity compared to single-actin filaments. The hypothesis of a hierarchic organization is supported by analyzing the fluorescence intensity along the bundle axis: it increases stepwise indicating that the small bundles are of well-defined size. The corresponding SAXS experiments reveal a fascin-like nature of the bundle organization (fig. 4.12(c),(d)). Dependent on the salt concentrations, α-actinin is reported to form hexagonal or quadratic bundles with a typical lattice distance of $a \approx 40\,\mathrm{nm}$ [99, 100]. In contrast to this, the diffraction pattern of an actin network bundled by a combination of α-actinin and fascin shows the first peak around $q_{10} = 0.59\,\mathrm{nm}^{-1}$ similar to fascin. No indication for any α-actinin characteristics is found. Indeed, fitting the higher order peaks by several Gaussians exhibits $q_{10} = 0.593\,\mathrm{nm}^{-1}$, which is exactly the same value as found for fascin bundles.

The SAXS data combined with the fluorescence micrographs support the assumption that fascin bundles are crosslinked via α-actinin to larger structures. However, the fascin bundling is suppressed when the α-actinin concentration is increased to $R_\mathrm{a} = 0.5$:

In this case α-actinin dominates the network structure. Similar effects are reported for a combination of filamin and fascin by macrorheological measurements [101].

Although the presented data on the combination of different ABPs is insufficent to give insight in the precise organization of such bundles, it shows that it is possible to build also *in vitro* larger structures, even though the bundle size of each crosslinker is limited to smaller values. Different ABPs with different binding affinity, flexibility and length might have different mechanism to overcome the mismatch between the helical symmetry and the bundle packing, e.g. overtwisting single filaments or supertwisting the whole bundle. The limited number of binding sites and the specific interplay between the ABPs will again limit the thickness of these bundles.

Chapter 5

Depolymerization Kinetics of Crosslinked Actin Networks

The requirements on the eukaryotic cytoskeleton are of high complexity and include even conflicting demands: While a dynamic character of cytoskeletal structures is essential for the motility of cells, their ability for morphological reorganizations and cell division, also stability is needed to guarantee the integrity of cells. For the former, the dynamic properties of microtubules [102–105] and actin filaments [106, 107] are of particular importance. The polymerization and depolymerization properties of actin filaments both *in vivo* [107, 108] and *in vitro* [16, 109–115] have been studied extensively.

It is well known that cells make use of actin-binding proteins (ABPs) in order to accelerate the intrinsic dynamics of actin filaments. While nucleation factors like the ARP2/3 complex [116] induce the formation of new filaments, capping proteins and actin-depolymerizing factors like cofilin result in a significant increase of depolymerization dynamics [37, 117]. On the other hand, some crosslinking proteins have been reported to excert a stabilizing effect on individual filaments [118–121]. This seems to be harnessed by cells for the regulation of bundle size *in vivo*: a lack of espin results in inhibition of stereociliary growth, followed by progressive degeneration of the hair bundle [122]. Moreover, varying expression levels of fascin in *drosophila* bristle cells resulted in changes of filament turnover accounting for distinct phenotypes [123]. An overexpression of α-actinin has been shown to cause accumulation of actin filaments and inhibition of actin dynamics [124].

As such a stabilization of filamentous structures could be an important aspect for cells, it is crucial that filaments are protected against depolymerization factors such as cofilin, which is omnipresent in a cell. Yet, it is still necessary to enable a controlled depolymerization of bundles and filaments, which suggests that additional mechanisms are needed to enable a disintegration of these actin structures. Despite the importance of the regulation of actin dynamics for many cytoskeletal processes, quantitative investigations of their mediation by crosslinking molecules remain scarce.

The following chapter provides a quantitative analysis of the effect of ABPs on the depolymerization kinetics of actin networks. Section 5.1 describes the methods used for analyzing the time course of depolymerization. The results presented in section 5.2 demonstrate that crosslinking proteins suppress actin depolymerization in a concentration dependent manner. Pyrene and microscopy experiments show a distinct slow-

down in depolymerization induced by latrunculin or dilution of the actin filaments (sec. 5.2.1-5.2.3). Moreover, ABPs even protect actin filaments from disintegration by cofilin (sec. 5.2.4). However, the addition of molecular motors can overcome the stabilization effect: even extremely stable actin bundle structures can be disintegrated by the concerted action of cofilin and myosin II (sec. 5.2.5). The results are discussed and qualitatively explained by a simple but generic model in section 5.3.

5.1 Methods

The choice of experimental methods to analyze the depolymerization behavior of different actin networks is quite challenging: The aim has been to investigate the dynamics of completely different structures of actin networks, made up of different crosslinking proteins in varying concentration. The corresponding geometries range from an entangled actin solution without any crosslinkers and a homogeneously crosslinked network of single filaments (e.g. for HMM) to thick, kinetically trapped bundles in the case of filamin (see section 2.2). In order to assure the comparability of the results, it is desirable to have one method applicable to all network structures. Besides the challenge of capturing single-filament and bundle networks at the same time, the out-of-equilibrium nature and the internal prestress of filamin and α-actinin bundles makes the handling very difficult. Experimental caution is mandatory to avoid the collapse of such networks.

Depolymerization can be induced in several ways: The depolymerization factor latrunculin B (LatB) sequesters monomeric actin and thus reduces the effective monomer concentration in the solution. Its addition causes a depolymerization at both, barbed and pointed ends of the filaments. Similarly, dilution of the actin below the critical concentration $c_{\mathrm{crit}} \gtrsim 0.1\,\mu\mathrm{M}$ [16] will induce depolymerization. While these methods cause depolymerization simply by lowering the monomer concentration in the solution without changing the rate constants of the filament, different effects can be expected for the addition of cofilin. Cofilin has not only been reported to cause an increase of depolymerization rates [35], but also to sever actin filaments [38, 125] (section 2.2).

There are different methods to follow the degree of polymerization over time: The first straight-forward approach is fluorescence microscopy. In order to evaluate the micrographs at different time steps, quantitative image analysis can be applied (sec. 5.1.1). Another standard technique to investigate the time course of polymerization or depolymerization is the pyrene assay. It provides a quantitative measure of the amount of polymerized actin in the sample (sec. 5.1.2). A detailed description of these methods and the diffusion chamber which allows the addition of reagents to a polymerized network (sec. 5.1.3) is given below.

Unfortunately, the widely pull-down assay does not seem effective for bundled networks. Centrifuging[1] a polymerized network should pellet all protein aggregates and thus all filamentous actin with bound crosslinking protein. In case of entangled actin solutions, only monomeric actin stays in the supernatant. This makes the centrifugation assay an adequate method to measure the critical actin concentration c_{crit}. For

[1] centrifugation was performed for 1.5 h at 100 000 g and 435 400 g, respectively

crosslinked networks, the actin concentration in the supernatant is greater than for pure actin solutions (see appendix B for details). In the case of filamin bundles, this supernatant can polymerize after the centrifugation step into a homogenous bundle network indicating that the increase in monomer concentration cannot be explained by a change of association/dissociation rates and thus of the critical concentration by the crosslinking molecules.

Sample preparation All samples in this section were polymerized at an actin concentration of $c_A = 3\,\mu M$ in F-buffer. In the case of crosslinked networks, the actin is usually polymerized in the presence of the crosslinking molecules. For actin/rigor-HMM networks, F-buffer without ATP is used. For the actin/filamin networks polymerized in the presence of myosin II, a different 10x polymerization buffer (100 mM Imidazol, 30 mM $MgCl_2$, 2 mM $CaCl_2$, 0.05 % NaN_3, pH 7.2) is used.

5.1.1 Fluorescence Microscopy and Quantitative Image Analysis

For microscopy experiments, the individual monomers were labeled with a fluorescent dye (sec. 2.3). If LatB and cofilin depolymerization assays are applied to filamentous networks, a 1 % fraction of labeled reporter filaments is mixed with unlabeled F-actin after full polymerization. This is necessary as at a concentration of 3 µM labeled actin, individual actin filaments are hardly detectable.

Fluorescence microscopy data are acquired on a Zeiss Axiovert 200M inverted microscope, using a 100x oil immersion objective with a numerical aperture of 1.4. For of α-actinin networks, a 40x oil immersion objective (NA 1.3), and, for filamin bundle networks, a 25x oil immersion objective (NA 0.8) is used. Time lap videos were taken for each time step in order to allow for a distinction between filaments and bundles. To correct for the insufficiency of Köhler illumination in the fluorescence path way, the inhomogeneous illumination is corrected by a gliding square average filter.

In order to measure the amount of polymerized actin over time, the fluorescence micrographs recorded at individual time steps are analyzed quantitatively. The images are edited to allow for the identification of filamentous structures (fig. 5.1). The first steps of this image processing are a gaussian blur and a background subtraction using the algorithms implemented in ImageJ. In order to identify the filamentous structures, a threshold which is adjusted manually for each time step is used to create a binary image. A minimal cluster size for filamentous structures suppresses diffuse fluctuations of the background intensity.

For filamentous networks the number of pixels which are part of filaments is counted and averaged over at minimum 30 images for each time step. For bundle networks, the fluorescence intensities of the bundle structures determined by the described binarization are measured to account for bundle thickness. Again, it is averaged over at least 30 images. The time courses of depolymerization are normalized by the initial values.

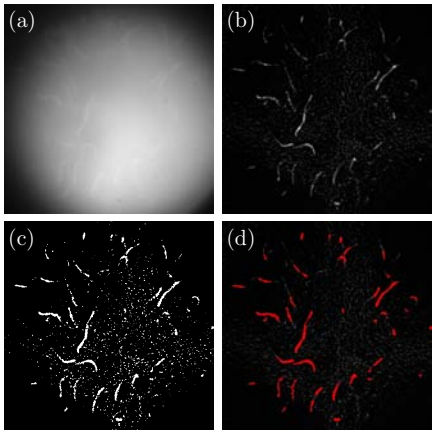

Figure 5.1: Image processing for quantitative image analysis using the example of an entangled actin solution: The series shows the same image after different processing steps using ImageJ and Matlab: (a) Original fluorescent micrograph. (b) Gaussian blur and background subtraction. (c) Binary image by applying a threshold in ImageJ. (d) A minimal cluster size defines the filamentous structures shown in red.

5.1.2 Pyrene Assay

The fluorescence of pyrene-labeled actin is drastically enhanced after polymerization. Thus, the fluorescence signal is proportional to the polymer weight concentration. Consequently, the pyrene assay has been established as a powerful tool for polymerization/depolymerization studies [41]. Note that the signal is insensitive to the polymer length distribution; the assay can only capture the overall amount of polymers in the sample.

For pyrene assay experiments, a total actin concentration $c_\mathrm{A} = 3\,\mu\mathrm{M}$ and a degree of labeling of about 11% are used. The fluorescence intensity is determined by a spectrofluorometer of type FP-6500[2]. Upon full polymerization, 50 µM LatB is added and thoroughly mixed using a pipette. The normalized fluorescence intensity $I_\mathrm{n}(t) = \frac{I(t)-I_0}{I_1-I_0}$ is calculated, where I_0 is the fluorescence intensity prior to polymerization and I_1 is the fluorescence intensity directly after addition of LatB.

This assay is not applicable for out-of-equilibrium networks. The method is based on the assumption that the addition of a depolymerization reagent neither changes the network morphology nor the filament length distribution. This is not the case for actin/filamin and actin/α-actinin networks where pipetting the sample will destroy the network architecture.

5.1.3 Diffusion Chamber

In order to investigate the depolymerization kinetics of crosslinked actin networks, the ability to add a reagent after the full polymerisation of the network is essential. Due to the high non-equilibrium nature of filamin and α-actinin networks, simply pipetting will mechanically disrupt the network and irreversibly change the network morphology [26]. This is overcome in a setup where the reagent can slowly diffuse into the sample. Such, mechanical damage to the network is avoided.

Therefore, a diffusion chamber has been designed (fig. 5.2), in which the actin network polymerizes between a cover slip and a 0.1 µm pore size Durapore PVDF filter

[2]JASCO Labor- und Datentechnik GmbH, Groß-Umstadt, Germany

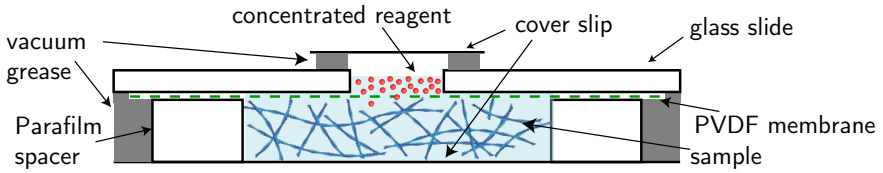

Figure 5.2: Schematic representation of the diffusion chamber used in depolymerization experiments which allows for addition of depolymerization reagent after polymerization of the network via the PVDF membrane.

membrane[3]. Four layers of Parafilm are used as a spacer and a glass slide with a hole is used to fix the membrane. In order to prevent the sample from evaporation over the extended experimental period of several days, the chamber is sealed with a sufficient amount of vacuum grease. An additional cover slip is used to close the chamber at the top. Upon polymerization, a highly concentrated solution of the reagent (LatB, cofilin or ATP) is added on top of the membrane.

5.2 Results

There are indications in literature that some ABPs influence the depolymerization kinetics of actin filaments. Often a specific effect of the crosslinking molecules has been assumed. However, a more general investigation relying on a quantitative analysis of the effects of different crosslinking molecules has been missing.

In the following section, such a study of various ABPs, namely fascin, filamin, α-actinin, rigor heavy meromyosin (HMM) and tropomyosin is investigated. Different techniques of depolymerization and quantitative analysis are used. At the same time, it addresses the question, how the network geometry influences the dynamics, i.e. whether bundling is necessary for a slow-down in depolymerization dynamics.

5.2.1 Latrunculin Induced Depolymerization in Pyrene Assays

In a first series of experiments, depolymerization is induced by addition of latrunculin B (LatB). This causes depolymerization at both the barbed and the pointed end by an effective decrease of available actin monomers in the solution. A standard pyrene assay, in which the normalized fluorescence intensity $I(t)$ is a measure for the degree of polymerization, allows monitoring the time course of actin depolymerization (sec. 5.1.2). In case of an entangled actin solution, the intensity and thus the amount of polymerized actin continuously decreases within 20 hours after the addition of LatB to $\sim 20\,\%$ of the initial value (fig. 5.3(a)). It has been suggested that the depolymerization kinetics for such a pure actin solution follow a double exponential decay [109, 113]. Assuming a constant depolymerization rate, the curve shape reflects the filament length distribution in the sample.

Interestingly, the depolymerization kinetics are drastically modified in the presence of the ABP fascin, which bundles actin into individual polar bundles (sec. 2.2). As de-

[3]Sigma-Aldrich Corporation, St. Louis , USA

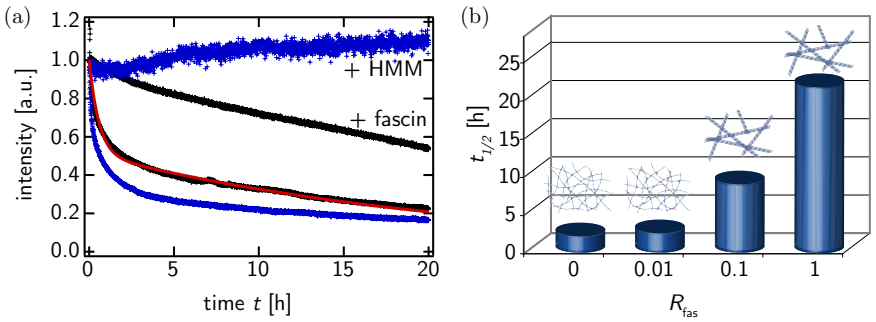

Figure 5.3: Pyrene assay monitoring actin depolymerization induced by addition of LatB: (a) Crosslinking molecules slow down the depolymerization of actin filaments. Fluorescence intensity upon addition of 50 µM LatB is shown for actin/fascin ($R = 1$) (black) and actin/rigor-HMM networks ($R = 1$) (blue) as well as the pure actin solutions in the corresponding buffers (F-buffer with ATP (black) and F-buffer without ATP (blue)). The depolymerization of an entangled actin solution is fitted with a double exponential decay (red). Please note, that the enhanced noise in case of HMM is due to quenching effects by the binding of HMM and the normalization with respect to the initial value. (b): The inhibition of actin depolymerization by fascin is concentration dependent. For actin/fascin networks $t_{1/2}$ is shown as a function of the molar ratio of fascin to actin, R. The network architectures emerging at the respective fascin concentrations are illustrated.

picted in fig. 5.3(b), fascin is slowing down the depolymerization process in dependence of its concentration: At a molar ratio of $R_{\text{fas}} = c_{\text{fas}}/c_{\text{a}} = 0.01$ fascin and actin no effect is resolvable. In contrast, the time $t_{1/2}$ at which the normalized fluorescence is halved, $I(t_{1/2}) = \frac{1}{2}I(0)$, increases about a factor of ten for $R_{\text{fas}} = 1$.

In order to test whether bundling accounts for this stabilization, the effect of the ideal crosslinker HMM in the rigor state is investigated . Rigor-HMM can both form crosslinks between actin filaments and decorate individual filaments (sec. 2.2). As shown in fig. 5.3(a), rigor-HMM completely inhibits actin depolymerization at $R_{\text{HMM}} = 1$, even though it does not cause any bundling at all.

5.2.2 Latrunculin Induced Depolymerization in Microscopy Based Experiments

A pyrene assay is inadequate in case of some ABPs as it is sensitive to quenching effects and as it requires pipetting the polymerized solution. This is problematic for networks – such as actin/filamin bundle networks – which are kinetically trapped and show syneresis effects [26]. Using a diffusion chamber allows the addition LatB to all actin network without disrupting the network mechanically (sec. 5.1.3). Fluorescence microscopy experiments confirm the effect of 50 µM LatB on the network architecture. Entangled actin solutions depolymerize almost completely within 48 hours (fig. 5.4(a)). Quantitative image analysis (sec. 5.1.1) allows monitoring the degree of depolymerization over time (fig. 5.4(c)).

Comparison ofthe time courses of depolymerization in the pyrene assay and the quantitative image analysis demonstrates, that the time scale observed in the microscopy

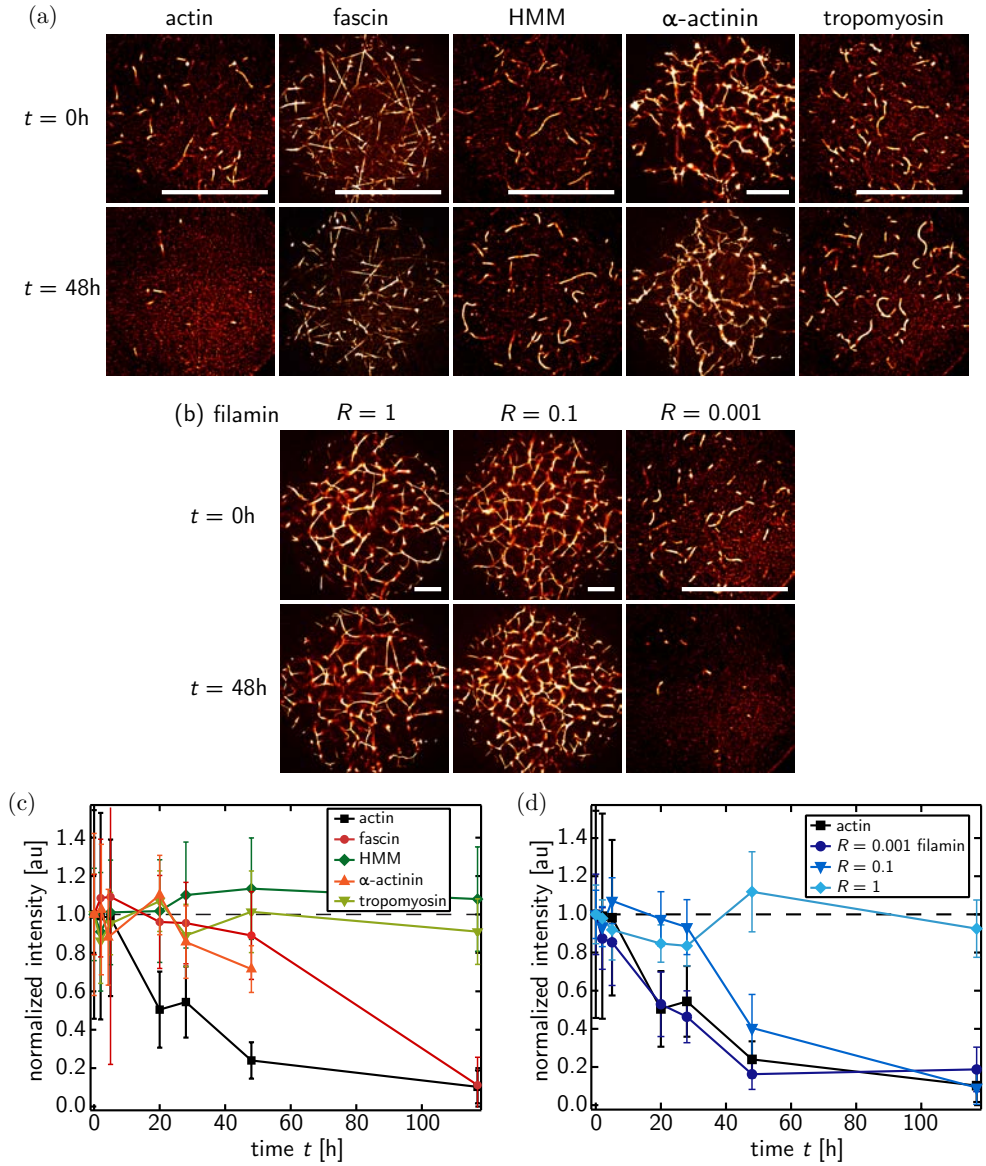

Figure 5.4: Fluorescence micrographs with quantitative image analysis showing the effective inhibition of depolymerization: actin networks ($c_a = 3\,\mu M$) in the presence of various crosslinkers are shown before and 48 hours after the initiation of depolymerization by the addition of 50 µM LatB via a diffusion chamber. In the case of filamentous networks, only 1 % of the actin is fluorescently labeled.(a) At $R = 1$, all crosslinking proteins effectively inhibit depolymerization. As shown for filamin in (b), the slowdown of actin depolymerization is concentration dependent. Scale bars denote 50 µm. (c)+(d) Quantitative image analysis allows extracting time courses of depolymerization corresponding to (a) and (b), respectively. (c) It can be seen that all crosslinking proteins observed in this assay slow down the depolymerization at $R = 1$ compared to entangled actin solutions. (d) The slowdown caused by filamin is concentration dependent. While no effect is observed at $R_{fil} = 0.001$ compared to pure actin (squares), the depolymerization clearly is slowed down at $R_{fil} = 0.1$ and is completely inhibited at $R_{fil} = 1$.

experiments is of the same order of magnitude as the slow time scale observed in the pyrene experiment. An initial fast decay is visible in the pyrene assay, but not in the analysis based on fluorescence microscopy. This difference could be due to changes in association/dissociation rates induced by the covalently labeling of the actin monomers with the pyrene or alexa dye (sec. 2.3). However, performing the microscopy experiment with the fraction of pyrene labeled actin used in the fluorimeter does not influence the depolymerization kinetics; this follows the same time course of the standard alexa-experiment. Likewise, the alexa labeling does not seem to have an influence: If unlabeled actin is mixed with LatB and fluorescently labeled phalloidin is added at certain time steps after initiation of depolymerization, the quantitative image analysis roughly follows the alexa-experiment.

The difference in the time courses can be explained by the fact that filaments shorter than a certain cut-off length, which is given by the resolution limit and the minimal cluster size in image processing, do not contribute to the decay measured in fluorescence microscopy. In contrast, the pyrene assay is sensitive to all lengths of filaments. If the fraction of filaments shorter than the cut-off length is large enough, this will cause such a difference in the time course of both experiments (see appendix C).

However, addition of crosslinking proteins to the sample drastically changes the depolymerization kinetics. While the pure actin filaments almost completely vanish within 48 h, only partial depolymerization is observed for actin/fascin networks at $R = 1$, where even bundles are still present after 48 hours (fig. 5.4(a) and (c)). In the case of actin networks crosslinked by rigor-HMM at $R = 1$, no depolymerization is observable over a time duration of 117 hours. Although fascin and rigor-HMM arrange actin filaments in significantly different network architectures, both crosslinking proteins suppress the depolymerization of actin filaments quite effectively. This suggests that the stabilization is a generic effect. Indeed, also the ABPs filamin and α-actinin, which induce the formation of highly curved and branched actin bundle networks, inhibit actin depolymerization (fig. 5.4). Similarly to actin networks crosslinked with rigor-HMM, actin/filamin networks of $R = 1$ are completely stable over 117 hours. In the case of filamin, where a pyrene assay cannot be used, this diffusion assay even allows the observation of a concentration dependency similar to that observed for fascin before. Again, an increase of the crosslinker concentration results in a gradual slowdown of the depolymerization dynamics. The stabilizing effect is not restricted to crosslinking ABPs: tropomyosin, which binds to six actin subunits along one filament has been shown to inhibit depolymerization at the pointed end of Villin-capped actin filaments [126]. As shown in fig. 5.4(a) and (c), tropomyosin even prevents depolymerization of uncapped filaments. An altered length distribution of filaments can not account for the drastic effects observed.

5.2.3 Dilution Induced Depolymerization

Diluting actin solutions below the critical concentration c_{crit} provides an additional way to induce depolymerization. This might give a deeper insight into the principle underlying the stabilization effect of crosslinking proteins. Upon 300-fold dilution in

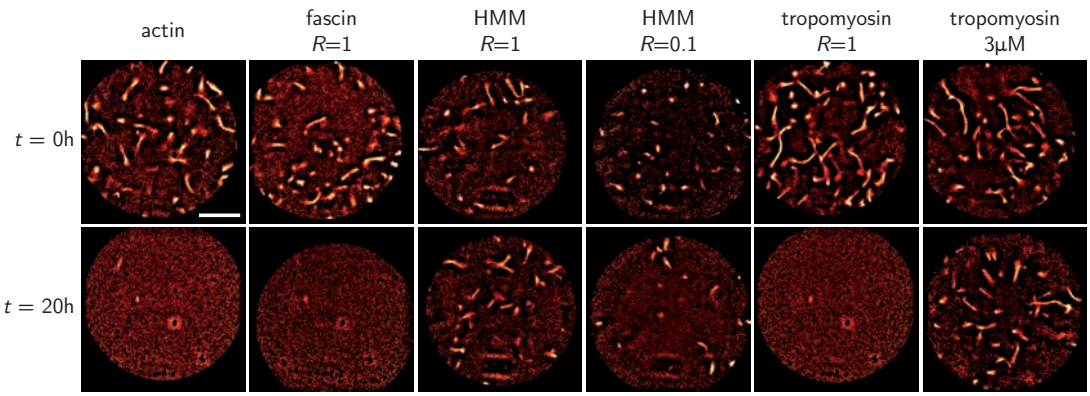

Figure 5.5: Depolymerization induced by dilution: Actin networks (polymerized at $c_a = 3\,\mu M$) in the presence of various crosslinking proteins are shown directly and 20 hours after 300-fold dilution to $c_a = 0.01\,\mu M$ in F-buffer. While pure actin solutions and actin/fascin bundle networks almost completely depolymerize, no depolymerization is observable within 20 hours for actin networks crosslinked by rigor-HMM. Tropomyosin decorated filaments depolymerize but the stabilizing effect can be recovered by addition of 3 µM tropomyosin to the dilution buffer. Scale bar is the same for all images and denotes 20 µm.

F-buffer, actin solutions ($c_a = 3\,\mu M$) almost completely depolymerize within 20 hours (fig. 5.5). Actin/fascin bundles decompose within a few minutes upon dilution, followed by a complete depolymerization within the experimental period comparable to pure actin solutions. Rigor-HMM at $R_{HMM} = 0.1$ or $R_{HMM} = 1$ inhibits depolymerization on relevant timescales. While rigor-HMM suppresses depolymerization without bundling filaments, bundling is essential for a slowdown of depolymerization induced by fascin. Both, fascin and rigor-HMM, form inter-filamental crosslinks but only rigor-HMM can form a high number of intra-filamental crosslinks decorating single filaments. This suggests that in the case of rigor-HMM rather intra-filamental crosslinks than the comparable small number of inter-filamental crosslinks account for the observed stabilization of actin filaments. 300-fold dilution of tropomyosin decorated filaments results in depolymerization (fig. 5.5). However, this might result from the fact that due to its lower binding affinity dilution causes a decrease of the molar ratio of bound tropomyosin. While fascin bundles still decompose if 3 µM fascin is added to the dilution buffer, the stabilizing effect of tropomyosin can be indeed recovered by adding 3 µM tropomyosin to the dilution buffer. This again demonstrates the concentration dependency of the stabilizing effect of ABPs.

5.2.4 Cofilin Induced Depolymerization

The mechanism by which crosslinking proteins affect the depolymerization kinetics of actin filaments is similar for both depolymerization methods independently if this is induced by addition of LatB or by dilution in F-buffer. Different effects can be expected for the addition of cofilin, which has not only been reported to cause an increase of depolymerization rates [35], but also to sever actin filaments [38, 125]. Tropomyosin has been shown to be a physiological inhibitor of cofilin dependent actin dynamics [127].

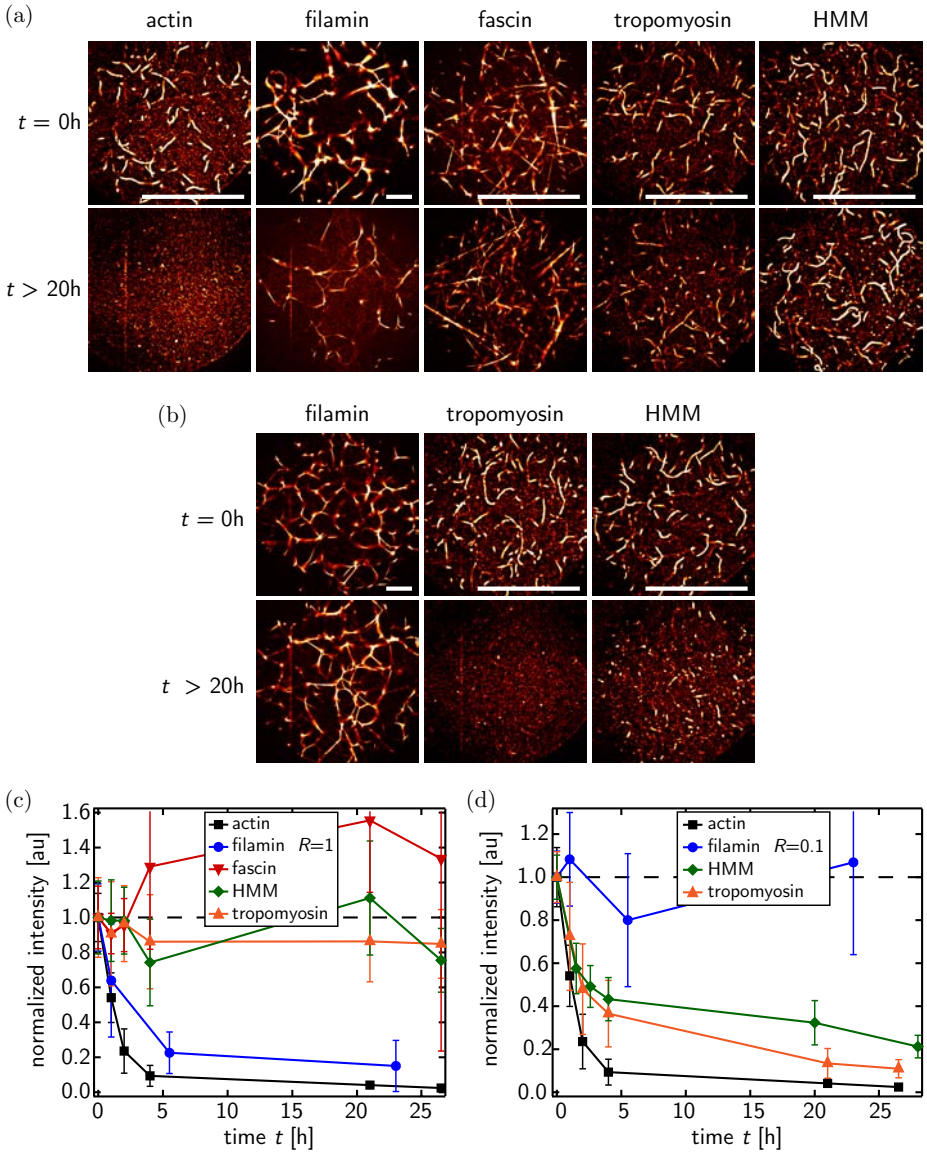

Figure 5.6: Crosslinking molecules inhibit depolymerization induced by cofilin: Actin networks ($c_a = 3\,\mu M$; for filamentous networks, only 1 % of the actin filaments is labeled) in the presence of various ABPs are shown directly and ≈ 20 hours after addition of 3 µM cofilin. (a) While pure actin solutions completely depolymerize within 2 hours (inset), depolymerization is drastically slowed down for actin networks crosslinked by rigor-HMM, decorated by tropomyosin or bundled by fascin or filamin ($R = 1$). (b) At lower crosslinker concentrations ($R = 0.1$), the slowdown of depolymerization is less pronounced than at high concentrations in the case of rigor-HMM and tropomyosin. Only for filamin, the stabilizing effect is even stronger at $R = 0.1$. Scale bars denote 50 µm. (c)+(d) Quantitative image analysis allows extracting time courses of depolymerization induced by cofilin from fluorescence micrographs shown in (a) and (b), respectively. (c) All observed ABPs decelerate the depolymerization at $R = 1$ compared to pure actin. While depolymerization is still observed for filamin, no significant depolymerization can be detected for HMM, fascin and tropomyosin. (d): At $R = 0.1$, a slow depolymerization is observed for HMM and tropomyosin. No depolymerization is observed for actin/filamin networks.

As shown in fig. 5.6, not only tropomyosin but also all the crosslinking molecules tested here prevent disintegration of actin networks by cofilin, provided that they are present at high concentrations ($R = 1$). In the case of tropomyosin, HMM and fascin, no depolymerization is detected in the quantitative image analysis (fig. 5.6(c)). Although bundles are still visible after more than 20 hours (fig. 5.6(a)), a slow disintegration is observed for actin/filamin bundle networks at $R = 1$ (fig. 5.6(c)). In the case of α-actinin networks, no reproducible could be obtained.

Addition of 3 µM cofilin to an actin network crosslinked by rigor-HMM or decorated by tropomyosin at lower concentrations ($R = 0.1$) results in disintegration (fig. 5.6(b)) – however still significantly slower than for pure actin (fig. 5.6(d)). Suprisingly, actin/filamin bundle networks at $R_{\text{fil}} = 0.1$ are completely stable over 23 hours. The complete stabilization at the low concentration of $R_{\text{fil}} = 0.1$ might be explained by an interaction of several actin subunits with a single filamin molecule. The fact that a slow disintegration is observed at the higher crosslinker value $R_{\text{fil}} = 1$ might indicate a specific effect that cannot be explained by our simple model presented in sec. 5.3.

5.2.5 Active Disintegration of Actin Bundles by Molecular Motors

The insensitivity of actin bundle networks with respect to the depolymerization assays investigated so far suggests that cells need additional mechanisms to disintegrate such highly stabilized actin structures. Molecular motors are known to influence the decomposition of bundles associated with the filopodium *in vivo* [128] and to disintegrate actin bundles *in vitro* [129, 130].

Using a standard motility assay [131], HMM molecules are able to disrupt fascin bundles. The ABP fascin arranges actin filaments into polar bundles which are transported by the motor molecules. Due to this polarity the bundles can slide as fast as single actin filaments on the myosin II surface (fig. 5.7(a)). Dependent on various parameters like the ATP, fascin or motor concentration, the bundles disintegrate during this movement. There are different modes of disintegration where also a combination of them can appear: at high ATP and low fascin concentrations, the bundle unzips right after ATP addition. The diverging filaments have the same length as the original bundle (fig. 5.7(b)). Without ATP and, thus, without activity of the motor molecules, the bundles are stable over minutes on the surface indicating that not only a dissociation of fascin molecules is responsible for the disintegration process. If fascin is present in the supernatant buffer, the bundles are more stable. Only short pieces of actin filaments smaller than 5 µm are pulled out. This process can take up to a few minutes until the whole bundle is disrupted (fig. 5.7(c)). Increasing the amount of inactive motor molecules presents a third mechanism: While sliding on the surface, the bundle repeatedly stalls, buckles, and finally breaks (fig. 5.7(d)). The underlying mechanism responsible for the different modes of disintegration is still unknown and subject of current research.

Based on the described disintegration ability of HMM in the two-dimensional setup it seems reasonable to assume that molecular motors might help to disrupt even three-dimensional actin networks bundled by filamin. To test this hypothesis, an actin/filamin network ($c_{\text{a}} = 3\,\mu\text{M}$, $R_{\text{fil}} = 1$) is polymerized in the presence of full-

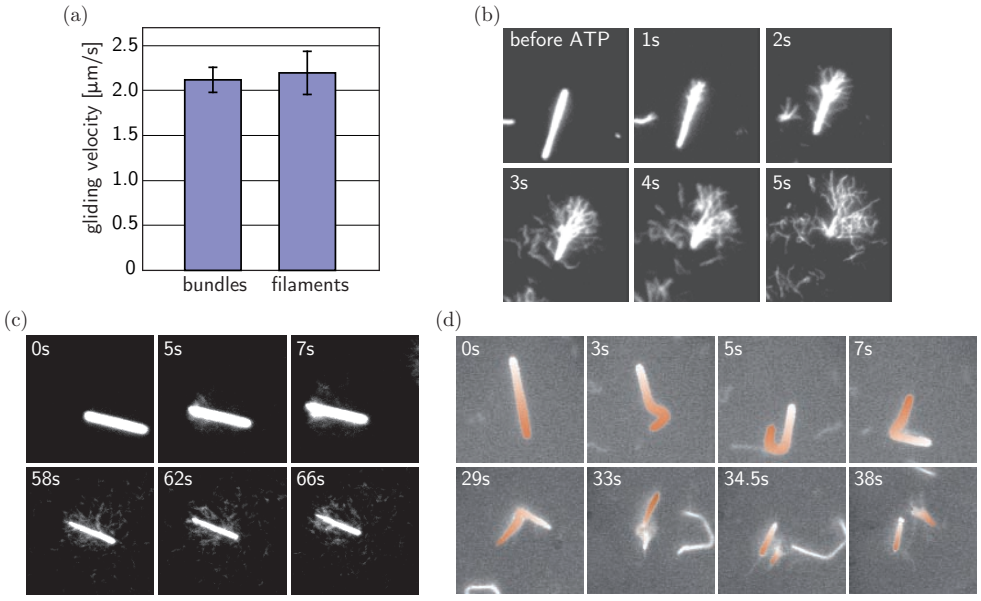

Figure 5.7: Motility assay with actin/fascin bundles: (a) Due to the polarity of the fascin bundles, their gliding velocity is the same as for single filaments. The data was recorded at $c_{\mathrm{ATP}} \approx 50\,\mu\mathrm{M}$ and $R = 1$. (b)-(d) Depending on various parameters, different modes of disintegration are observed: (b) Within a few seconds after ATP addition, the fascin bundles unzip completely. (c) If fascin is present in the buffer, only short fragments of actin filaments are pulled out. (d) Increasing the amount of inactive motors, the bundles repeatedly stall, buckle, and finally break. The color gradient from the leading edge (pointed end, in brown) to the rear part (barbed end, in white) indicates the direction of movement.

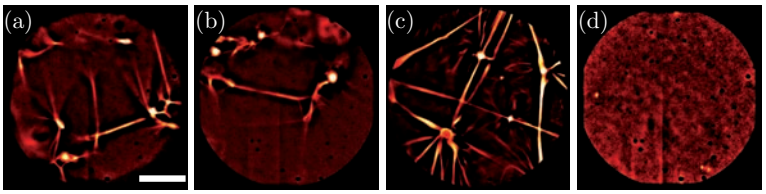

Figure 5.8: Actin/filamin bundle networks can be disintegrated using molecular motors: (a) Actin/filamin networks ($c_a = 3\,\mu M$, $R = 1$) are polymerized in the presence of myosin II ($c_{myosin} = 0.035\,\mu M$), which has been saturated with with a 16-fold excess of AMP-PNP and is therefore unable to bind to actin. (b) Addition of 3 µM cofilin does not result in complete depolymerization within 20 hours. (c) Activation of myosin II by addition of 5.4 mM ATP causes drastic structural reorganization but actin structures are still present after 20 hours. (d) By addition of both, cofilin and ATP, the networks can be completely disintegrated (d). Scale bar is the same for all images and denotes 20 µm.

length myosin II ($c_{myosin} = 0.035\,\mu M$) which forms – dependent on the salt concentration – mini-filaments (sec. 2.2). The myosin has been saturated with a 16-fold excess of the non-hydrolyzable ATP analog AMP-PNP and is therefore not able to bind actin (fig. 5.8). Active myosin during polymerization would cause drastic changes in the network morphology. As expected, 20 hours after addition of 3 µM cofilin bundles are still present (fig. 5.8(b)). Also activation of the molecular motors by addition of 5.4 µM ATP in the absence of cofilin causes only a drastic reorganization (fig. 5.8(c)), but no disintegration of the actin structures. Only if both agents are added simultaneously, the network is completely disintegrated within 20 hours (fig. 5.8(d)). Thus, cofilin and the presence of motor activity is needed to depolymerize actin/filamin bundle networks effectively.

5.3 Discussion

The effect of crosslinking proteins on the depolymerization behavior of F-actin has been rather unknown. Although an inhibition of actin depolymerization has been reported previously for *dictyostelium* 30 kDa actin-bundling protein [118], α-actinin [119], espin [120] and plastin [121] and has been postulated for bundles from *in vivo* experiments [122, 123], it has so far not been systematically investigated. The multiple depolymerization assays used in this work should reveal insights into the effect of crosslinking molecules on the kinetics of actin filaments: Depolymerization has been induced by dilution or by addition of latrunculin B and followed by quantitative fluorescence microscopy as well as a pyrene actin assay. Different crosslinking proteins result in the formation of actin networks with strongly varying network architectures and properties [8]. Yet, all studied crosslinking molecules inhibit depolymerization of F-actin provided that they form a high number of crosslinks. This can be achieved either in the case of bundling, where inter-filamental crosslinks are formed (fig. 5.9(a)), or if ABPs decorate actin filaments with intra-filamental crosslinks (fig. 5.9(b)). The latter is the mechanism by which the well studied toxin phalloidin stabilizes F-actin [109, 132]. Both cases result in an increase of the total binding energy of the crosslinked actin subunits in the

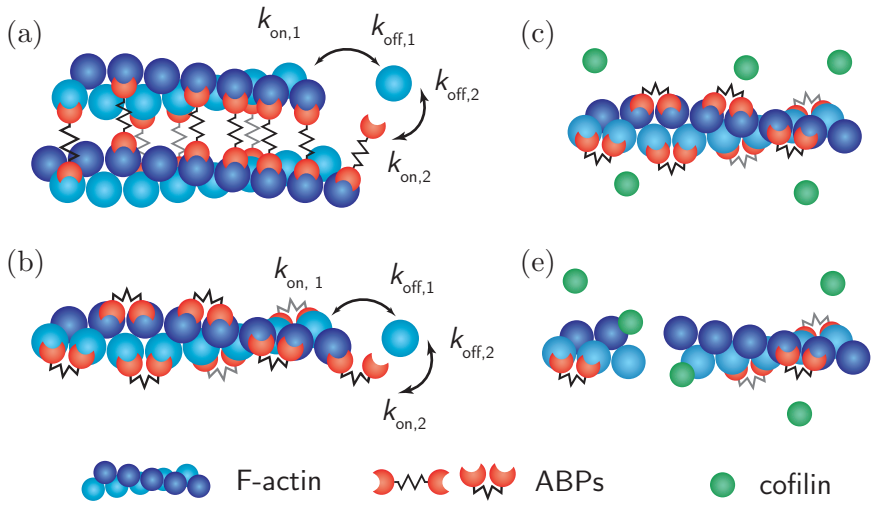

Figure 5.9: Simple model for depolymerization of actin in the presence of crosslinking molecules. (a): Crosslinking molecules which bundle actin filaments prevent potential depolymerization events. (b): A similar effect occurs if crosslinking molecules decorate an individual actin filament. (c): At high concentrations crosslinking molecules can prevent disintegration of actin filaments induced by cofilin. (d): At lower crosslinker concentrations disintegration induced by cofilin is possible.

filament – which is set by the actin-actin as well as the actin-ABP interaction – due to the additional bonds to the crosslinking molecules. As solely simultaneous unbinding of the actin-actin as well as the actin-crosslinker bond allows for a complete depolymerization event, depolymerization is shifted to slower timescales. Moreover, a concentration dependence of the slowdown is reasonable: At low molar ratios of the crosslinker, such an improbable depolymerization event may be followed by several actin subunits which can freely depolymerize until the next crosslinking molecule is reached.

This simple model (fig. 5.9) captures the major effects of crosslinking proteins, but does not account for their specific properties, such as the binding propensity to actin. The fact that no specific effects are needed to rationalize a stabilization effect of crosslinking proteins suggests that a similar behavior can be expected also for other dynamic polymers. In order to test this hypothesis, the depolymerization of microtubules upon dilution is investigated.[4] In analogy to rigor-HMM in the case of actin, kinesins in the rigor state can be used to decorate microtubules with intra-filamental crosslinks. Indeed, an obvious slowdown of the depolymerization process upon dilution is observed in the presence of kinesins (fig. 5.10).

Crosslinking proteins not only inhibit the intrinsic dynamics of actin filaments but all crosslinking proteins tested here also inhibit disintegration of actin filaments by cofilin. Presumably, the crosslinking proteins sterically hinder the access of cofilin to the actin filament (fig. 5.9(c)), inside bundles this access is additionally hampered. As expected from our model, disintegration induced by cofilin is possible at lower crosslinker concentrations (fig. 5.9(d)). Such an interpretation agrees with the previous

[4]Microtubules and kinesin is kindly provided by M. Brunnbauer.

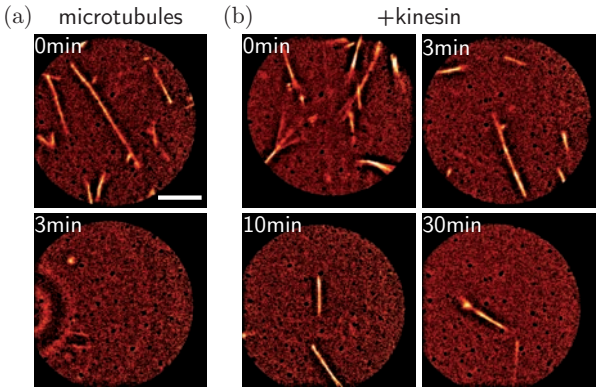

Figure 5.10: Depolymerization of microtubules induced by dilution is slowed down by kinesin: Microtubules ($\approx 100\,\mu M$) are shown directly after 100-fold dilution. Within 3 minutes, a complete depolymerization is observed. If the microtubules have been decorated with kinesin (KIF5A) in the rigor state previous to dilution, some microtubules are still present even after 30 minutes. Scale bar is the same for all images and denotes 20 µm.

findings that bundling by villin1 [133] or nonspecific interactions [134] can prevent depolymerization induced by cofilin. In addition, actin bundles induced by dynamin2 and cortactin are remodeled to a more loosely packed conformation if GTP is added, which in turn causes a higher sensitivity to cofilin [135]. The considerable effect of filamin at intermediate concentration can be attributed to the supposition that filamin acts with several subunits along the actin filaments.

The drastic modification of actin kinetics by crosslinking molecules can be expected to have wide-ranging implications for living cells, where crosslinking proteins or ABPs such as tropomyosin, which bind at least two actin subunits simultaneously are omnipresent. Crosslinking ABPs may not only guarantee a mechanical stability and integrity of cytoskeletal actin structures but can also provide a powerful tool for cells to stabilize distinct actin structures against the intrinsic actin dynamics and can therefore fulfill regulatory functions. On the other hand, additional concepts which enable cells to disintegrate crosslinked actin structures or facilitate a continuous turn-over of actin filaments are indispensable. In addition to severing ABPs such as cofilin – which accomplishes a disintegration of moderately crosslinked networks but is not able to destroy most networks crosslinked with a one-to-one stoichiometry – cells may need to deal with the crosslinker induced stabilization of actin filaments using active molecular motors [128–130]. As shown above the combination of active myosin II and cofilin is able to completely disintegrate actin/filamin networks at the high crosslinking concentration $R = 1$. Myosin II activity might partially disrupt actin/filamin bundles by tearing them apart and thereby create free binding sites along the filaments or at the ends of the filaments, where cofilin can have access to. While this study demonstrates that crosslinkers drastically alter the actin dynamics, it is a formidable challenge to address their role on the actin kinetics *in vivo*, where multiple molecules are involved and compete for their effect on the filaments. Future studies on the interplay between the numerous cytoskeletal constituents will eventually enable the reconstitution of *in vitro* modules with controlled properties akin to those of the highly dynamic and complex living cell.

Chapter 6

Nonlinear Rheology of Entangled Actin Solutions

Many processes of living cells require a tight control of cytoskeletal mechanics. While the puzzling complexity of the linear response and the observed general response behaviors are already posing a major challenge to experiments and theory alike [8], it has been proposed that cells harness the nonlinear response of the semiflexible polymer networks to rapidly adapt their local properties already at small strains [7]. As the strain increases, a crossover has been observed to a linear inelastic flow regime, most likely due to crosslink slippage [136]. The observed generic form of the nonlinear response of living cells can be explained by bending deformations of the cytoskeletal network [137], however only *in vitro* systems will be able to unambiguously determine the underlying physical mechanisms.

The simplest model system with still daunting complexity are entangled F-actin solutions. While the linear response can be quantitatively understood by tube deformations [76, 138], an understanding of the nonlinear response is still elusive. This is partly attributable to the fact that all kinds of stress weakening or stiffening responses have been reported for such networks [139, 140]. The contradictory results need to be addressed, before further progress can be achieved or any conclusions can be drawn on the deformation modes dominating such networks. Achieving consistent results requires that several difficulties are overcome, including clean sample preparation and the development of experimental techniques that can accurately characterize nonlinear deformation. Reproducible measurements of nonlinear deformation are often difficult to obtain because nonlinearity is associated with large deformations that alter or yield material structures. A major challenge is to separate the elastic, viscous and plastic stress contributions for soft samples with pronounced viscous properties. Thus, great care has to be taken in choosing a measurement protocol to obtain a method-independent description of the nonlinear response [140].

The first section in this chapter includes a short abstract of the theory of polymer physics and the phenomenological description of viscoelasticity. Furthermore it presents a variety of macrorheological measuring techniques in the nonlinear regime. In section 6.2, these protocols are used to characterize the nonlinear shear response of highly purified *in vitro* F-actin solutions. By careful analysis of the rheological data, it is possible to resolve all contradictions found literature so far. As shown in section 6.3 this nonlinear response of entangled F-actin is very sensitive to experimental conditions including temperature, actin and salt concentration, and even filament length.

It is shown that each of these parameters can be tuned to produce a dramatic transition between softening and hardening of the network. These results are discussed in the context of the existing literature and are qualitatively explained by the recently introduced glassy worm like chain model [141] in section 6.4.

6.1 Rheological Basics

If a body is subjected to an external force, the body can either be moved as a whole or it can be deformed by moving various particles of the body with respect to each other. Elastic materials strain instantaneously according to Hooke's Law – independent of the applied strain rate. In contrast, for viscous liquids the stress is always directly proportional to the rate of strain in accordance to Newton's Law – independent of the strain itself. Viscoelastic materials have elements of both of these limiting cases. The study of the deformation and flow of matter is called rheology, while the experimental characterization of the viscoelastic properties of a material is known as rheometry.

This chapter provides a short introduction to the theory of polymer networks, including a brief description of the tube model and of the basic concepts of linear viscoelasticity. Section 6.1.3 describes the macrorheological methods for measuring the viscoelastic properties of polymer solutions. Experimental protocols how to analyze the mechanical properties in the nonlinear regime and their interpretation are introduced in section 6.1.4.

6.1.1 Theory of Polymer Networks

Many biological polymers are semiflexible, i.e. their shape and behavior is not only dominated by entropic effects but else by internal energetic contributions that arise from their flexural rigidity κ. A measure for the competition between internal bending and entropy is the persistence length $l_\mathrm{p} = \kappa/k_\mathrm{B}T$. It defines the typical length scale over which directional correlations along the polymer are lost. Actin filaments have a persistence length of 18 µm and (*in vitro*) a typical contour length of several micrometers [142, 143], making them textbook representatives of the class of semiflexible polymers.

Worm-Like-Chain Model A theoretical description of semiflexible polymers has to incorporate bending rigidity as well as the conformational entropy of the strand. This is done by the common *worm-like chain model* (WLC) first introduced in [144]. This model describes the polymer as a continuous space curve $\mathbf{r}(s) = (\mathbf{r}_\perp(s), s - r_\parallel(s))$ where $\mathbf{r}(s)$ and $r_\parallel(s)$ denote the transverse and longitudinal displacements at arclength s. The WLC model has been subject to extensive studies; for more details about the WLC dynamics, the reader may be referred to [145]. Longitudinal fluctuations are of higher order. Thus, the dynamics of a weakly bending WLC can be described in leading order by the linear Langevin equation:

$$\zeta_\perp \partial_t \mathbf{r}_\perp = -\kappa \mathbf{r}_\perp'''' + f\mathbf{r}_\perp'' + \boldsymbol{\xi}_\perp \tag{6.1}$$

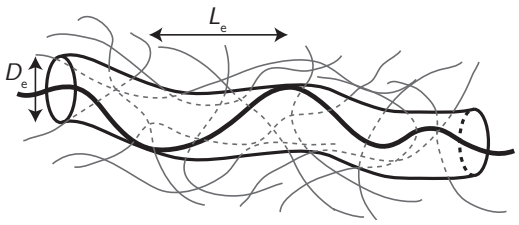

Figure 6.1: Tube model by Doi and Edwards [146]: The effect of the surrounding polymers is modeled by a hypothetical tube wherein the polymer of interest can fluctuate. The tube is characterized by the tube diameter D_e and the entanglement length L_e.

where $\zeta_\perp$ and $\boldsymbol{\xi}_\perp$ denote the solvent friction per length and the Gaussian thermal noise, respectively. Equation (6.1) can be solved by introducing eigenmodes. The eigenfunctions can be chosen to be simple sine functions.

$$\mathbf{r}_\perp(s,t) = \sum_{n=1}^{\infty} \mathbf{a}_n(t) W_n(s) \tag{6.2}$$

$$W_n(s) = \sqrt{\frac{2}{L}} \sin(k_n s) \tag{6.3}$$

Independent from each other, these eigenmodes relax exponentially with a characteristic relaxation time τ_n for each mode,

$$\tau_n = \frac{\tau_L}{n^4 + n^2 f/f_L}, \tag{6.4}$$

where $\tau_L = \zeta L^4/\kappa\pi^4$ is the relaxation time and $f_L = \kappa\pi^2/L^2$ is the Euler force of the longest mode. Based on these results, various time-dependent parameters can be calculated, for instance the transverse mean-square displacement or the relaxation after application of an external forces [145].

Tube Model The WLC model presented above describes the dynamics of an isolated fibre. If the concentration of polymers in the solution exceeds a critical value, the movement of a chain is highly constrained by the entanglements with the surrounding polymers. The fibers can slide past each other but cannot cross the adjacent fibers. Caused by the enormous number in degrees of freedom, such a solution of semiflexible polymers is extremely complex if all polymers are considered explicitly. An important step is the simplification to a single-polymer description. The tube model of Doi and Edwards [146] has proven to be a very useful tool in combination with the reptation model of de Gennes [147]. Here, the topological constraints of the entangled polymer solution are modeled assuming that the motion of an individual chain is confined in a tube-like region formed by the surrounding polymers (fig. 6.1). Inside this tube, the filament can freely fluctuate and is able to move laterally along the tube axis. The entanglement length L_e is defined as the mean distance between collisions of the polymer with its tube. Transversal undulations of the filament with wavelengths larger than the entanglement length are highly overdamped. The tube will change either by reptation of the central fibre along the tube or by fluctuations of the surrounding polymers. External forces lead to an affine deformation of the tube [148].

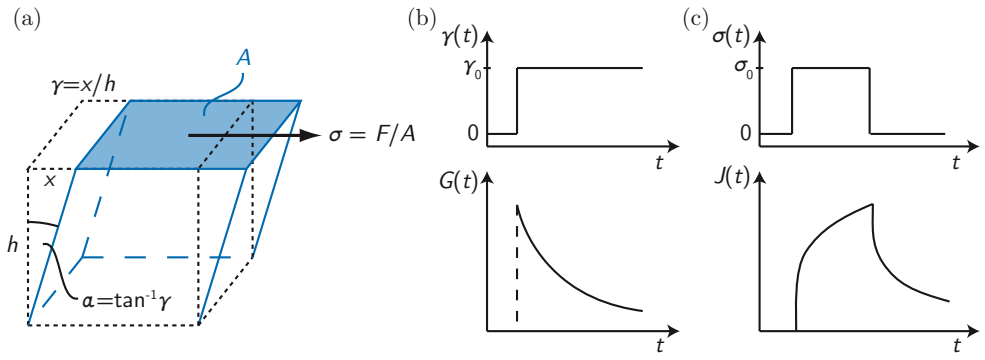

Figure 6.2: (a) Scheme of the geometry in a simple shear experiment. The stress σ is defined as the applied force normalized by the area F/A, the strain γ as the ration between deflection and sample height x/h. (b) Time profiles in a stress relaxation experiment following a sudden step deformation. (c) Time profiles in a creep experiment following a sudden stress step.

Although originally proposed for flexible polymers, the tube model is perfectly applicable to semiflexible polymers. Beyond the qualitative benefits, also quantitative predictions for the plateau modulus or the tube diameter have been achieved [138, 149].

6.1.2 Basic Concepts in Linear Viscoelasticity

In general, solutions of semiflexible polymers exhibit viscoelastic behavior. In this case, the relation between stress σ, strain γ, and their time dependencies can be described by a constitutive equation. In a typical rheometric experiment, the deformation – a dimensionless quantity which is defined as the ratio between deflection and sample height – is uniform and corresponds to a simple shear of the sample (cf. fig. 6.2(a)). In this case, the constitutive equation is based on the Boltzmann Superposition principle: It states that – in the linear regime – the stress response to successive changes in strain are additive which is called the Boltzmann Superposition principle:

$$\sigma(t) = \int_{-\infty}^{t} G(t-t')\frac{\partial\gamma(t')}{\partial t'}\mathrm{d}t' \tag{6.5}$$

A detailed description can be found in [150]. In an alternative constitutive equation, the strain is expressed as a function of the changes in stress:

$$\gamma(t) = \int_{-\infty}^{t} J(t-t')\frac{\partial\sigma(t')}{\partial t'}\mathrm{d}t' \tag{6.6}$$

Beside this mathematical definition, a demonstrative, physical meaning is attached to the memory functions $G(t-t')$ and $J(t-t')$, which manifests in their terms of relaxation modulus and of creep compliance, respectively: Consider a step deformation where the strain is suddenly increased to $\gamma = \gamma_0$ (fig. 6.2(b)). According to equation (6.5), the time dependence of the stress is given by

$$\sigma(t) = \gamma_0 G(t) \tag{6.7}$$

Thus, the relaxation modulus $G(t)$ describes the time course of the stress $\sigma(t)$, normalized by the applied strain γ_0 after a stepwise deformation. A typical viscoelastic profile is shown in fig. 6.2(b). Note that in the case of an elastic material (where $G(t) = \text{const.}$) equation (6.7) reduces to Hooke's Law.

Analogously, a constant shear stress σ_0 may be applied to the sample in a so-called creep experiment (fig. 6.2(c)). The dependence of the deformation on time, $\gamma(t)$, can be derived from equation (6.6):

$$\gamma(t) = \sigma_0 J(t) \tag{6.8}$$

Thus, the physical meaning of the creep compliance $J(t)$ is the time course of the creeping strain $\gamma(t)$, normalized by the applied stress σ_0 in a step-stressing experiment. It has dimensions of a reciprocal modulus. In the limit of an elastic material, $J = 1/G$.

Complementary information is provided by an oscillatory shear experiment in which a sinusoidal strain $\gamma_0 \sin(\omega t)$ at constant frequency $f = \omega/2\pi$ is applied to the sample. If the material behaves linearly, the stress response will also change sinusoidally. In general, there is a phase shift δ between strain and stress response, ranging from 0° to 90°.

$$\sigma(t) = \sigma_0 \sin(\omega t + \delta) = \sigma_0(\cos\delta \sin(\omega t) + \sin\delta \cos(\omega t)) \tag{6.9}$$

Placing the sinusoidal strain in the constitutive equation (6.6) yields:

$$\begin{aligned}\sigma(t) &= \gamma_0 \left(\omega \int_0^\infty G(s)\sin(\omega s)\mathrm{d}s\right)\sin(\omega t) + \gamma_0 \left(\omega \int_0^\infty G(s)\cos(\omega s)\mathrm{d}s\right)\cos(\omega t) \\ &= \gamma_0 \left(G'(\omega)\sin(\omega t) + G''(\omega)\cos(\omega t)\right) \\ &= \gamma_0 G^*\end{aligned} \tag{6.10}$$

Comparison of equations (6.9) and (6.10) shows that

$$G'(\omega) = \sigma_0/\gamma_0 \cos\delta \tag{6.11}$$

$$G''(\omega) = \sigma_0/\gamma_0 \sin\delta \tag{6.12}$$

Equation (6.10) demonstrates that the stress response is composed of two contributions: an in-phase part proportional to G' and an out-of-phase part proportional to G''. Thus, $G'(\omega)$ describes the elastic contribution is called *storage modulus*; in contrast, $G''(\omega)$ is a measure for the viscous contribution and is called *loss modulus*. Generally, the moduli G' and G'' depend on the applied frequency ω.

In principle, the transient and oscillatory measures $G(t)$ and $G(\omega)$ report the same viscoelastic properties. They are connected via a Laplace-Transformation:

$$G^*(\omega) = \int_0^\infty G(t)\mathrm{e}^{-i\omega t}\mathrm{d}t \tag{6.13}$$

Therefore, a conversion of the time in the frequency space is possible but experimentally hardly to realize.

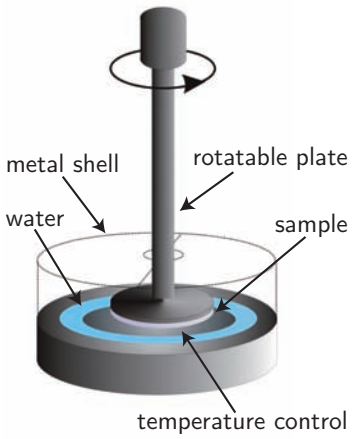

Figure 6.3: Scheme of the measuring setup in macrorheology. The sample is loaded between a temperature controlled plate at the bottom and a rotatable plate-plate geometry. Water surrounding the sample and the metallic shell prevents evaporation.

6.1.3 Methods in Macrorheology

In this work, the viscoelastic properties of actin networks are determined using macrorheological methods. For this purpose, all dimensions of the measuring setup have to exceed the length-scales of the network to ensure the measurement of the macroscopic character of the sample rather than of the local properties of single constituents. The measurements have been done on two commercial, stress-controlled rheometers. For most experiments, the Physica MCR301[1] has been used. The LAOS measurements have been performed at the AR-G2[2] which allows recording the oscillation raw data via a small auxiliary program. The setup of both rheometers is very similar (fig 6.3): The sample is loaded between a stationary, temperature controlled plate at the bottom and a rotatable plate above. In case of the Physica MCR301, a plate-plate geometry with a diameter of 50 mm and a plate separation of 160 µm has been used; at the AR-G2, the plate-plate geometry has a diameter of 40 mm and the gap has been chosen to 300 µm to obtain approximately the same sample volume of 450 µl. To avoid evaporation, water is added in a reservoir surrounding the sample and the measuring unit is covered with a metallic shell.

After instrument calibration, the actin solution is added within a few minutes after the initiation of polymerization. To ensure complete polymerization, the complex modulus is monitored by stress-controlled oscillations at a frequency $f = 0.5\,\mathrm{Hz}$ and a torque $M = 0.5\,\mu\mathrm{Nm}$, which is near the minimal torque both rheometers can apply. The quality of the actin was tested by measuring the frequency spectrum of the moduli $G'(f)$ and $G''(f)$ in the linear regime.

For some methods, it is necessary to monitor not only the complex modulus $G^*(f)$ that is provided by the rheometer software but to track also the values of stress $\sigma(t)$ and strain $\gamma(t)$ during the oscillations. A small auxiliary program at the AR-G2 provides raw data of angular displacement and torque with a resolution of 1 ms. These values are converted to strain γ and stress σ_M by multiplication with the standard geometric

[1] Anton Paar, Graz, Austria
[2] TA Instruments, New Castle, USA

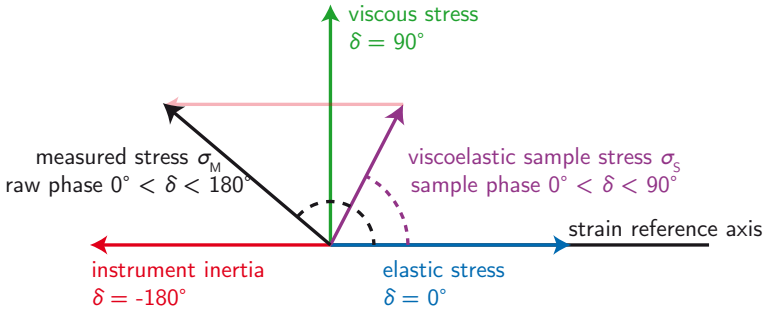

Figure 6.4: Schematic of the phase relations in a single head rheometer. Pure elastic stress is in phase with the applied strain, pure viscous stress is shifted by 90°. The measured stress is the sum of the viscoelastic sample stress and the inertia contribution of the instrument which is shifted by 180°.

conversion factors for parallel-plates rheometers, C_γ and C_σ, respectively. To obtain the stress acting on the sample σ_S the applied stress, σ_M, has to be corrected for the instrument inertia I according to $\sigma_S = \sigma_M - a\ddot{\gamma}$, where $a = IC_\sigma/C_\gamma$ (fig. 6.4). The second derivative of the strain,$\ddot{\gamma}$, was calculated by a numerical differentiation of the shear rate $\dot{\gamma}(t)$, that was first smoothed using a cubic spline method available in MATLAB. Note that this inertial contribution $a\ddot{\gamma}$ depends on ω^2 and is responsible for the upper frequency limit of the experimentally accessible range. Above a critical frequency, the signal is dominated by the inertial contribution and it is no longer possible to separate the inertia correction.

The accuracy of this sample stress calculation has been demonstrated to milli-second timescale by measuring the expected Newtonian response with calibration oils. It has also been verified that the rheometers strain-control feedback loop is sufficiently accurate to produce roughly sinusoidal strain and strain rate waveforms, even in the nonlinear regime, as expected for strain-controlled oscillations. This has been achieved in the "medium motor mode" of the rheometer control software.

6.1.4 Experimental Methods for Analyzing the Nonlinear Regime

The most challenging task in investigating the nonlinear regime of soft materials is the choice of an appropriate experimental protocol. The difficulty is to distinguish between the different stress contributions, namely elastic, viscous, and plastic contributions. Purely or predominantly elastic networks are independent of the applied loading rates. Thus, their nonlinear response can be successfully probed by various techniques. For more viscous networks or for entangled solutions, the viscous flow cannot be neglected. In this case, the network response strongly depends on both the loading rate and the detailed measurement protocol. Even more complications occur if the network yields and is irreversibly deformed. In the following, a short overview of the used methods and their limitations is given.

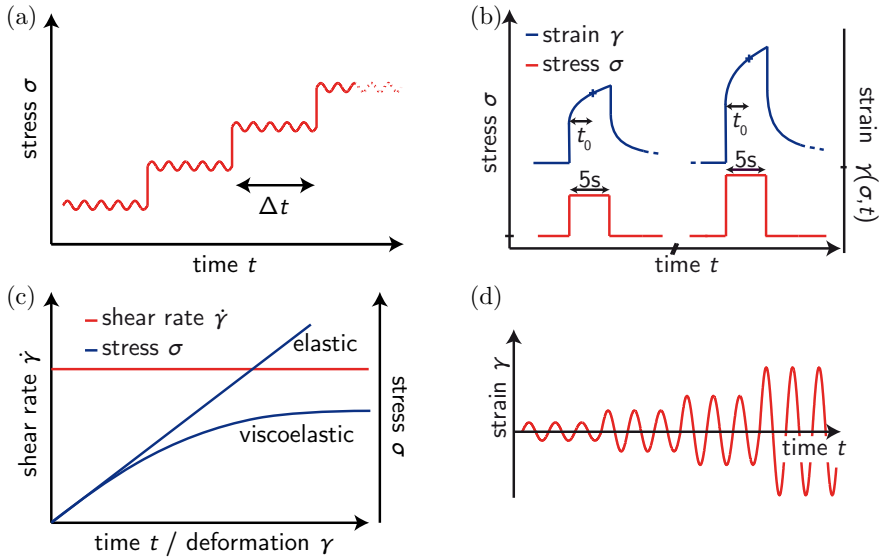

Figure 6.5: Scheme of the different measuring protocols in the nonlinear regime: (a) Prestress (b) Stress Pulse Series (c) Constant Shear Rate (d) LAOS.

Prestress

A common method for the investigation of the nonlinear regime in viscoelastic samples is the prestress protocol. To measure the dependence of the viscoelastic parameters on an external force, increasing amounts of a constant prestress σ_0 are applied, each for a time period Δt. The network parameters are determined by a small superimposed oscillatory stress (fig. 6.5(a)).

This method is applicable only for highly crosslinked samples with a marginal viscous contribution. Artifacts occur if viscous flow is introduced and the sample rearranges during the time Δt, changing the network geometry during the measurement. Hence, the time dependence is in this method hardly accessible: the mechanical response is not only dependent on the applied frequency, but is also dominated by the duration Δt of the applied prestress and by the overall measuring time.

Stress Pulse Series

The step stressing protocol avoids the deficiency of the prestress method: A series of short increasing stress pulses is applied to the sample, and the deformation is recorded over time (fig. 6.5(b)). The time in-between two pulses is chosen to be that long that the network relaxes to at most 2 % of the deformation of the foregoing stress pulls, but at least 50 s to ensure that all relaxations have decayed. A measure for the viscoelastic properties is the creep compliance $J = \gamma/\sigma_0$ (section 6.1.2) in dependence of the applied stress evaluated at a certain delay time t_0. The inverse of the creep compliance, 1/J, is considered as a modulus of the network. As a modulus of the network, the inverse of the creep compliance $1/J$ is considered. Due to the long relaxation times after pulses

with larger amplitude, the procedure can take up to several hours, which calls for a good protection from evaporation.

Constant Shear Rate

A complementary, strain controlled measuring method is a simple shear experiment in which a constant shear rate $\dot{\gamma}$ is applied to the sample. The differential modulus $K(\gamma)$ is determined by numerically differentiating the stress-strain-relation $\sigma(\gamma)$, which has firstly been smoothed by the Smoothing Spline algorithm of IGOR. Alteration of the shear rate provides the opportunity to investigate the time dependence of the response.

In a purely elastic sample, the stress would increase linearly with the strain according to Hooke's Law (fig. 6.5(c)). The response of an ideal viscoelastic sample converges at short times to the elastic limit before viscous contributions become significant. Thus, this apparent weakening cannot be interpreted as strain weakening. Only if the stress-strain-relation steepens above the elastic limit, evidence for a strain hardening is given.

LAOS, Fourier Transform Rheology and Lissajous Figures

If a material behaves nonlinearly, the response in an oscillatory shear experiment is no longer sinusoidal. This nonlinearity appears usually above a critical oscillation amplitude depending on the frequency. The LAOS (Large Amplitude Oscillating Shear) measurements investigate this behavior in dependence of the strain amplitude γ_0 (fig. 6.5(d)). Oscillations in the nonlinear regime will produce higher harmonic contributions in the stress response. Thus, the storage and loss modulus, G' and G'' respectively (section 6.1.2), are no longer well defined. Information about the sample parameters can be obtained by the shape of the non-sinusoidal response. Therefore, the raw data of the oscillations has to be collected and processed to obtain the sample stress and strain. These are not provided by default by the software of commercial rheometers (section 6.1.3).

Fourier Transform Rheology (FTR) One method to analyze the inertia-corrected raw data, and thus to evaluate the nonlinearity in the LAOS experiments, is the Fourier analysis of the response. It allows the quantification of the degree of nonlinearity by means of the intensity ratios of higher harmonics in the response function [151]. If a simple sinusoidal strain is applied, the response can be written as a Fourier series

$$\sigma(t) = \gamma_0 \sum_{n,\text{odd}} G'_n(\omega, \gamma_0) \sin(n\omega t) + G''_n(\omega, \gamma_0) \cos(n\omega t) \tag{6.14}$$

Based on non-negativity of stored energy it has been argued that – in the case of the simple shear deformation – only odd terms contribute to the stress response [152]. The dissipated energy per unit volume during one period of sinusoidal strain is given by:

$$
\begin{aligned}
E_d &= \int_0^{2\pi/\omega} \sigma(t)\dot{\gamma}(t)\mathrm{d}t \\
&= \gamma_0^2\omega \int_0^{2\pi/\omega} \sum_{n,\mathrm{odd}} \left(G_n'(\omega,\gamma_0)\sin(n\omega t) + G_n''(\omega,\gamma_0)\cos(n\omega t)\right)\cos(\omega t)\mathrm{d}t \\
&= \pi\gamma_0^2 G_1''(\omega,\gamma_0) \qquad (6.15)
\end{aligned}
$$

where all other summands in the Fourier series vanish due to the orthogonality of the trigonometric functions. The result is the same as for a linear viscoelastic material, where $G_1''(\omega,\gamma_0)$ is replaced by $G''(\omega)$. Thus, G_1'' governs the dissipated energy during sinusoidal deformation. All other harmonic moduli in equation (6.14) govern the reversible storage of energy [153].

A Fourier transformation of the response signal yields a frequency spectrum which features the first harmonic at the excitation frequency $\omega/2\pi$ and the higher harmonics at the odd multiples. A measure for the nonlinearity is the intensity ratio of the higher harmonics to the first [151].

Although it is difficult to understand the physical meaning of the harmonic moduli, the Fourier transform rheology provides a sensitive technique to detect nonlinearities in the sample and to separate between elastic and viscous contributions. Crucial for the delicate detection is a reduced signal-to-noise-ratio and an increased spectral resolution $\Delta\nu = 1/t_{\mathrm{ac}}$. Both can be achieved by a longer acquisition time t_{ac} [151]. Therefore, typically 5-50 cycles of the excitation wave are acquired. At large amplitudes, this can lead to plastic softening of the sample as in the case of entangled actin solutions (section 6.2).

Quantitative Analysis of Lissajous Curves A more demonstrative way of analyzing the LAOS data is plotting it in the form of a Lissajous curve. This is a parametric plot of the stress $\sigma(t)$ versus the strain $\gamma(t)$. In the limit of an ideal elastic sample following Hooke's law, this is a straight line with a slope equal to the spring constant (fig. 6.6(a)); in the limit of a purely viscous sample, the Lissajous curve is an ellipse with the axes along the coordinate axes (fig. 6.6(b)). For a viscoelastic material, the curve appears as a tilted ellipse (fig. 6.6(c)). The enclosed area in the Lissajous plot is equal to the energy dissipated per unit volume during one cycle and thus a measure for G'', as calculated above.

Nonlinearity in the sample response will distort the ellipse. Thus, the Lissajous figures clearly depict deviations from the linear viscoelastic behavior. Distorted Lissajous curves can take many different forms: In fig. 6.6(a), typical shapes of strain-stiffening and strain-weakening of a purely elastic material are shown. Analogously, fig. 6.6(b) depicts curves of nonlinear fluids in the shear-thicking and shear-thinning regime. In the viscoelastic regime, where a combination of these effects can occur, a large variety of Lissajous curves exists. Fig. 6.6(d) and (e) exemplarily show a scheme in the strain-stiffening and strain-weakening regime, respectively.

Beyond the purely graphic description, a framework of different moduli has been proposed to analyze the Lissajous curves in a more quantitative manner [154]. As

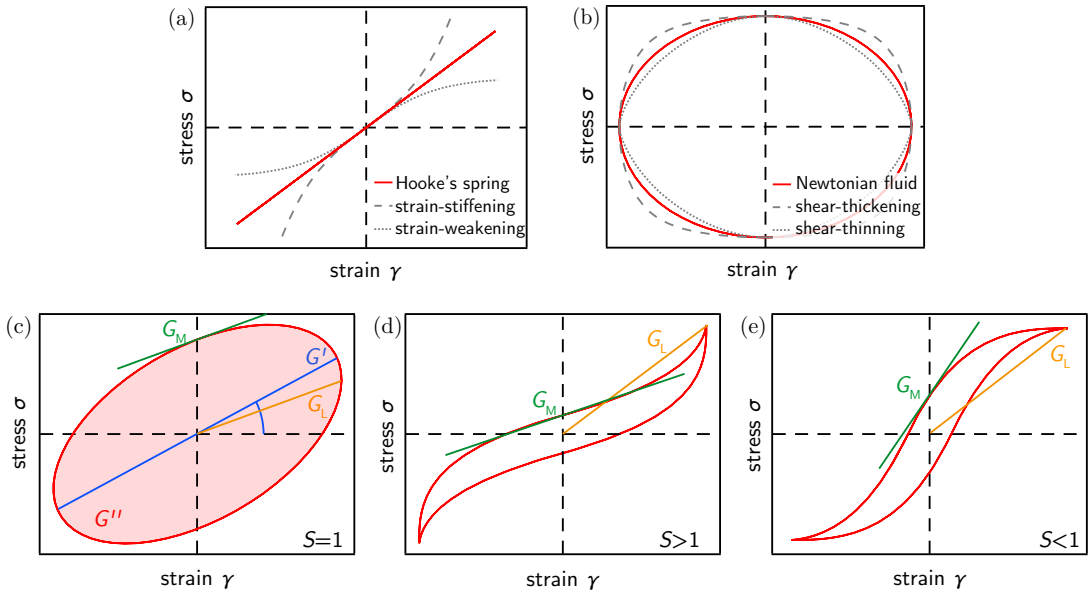

Figure 6.6: Schematic representation of the Lissajous curve for (a) a purely elastic solid (b) a purely viscous fluid (c) a linear, (d) a strain-stiffening and (e) a strain-softening viscoelastic material. (c)-(e) show schematically the definitions of the small strain elastic modulus G_M and the large strain elastic modulus G_L.

discussed above, the dissipative contribution is completely captured by the loss modulus G_1''. The elasticity is well described by two material parameters, the tangent modulus G_M and the secant modulus G_L (fig. 6.6(c)).

The former is defined as the slope of the stress-strain-relation at zero strain, and thus can be interpreted as a small strain elastic modulus:

$$G_M(\omega, \gamma_0) = \left.\frac{\mathrm{d}\sigma}{\mathrm{d}\gamma}\right|_{\gamma=0} = \left.\frac{\mathrm{d}\sigma}{\mathrm{d}t}\frac{\mathrm{d}t}{\mathrm{d}\gamma}\right|_{\gamma=0} \tag{6.16}$$

Using the Fourier series (6.14) for the stress response and substituting $t = 0$ and $t = \pi/\omega$, one obtains

$$\begin{aligned} G_M &= \left[\pm\gamma_0\omega \sum_{n,\mathrm{odd}} nG_n'(\omega, \gamma_0)\right] [\pm\gamma_0\omega]^{-1} \\ &= \sum_{n,\mathrm{odd}} nG_n'(\omega, \gamma_0) \end{aligned} \tag{6.17}$$

In the linear regime, the only contributing modulus is the first harmonic. The tangent modulus reduces to $G_M(\omega) = G'(\omega)$.

The secant modulus G_L is defined as the ratio of stress and strain at maximum strain γ_0, und thus serves as a measure of the elasticity at large strain:

$$G_L(\omega, \gamma_0) = \left.\frac{\sigma}{\gamma}\right|_{\gamma=\pm\gamma_0} \tag{6.18}$$

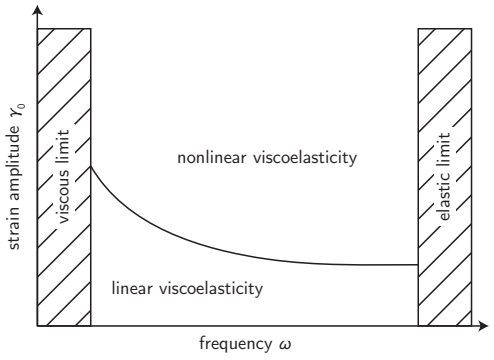

Figure 6.7: A schematic pipkin diagram maps the linear and nonlinear regime in dependence of the applied strain amplitude γ_0 and frequency ω.

Expressing the stress in terms of the Fourier series and substituting $t = \pi/2\omega$ and $t = 3\pi/2\omega$ yields

$$G_L(\omega, \gamma_0) = \sum_{n,\text{odd}} G'_n(\omega, \gamma_0) \tag{6.19}$$

As for the tangent modulus, the secant modulus reduces to $G'(\omega)$ in the linear regime.

Comparing the moduli $G_M(\gamma_0)$ and $G_L(\gamma_0)$ gives a relation of the elastic properties at small and at large strains. Thus, the elastic stiffening index $S(\gamma_0)$ is defined as the ratio of G_L and G_M:

$$S(\omega, \gamma_0) = \frac{G_L(\omega, \gamma_0)}{G_M(\omega, \gamma_0)} \tag{6.20}$$

A viscoelastic material in the linear regime, where $G_L = G_M = G'$, features $S = 1$. $S > 1$ describes a strain stiffening of the network (fig. 6.6(d)), while, for $S < 1$ the network strain softens (fig. 6.6(e)). In the case of a purely elastic material, this framework of elastic moduli also serves to characterize the nonlinearity. In the case of a purely viscous fluid, $G_M = G_L = 0$, so S is no longer defined.

The Pipkin Diagram The Lissajous figures and their quantitative analysis provide a sensitive tool for the detection of nonlinearity. The transition between linear and nonlinear behavior will depend not only on the shear amplitude but also on the applied shear rate and thus the frequency of the imposed sinusoidal strain. It is useful to map the regimes of linear and nonlinear shear response in dependence of the strain amplitude γ_0 and the applied frequency ω. These two parameters span an experimental phase space which is compactly represented in a Pipkin diagram, where the frequency is plotted on the abscissa and the strain amplitude on the ordinate (fig. 6.7) [155]. At very small frequencies, where the relaxation times of the sample are small compared to the characteristic flow time, the sample behaves like a Newtonian fluid. In the opposing limiting regime, where the relaxation times are much longer than the experimental time, the sample behaves like a Hookean solid. In-between, where the two characteristic timescales are of the same order, the sample exhibits viscoelastic behavior. An increase in strain amplitude induces a transition into the nonlinear regime, which will, in general, depend on the applied frequency.

6.2 Stress Stiffening of Entangled Actin Solutions

In this section, the rheological characterization methods described in the previous section are applied to probe the nonlinear behavior of entangled F-actin solutions. So far, a stress weakening as well as a stiffening response has been published for such filamentous solutions: While Xu *et al.* report that F-actin solutions exhibit stress hardening when subjected to step-stress deformations [140], Gardel *et al.* proclaim a transition from a weakening to a stiffening regime with increasing crosslinker concentration. For entangled solutions, they could not determine a hardening response using oscillatory methods. Before new insights in the molecular mechanism and the underlying deformation mode of the network can be gained, this contradictory results have to be explained and an appropriate measuring method has to be established.

First, the results of the LAOS experiments are presented, including the quantitative analysis of the Lissajous figures, the pipkin diagram as a compact mapping of the nonlinear phase-space and the Fourier transform analysis. The step-stressing protocol and the constant shear rate experiment are used as complementary methods to examine the nonlinear regime. All methods used in this section provide consistent results as long as the oscillatory stress and strain data of the LAOS measurements are regarded instead of G^* which is well defined only in the linear regime.

For all samples described in this section, the network parameters are the same: the actin concentration is $c_A = 9.5\,\mu M$, the average length $L = 21\,\mu m$ (adjusted by gelsolin), the temperature $T = 21°C$, and standard F-buffer salt conditions are maintained.

LAOS experiment

The first step in characterizing the properties of an entangled actin solution is a LAOS experiment. Strain-controlled oscillations at an intermediate frequency $\omega = 0.5\,Hz$ are applied increasing the amplitude γ_0 over the measurement (sec.6.1.4). The moduli G' and G'' provided by the rheometer decrease as γ_0 increases, indicating an apparent softening of the network (Fig. 6.8(a)). This can be attributed to two effects: firstly, the software assumes a linear response. Thus, it returns only the first harmonic of the elastic response leading to an incomplete analysis of the data. Secondly, the solution is too soft to withstand the large deformations, and a permanent plastic deformation is introduced to the filament solution [25].

Lissajous curves of the raw oscillation data visualize these points. As described in section 6.1.4, this parametric plot of the stress σ versus the strain γ represents a perfect ellipse in the linear regime, where the stress response is sinusoidal. As illustrated in fig. 6.8(b), this is valid for strains up to ∼15%. For larger oscillation amplitudes, the Lissajous figures become more and more distorted. The stress rate increases at large strains, indicating a hardening of the entangled actin solution.

This contradiction to the behavior of G' is caused by the approximation performed by the software. The algorithm considers only the first harmonic of the elastic response. Fig. 6.8(c) shows the Lissajous curve for the intermediate strain amplitude of 40% and an ideal ellipse fitted to the data, which corresponds to the first-order harmonic assumed by the rheometer software. Clearly, the fitted data hardly approximates the raw data

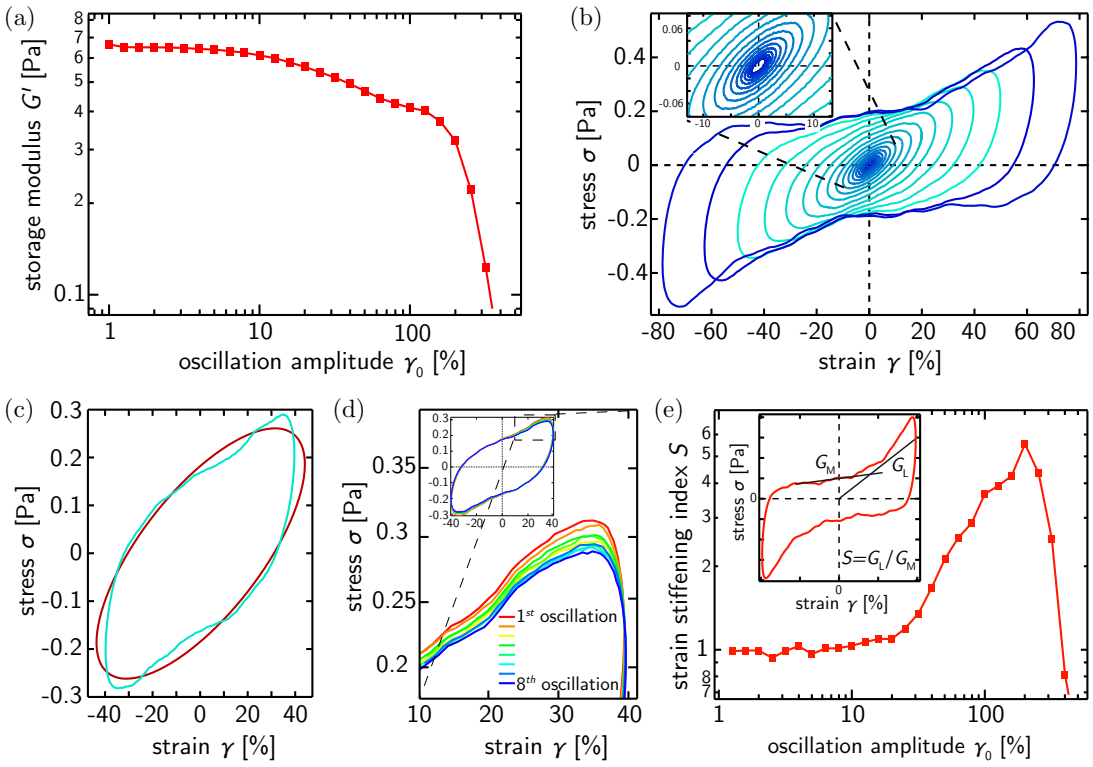

Figure 6.8: LAOS method: (a) Storage modulus G' as a function of the strain amplitude γ_0 at a frequency of $f = 0.5\,\mathrm{Hz}$ calculated by the commercial rheometer software. After a linear regime the network apparently softens at strains larger than 15%.(b) Lissajous curves of the raw data corrected for instrument inertia. At small amplitudes, the stress–strain relation displays a perfect ellipse with constant slope. For $\gamma \approx 15\%$ the Lissajous figures become distorted, indicating a hardening of the network. (c) Lissajous figure of the raw data for an oscillation amplitude of 40%. The ellipse fitted to the data demonstrates the insufficiency of first harmonic approximation. (d) Lissajous figure of the raw data for an oscillation amplitude of 40% over time showing the continuous change of the network response due to the large amplitude strains. (e) The elastic strain stiffening index S as a function of the oscillation amplitude γ_0. After a linear regime ($S = 1$), the stiffening index S increases until the network ruptures at strains $\gamma \approx 150\%$.

recorded by the instrument. Therefore, the software shows a softening of the network (fig. 6.8(a)), although the individual raw data curves indicate a hardening behavior.

To demonstrate the second point of the permanent plastic deformation, several oscillations at 40% strain amplitude are applied and the corresponding Lissajous figures are regarded over this extended measurement time. As illustrated in fig. 6.8(d), the peak stress of the Lissajous figure decreases with each oscillation, i.e. the sample softens during repetitive oscillation with large strain amplitudes. This softening is irreversible; even after a long waiting period the network never recovers completely. To minimize this plastic deformation in the further analysis, two oscillation cycles are applied to the sample, which is the minimal number the software can handle.

As shown above, the common moduli G' and G'' are insufficient to describe the nonlinear regime. For a more detailed analysis of the Lissajous figures, the small strain elastic modulus $G_{\mathrm{M}}(\gamma_0)$, the large strain elastic modulus $G_{\mathrm{L}}(\gamma_0)$ and the strain stiffening index $S(\gamma_0)$ (inset in fig. 6.8(e)) have to be included as described in the previous section. Fig. 6.8(e) displays the latter as a function of the applied oscillation amplitude. After the first linear regime, where $S = 1$, this analysis shows a stiffening for strains larger than $\gamma_c \approx 20\%$, indicated by a sharp increase in the strain stiffening index. At large strain values, the network ruptures and the modulus decays rapidly.

A compact visualisation of the nonlinear behavior is provided by the pipkin diagram. It maps the phase-space of the nonlinearity in dependence of the applied frequency f and oscillation amplitude γ_0 (sec. 6.1.4). For each point in the pipkin space exists a Lissajous figure corresponding to the oscillation at this specific frequency and amplitude. Fig. 6.9(a) shows the pipkin diagram for an entangled actin solution. Linear viscoelasticity is observed at small γ_0, resulting in an elliptic shape of the Lissajous figures. The increasing enclosed area for higher frequencies corresponds to a rise of the loss modulus G'' above the entanglement frequency; the nearly constant slope and thus constant storage modulus G' is characteristic for the plateau regime [156]. With increasing amplitude, the ellipses become progressively distorted; the onset of this nonlinearity shifts with decreasing frequency. The calculated strain stiffening index S is reflected by the color code: the brighter the Lissajous figure, the larger the corresponding S value. When the oscillation amplitude is increased beyond 50 %, the short range elastic modulus G_{M} decreases, corresponding to a decreasing slope at $\gamma \approx 0\,\%$. This is interpreted as a yielding of short-range elastic network components. On large scales, the stiffening on large scales is even more pronounced.

A more quantitative representation of the pipkin plot is the strain stiffening index as function of the applied amplitude γ_0 (fig. 6.9(b)). Nonlinear contributions become significant at strains around 20 %. The higher the frequency, the steeper is the increase in S. Complete yielding occurs at strains of $\sim$100 %.

Another sensitive method for the detection of nonlinearities in the LAOS experiment is the Fourier analysis of the raw data. It allows quantitative insights into the higher order composition of the response function (cf sec. 6.1.4). Fig. 6.10 shows the Fourier spectra of the stress response of an entangled actin solution. In the linear regime (at

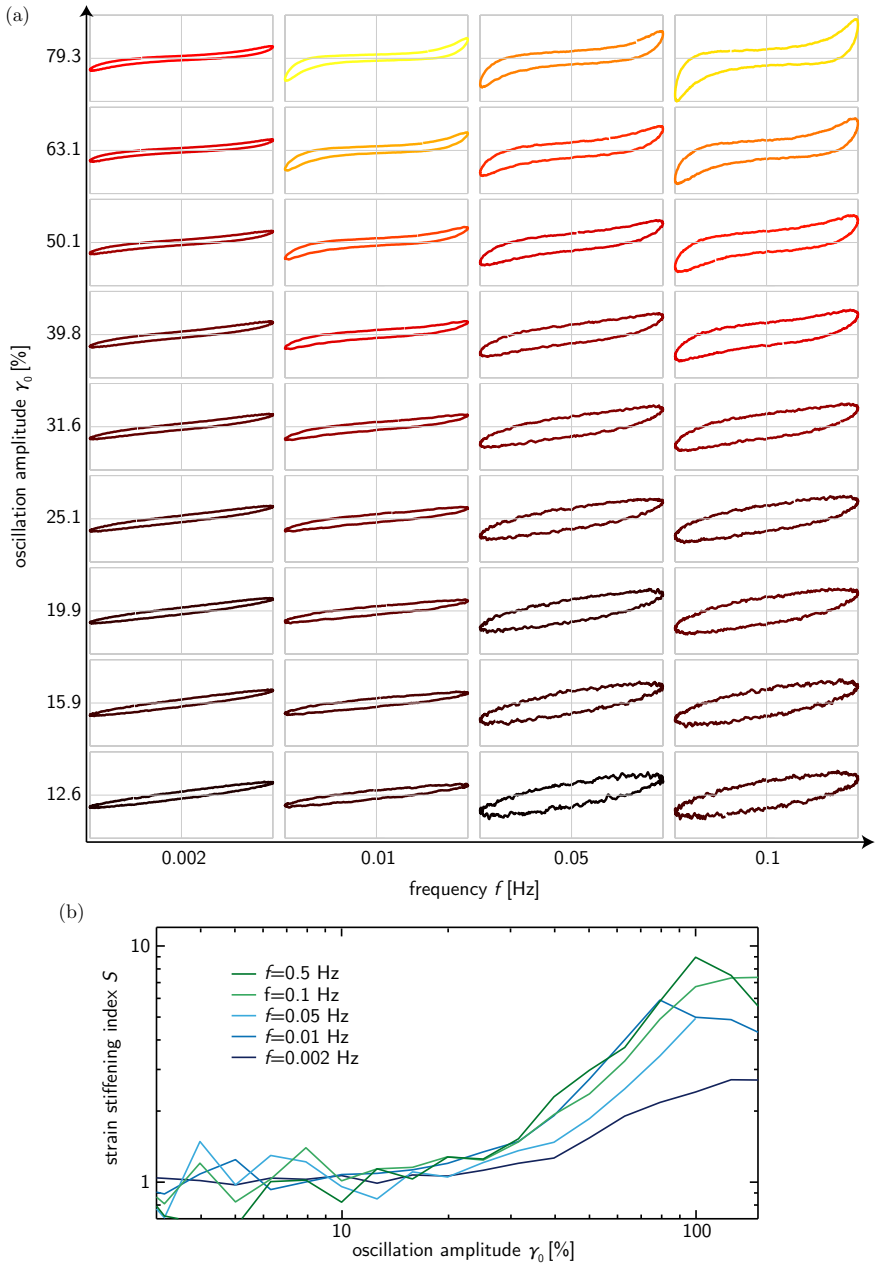

Figure 6.9: Pipkin diagram showing the evolution of nonlinearity in an entangled actin solution as a function of the oscillation frequency f and amplitude γ_0. (a) Each point in the phase space shows the corresponding Lissajous figure. The x-axis scale is chosen to fit the maximal strain, the axes ratio is kept constant. The color code is given by the corresponding S value. (b) The strain stiffening index S as a function of the oscillation amplitude γ_0 gives a quantitative representation of the pipkin plot.

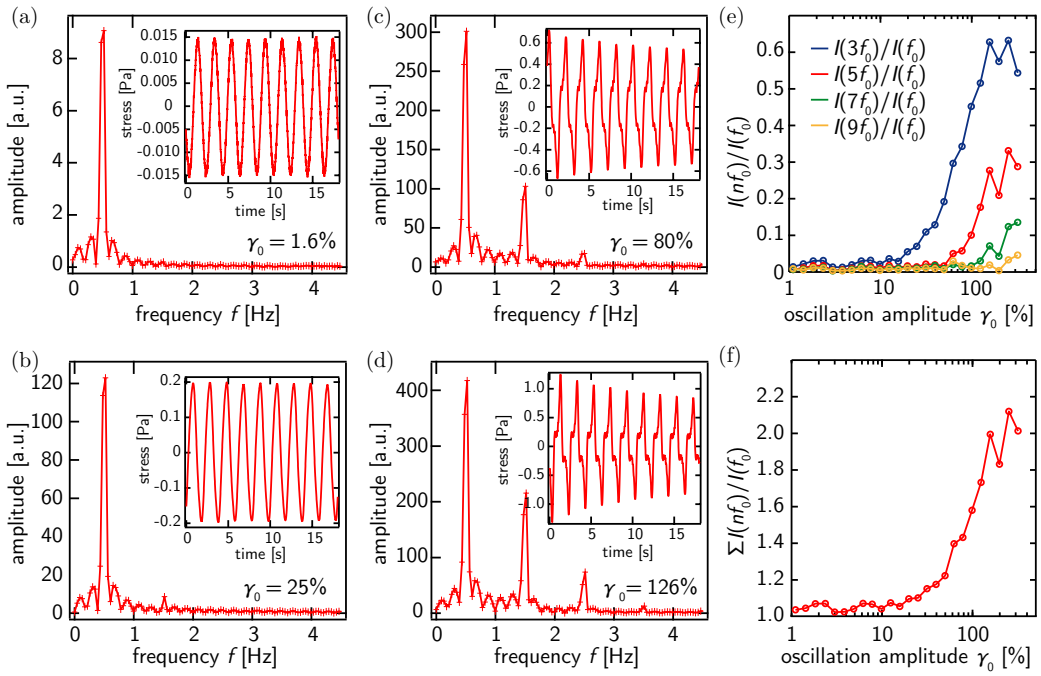

Figure 6.10: FTR analysis of the LAOS experiment: (a)-(d) Fourier transform of the stress response at different strains. The inset shows the inertia corrected stress response. (a) In the linear regime, the Fourier signal exhibits a single peak corresponding to the complex modulus G^*. (b) In the transition regime at $\gamma \approx 25\,\%$, a second peak appears at three times the excitation frequency. (c) Further increase in the oscillation amplitude leads to an increase in the contribution of higher harmonics until at strains just before rupturing of the network at $\gamma_0 \approx 125\,\%$ the stress response is highly distorted (d). (e) The amplitudes of higher harmonics normalized by the first show the development of nonlinearity in dependence of the oscillation amplitude γ_0. The strain at which harmonics significantly contribute to the stress response is shifted with increasing order. (f) The sum of all odd harmonics normalized by the first is a measure for the overall nonlinearity in the sample.

small strains), the Fourier transform exhibits a single sharp peak at the excitation frequency $f = 0.5\,\mathrm{Hz}$ (fig. 6.10(a)). An increase in the strain amplitude leads to the appearance of higher order contributions at frequencies which are odd multiples of the excitation frequency f_0 (fig. 6.10(b)-(d)). Fig. 6.10(e) shows the development of the higher harmonics in dependence of the strain amplitude γ_0. At small strains, the normalized intensities of higher harmonics tend to zero. Significant contributions begin to appear at approximately 20 %: The higher the order of the harmonic, the larger is the strain at which this contributes significantly. A measure of the nonlinearity of the sample repsonse is the sum of the amplitudes of all odd harmonics normalized by the amplitude of the first (fig. 6.10(f)).

The Fourier analysis offers a precise quantitative method for investigating the nonlinear regime. In general, it is possible to distinguish between elastic and viscous contributions. The downside is the danger plastic deformation caused by the oscillations at larger strains. For the FTR analysis shown, ten oscillation cycles repeated at

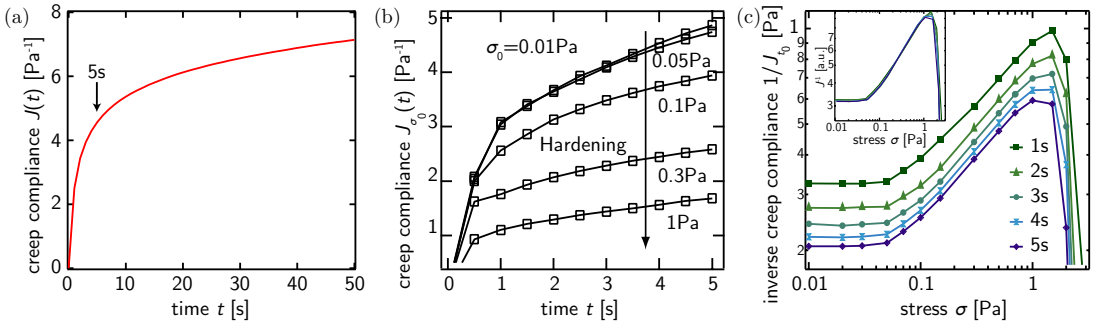

Figure 6.11: Step stressing protocol. (a) The creep compliance J as a function of time t during a stress pulse of $\sigma_0 = 0.05\,\mathrm{Pa}$. (b) The creep compliance $J(t)$ for different stress values σ_0. Above a critical stress, the network stiffens and J_{t_0} decreases. (c) The inverse creep compliance $1/J$ as a function of the applied stress σ in a step-stressing experiment evaluated at a certain time t_0. Inset: J_{t_0} collapse for different t_0.

each strain amplitude γ_0 are necessary to obtain a satisfying resolution in frequency (sec. 6.1.4). During repeated oscillations at strains in the nonlinear regime, the investigated sample softens. This corresponds to a gradual decrease in the peak amplitude of the stress response (fig. 6.10(c)-(d)). For two oscillation cycles which is the experimentally minimal number, the frequency resolution is $\Delta\nu = 0.5f$ which is quite imprecise and may hide occuring artefacts.

Step stressing protocol The step stressing protocol measures the viscoelastic properties of the sample by monitoring the strain response while a constant prestress is applied (section 6.1.4). The creep compliance of an entangled actin network, $J_{\sigma_0}(t) = \gamma(t)/\sigma_0$, shows three distinct regimes: a fast elastic response, a viscoelastic transition regime, and a viscous flow regime (fig. 6.11(a)). The stress pulse duration is set to 5 s. It is chosen to prevent entering the the viscous regime occurring after 10^4 s [157], where all the energy dissipates.

The nonlinear behavior is tested by increasing the stress amplitude. In the linear regime, the creep response is independent of the stress input. Above a critical stress amplitude, the network stiffens, indicated by a smaller increase in the creep compliance over time (fig. 6.11(b)).

The inverse of the creep compliance $1/J$ at a given time t_0 is a measure for the viscoelasticity of the network. Fig. 6.11(c) shows $1/J_{t_0}$ as a function of the applied stress σ. There are three different regimes distinguishable: After a linear stress-strain-relation at low forces, where the creep compliance is approximately constant, the network stiffens above a stress of $\sigma_c \approx 0.07\,\mathrm{Pa}$ with $1/J \propto \sigma^{0.4}$ until the network ruptures irreversibly at approximately 1 Pa. Within the 5 s stress pulse, the time development is independent of the stress applied and all curves can be rescaled onto a single master curve (fig. 6.11(c) inset). The stiffening is completely reversible; as long as no rupture has occurred, the series of stress pulses can be repeated with excellent agreement of the results, indicating that no permanent reorganization occurs. This is in contrast to the behavior observed by the LAOS experiment, where the repeatedly applied large strains

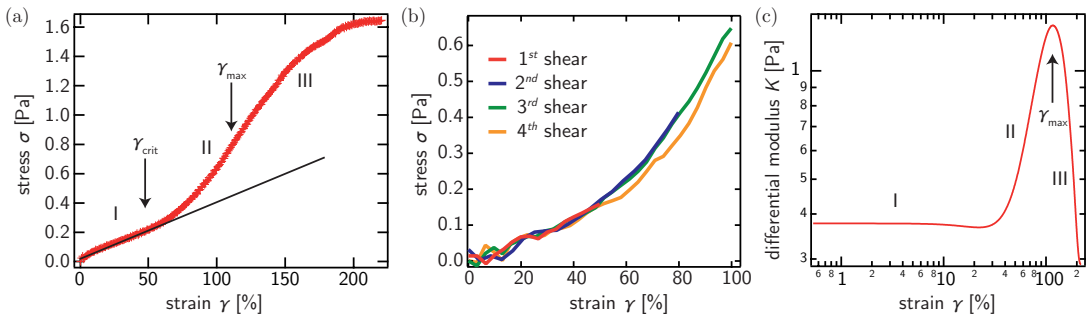

Figure 6.12: $\dot{\gamma}$-protocol: (a) Stress-strain-relation $\sigma(\gamma)$ for a shear rate of $\dot{\gamma} = 20\,\%$. After a linear regime (I) the network stiffens (II) until it ruptures at $\gamma_{\max}$ and the actin solution softens (III). Note that due to the viscoelastic nature of the network γ_{crit} is overestimated in this technique. (b) The hardening is reversible, the stress-strain relation can be reproduced perfectly as long as $\gamma < \gamma_{\max}$. (c) The differential modulus K as a function of strain γ reflects again the three different regimes.

presumably result in an irreversible deformation. In the step-stresses protocol, only a single short pulse is required for each stress level.

Constant shear rate experiment The time dependence of the nonlinear response of the network is investigated by the complementary shear experiment described in the previous section. After a first regime in which an approximately linear stress-strain relation holds, the network hardens above a critical strain of $\gamma_{\text{crit}} \approx 20 - 30\%$ which is indicated by the increase in the stress-strain-relation (fig. 6.12(a)). Note, that this method captures the overall viscoelastic response, including the viscous contributions. Therefore, a possible variation downward from the elastic limit can not be interpreted as softening of the network. It could just reflect the viscous contributions in the stress response. Furthermore, this is responsible for an overestimation of γ_{crit} by a compensation of nonlinear elasticity and viscous contributions.

Apparent softening of the actin solution starts at a maximal strain of $\gamma_{max} \approx 100\%$, discernible in a turning point in the stress-strain-relation. The hardening is completely reversible as long as $\gamma < \gamma_{max}$ (fig. 6.12(b)). Thus, no permanent plastic deformations are induced. Once the strain exceeds γ_{max}, the network softens irreversibly. To facilitate the comparison with results of the step stressing protocol, the differential modulus $K(\gamma)$ is calculated. This shows qualitatively the same behavior as $1/J(\sigma)$ (fig. 6.12(c)): After a constant linear regime, the network hardens until irreversible rupturing occurs.

Summary/Discussion Contradictory results for the behavior of entangled actin solutions have been described in the literature so far [139, 140] . These analysis were partially based on the evaluation of the moduli G' and G'' provided by the rheometer software. As shown in this section, this discrepancy is resolved by an analysis of the oscillatory response function over repeated oscillation cycles. Based on the more accurate analysis of the LAOS experiments (Lissajous evaluation or FTR analysis), all the methods described in this section show qualitatively the same nonlinear behavior

for entangled actin solutions. However, as the described methods measure different moduli with different viscous and elastic contributions and, moreover, in a strain- and stress-controlled manner, a direct comparison between them is not possible. However, the values of γ_{crit} and γ_{max} measured by LAOS and by the constant shear experiment are in excellent agreement.

Although the more accurate analysis of the LAOS experiment captures the strain stiffening of entangled actin solutions, there still remains the problem of the occurrence of plastic deformations during oscillations at large amplitudes (fig. 6.8(d)). This makes this method to be less adequate for such soft samples as entangled actin solutions. In the step-stressing protocol and the constant shear rate experiment, the effects of plastic deformations are reduced, which is discernible by the complete reversibility of the hardening up to γ_{max}. In the first, the network is deformed on a short time scale, followed by a long relaxation time. Unlike in LAOS experiments, the network can completely recover after large deformations, resulting in a clearly enhanced reproducibility. The drawback of these methods is the fact that the differentiation between elastic and viscous contributions is not possible. One can minimize the viscous effects by evaluating the step stressing protocol within the first seconds or by increasing the shear rate in the constant shear experiment.

The question remains what happens at γ_{max} when the network yields. Though the elasticity recovers slightly, the modulus does not reach its original value – even after some hours of waiting period. One can imagine different scenarios: The drop-down in elasticity could be due to breakage or shear alignment of the actin filaments. Another possibility could be slippage or uncoupling from the rheometer plates. Measurements using a shearing tool combined with a confocal microscope have shown that in the case of actin/filamin networks the bundles detach from the surface and the network collapses [158]. Similar experiments[3] indicate that also entangled actin solutions detach from the rheometer plates and collapse. This collapse can be explained by the negative normal stress reported for stiffening filamentous gels [159].

[3]performed by K. Schmoller

6.3 Dependence of the Nonlinear Behavior on Various Network Parameters

To further understand the nature of the nonlinear rheology, an extensive study of the nonlinear behavior of entangled actin solutions is performed, based on the precise experimental techniques presented in the preceding section. It is found that the experimental conditions remarkably influences the occurrence and characteristics of the stiffening behavior. The nonlinearity can be finely tuned by the ambient temperature, buffer salt concentrations or the filament length and concentration, while the linear response is not affected by these parameters.

Ambient temperature The ambient temperature, which can be precisely adjusted by the Pelletier element in the bottom plate of the rheometer, has a significant effect on the degree of stiffening. This dependence is demonstrated by the results of the step stressing protocol performed at different T values shown in fig. 6.13(a). Starting from the standard temperature of 21 °C, a decrease leads to a significantly enhanced hardening. With increasing temperature, the slope in the nonlinear regime gradually diminishes. The displayed inverse creep compliances measured at temperatures between 18 °C and 27 °C show a decrease of the power-law exponent x in the nonlinear regime with temperature. The hardening vanishes completely above $T \approx 25\,°\mathrm{C}$. Overall, x features a roughly linear dependence on T (fig. 6.13(b)), considering that the short nonlinear regime makes a precise analysis difficult.

Surprisingly, neither the linear regime in fig. 6.13(a) (not shown) nor the frequency-dependent linear shear moduli G' and G'' in the range of 0.01-10 Hz show a significant change with temperature (fig. 6.13(c)). The strong dependence of the network response on temperature is only observable in the nonlinear regime.

Salt concentration Completely analogous observations were made for changes in the electrostatic screening of the solution. Reducing the monovalent salt concentration from 100 mM to 10 mM has a very similar effect on the nonlinear response as a raise in temperature. (fig. 6.13(d)). Neither the linear moduli nor the polymerization speed is influenced by the low-salt conditions (fig. 6.13(e)). At this low salt concentration, a stiffening can be induced by lowering the temperature to 13 °C (fig. 6.13(d)). The characteristic strains γ_{crit} and γ_{max} are shifted to smaller values.

This dependence on the buffer salt concentration could be either an ion-specific effect related to the Hofmeister series or given by pure electrostatics. To test this further, the concentration of 90 mM KCl is replaced by a kosmotropic and a chaotropic salt, NaCl and CsCl, respectively. No differences can be detected in the nonlinear response of the network. This is a strong indication that a shift of the transition temperature by changing the salt concentration is a purely electrostatic effect. The linear response is not influenced by the type of monovalent salt.

Time dependence The time dependence of the nonlinear response is investigated by the constant shear rate experiment. To assure the equivalence of the step stressing pro-

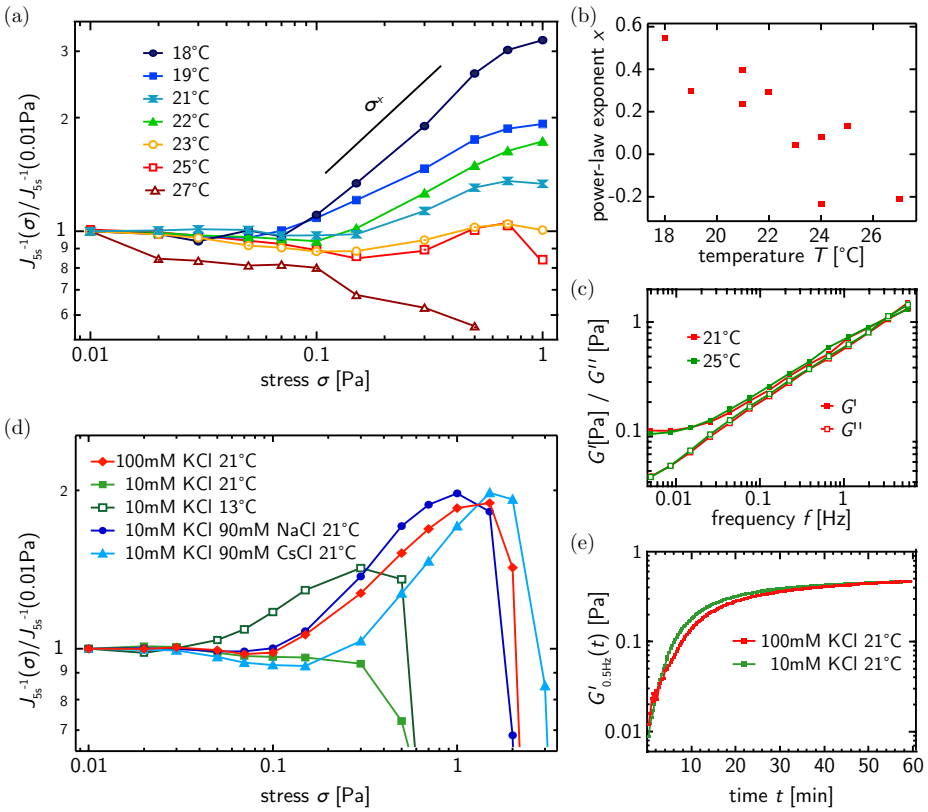

Figure 6.13: Step stressing protocol: (a) Temperature dependence of the nonlinear behavior: The inverse creep compliance $1/J$ normalized by $1/J(0.01\,\text{Pa})$ as a function of the applied stress σ for various temperatures between 18 °C and 27 °C at standard salt conditions. (b) Apparent power law exponent x of $1/J(\sigma) \propto \sigma^x$ versus the temperature T. (c) Frequency dependence of the moduli G' and G'' in the linear regime for two different temperatures, each averaged over five different samples. (d) Salt dependence of the nonlinear behavior: The inverse of the creep compliance $1/J$ normalized by $1/J(0.01\,\text{Pa})$ as a function of the applied stress σ for various buffer salt conditions. (e) Storage modulus $G'_{0.5\,\text{Hz}}$ as a function of time t recorded during polymerization for high and low salt conditions.

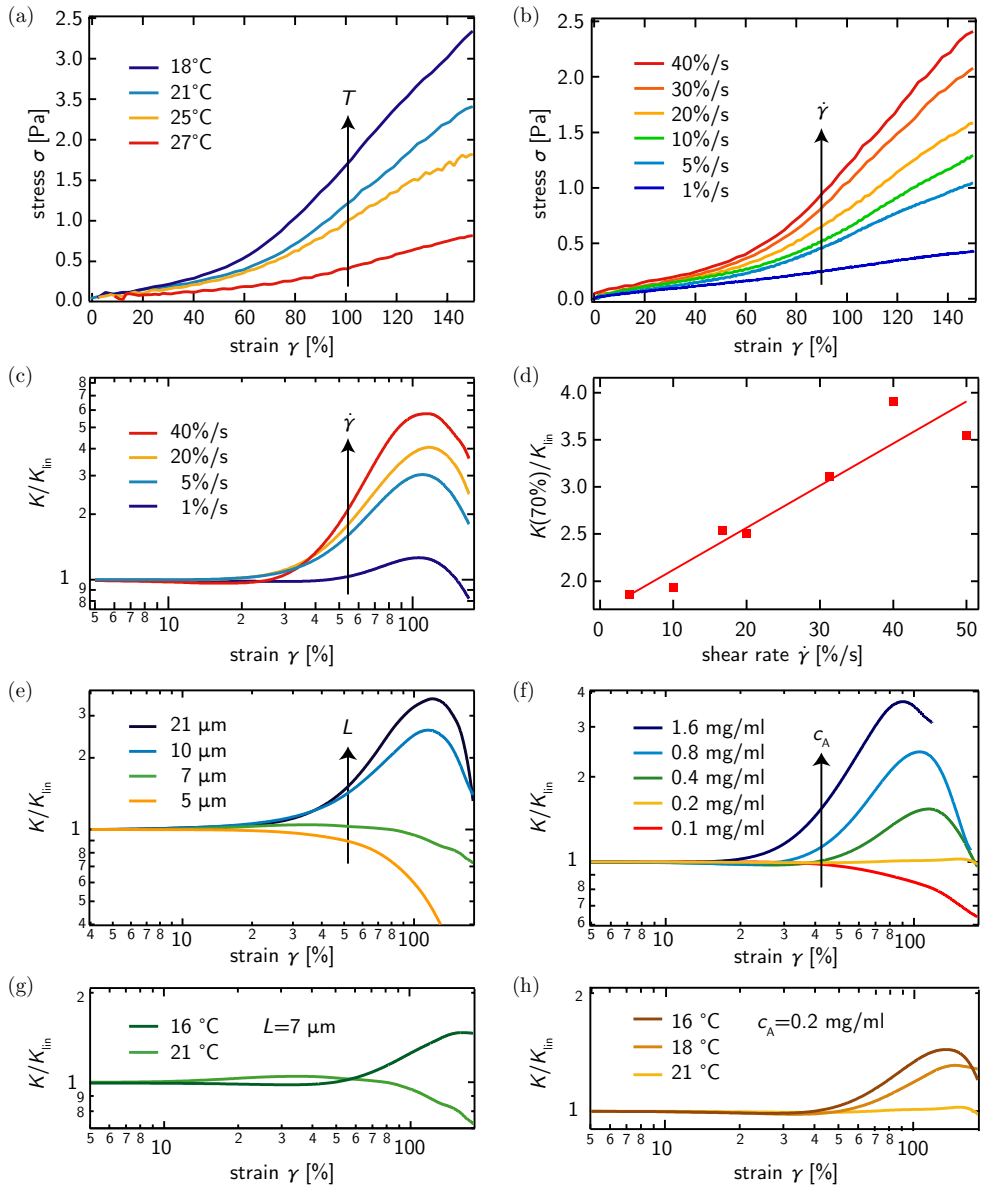

Figure 6.14: The transition as a function of various network parameters ($\dot{\gamma}$-protocol): The stress σ versus the strain γ in a shear experiment at (a) various temperatures between 18 °C and 27 °C and (b) various shear rates between 1 %/s and 40 %/s. (c) Differential modulus K normalized by the modulus in the linear regime K_{lin} versus the strain γ. (d) The normalized differential modulus $K(70\,\%)/K_{\mathrm{lin}}$ as a function of the shear rate at 21 °C. The modulus increases approximately linearly with the applied shear rate. (e)-(h): The normalized differential modulus K/K_{lin} versus the strain γ for (e) different filament lengths L and (f) different actin concentrations c_{A}. The hardening can be re-induced for (g) $L \approx 7\,\mu\mathrm{m}$ and (h) $c_{\mathrm{A}} = 0.2\,\mathrm{mg/ml}$ by lowering the temperature to $T = 16\,^{\circ}\mathrm{C}$.

tocol to this method, the temperature dependence of the stress response is investigated with the shear experiment (fig. 6.14(a)): the same quantitative transition is found in the shear rate experiment and the compliances described above

A change in the shear rate $\dot{\gamma}$ induces a similar transition between hardening and softening as the ambient temperature. The lower the pulling velocity the less pronounced is the stiffening of the network(fig. 6.14(b)). To facilitate the comparison with the results of the step stressing protocol, the differential modulus $K(\gamma)$ is calculated (fig. 6.14(c)). It shows the same qualitative behavior as $1/J(\sigma)$: After a constant linear regime, the network hardens until rupturing occurs.

To quantify the dependence of the nonlinear modulus on the applied shear rate, it is evaluated at a certain strain in the nonlinear regime, $K(70\%)$, and normalized by the linear modulus K_{lin}. This measure of nonlinearity increases approximately linearly with $\dot{\gamma}$ (Fig. 6.14(d)).

Filament length and concentration In a next series of experiments, the lengths of the filaments are varied by the use of gelsolin. A transition from hardening to softening is observed as the average filament length decreases (fig. 6.14(e)): For solutions with filaments shorter than approximately 7 µm, a softening is observed, while for longer filament solutions a hardening is reported. Surprisingly, the transition length can be shifted by lowering the temperature: while solutions of approximately 7 µm filament show a softening at 21 °C, a hardening is observed for the same network at 16 °C (fig. 6.14(g)). Again, the linear response is not affected.

A similar behavior is observed by changing the actin concentration. Varying the filament density influences the degree of hardening. The higher the actin concentration the more pronounced is the increase in the modulus K (fig. 6.14(f)). Also in this case, networks that show a softening response at 21 °C feature a hardening response if the temperature is at 18 °C or 16 °C (fig. 6.14(h)).

Master curve The data collected on entangled actin solutions demonstrate not only a remarkable sensitivity of the nonlinear regime on various network and ambient parameters but also suggests an interchangeability of these parameters. For instance, a decrease in the salt concentration can be compensated by an appropriate decrease of the ambient temperature (fig. 6.13(d)), while increasing temperature is compensated by an increase in shear rate. This nicely demonstrates the rheological redundancy principle. Indeed, this is shown in fig. 6.15 with 25 curves for different T, L, c_{A}, and $\dot{\gamma}$ values. A single master curve can be found on which all stress-strain relations neatly collapse provided they are rescaled by their characteristic strain and stress values, γ^* and σ^*, respectively.

This remarkable finding is a hint that the changes in temperatures, salt concentration, filament length and density affect the nonlinear response in the same way and can be interpreted as a rescaling in time. This leads to the glassy worm-like chain model which is presented in the following section.

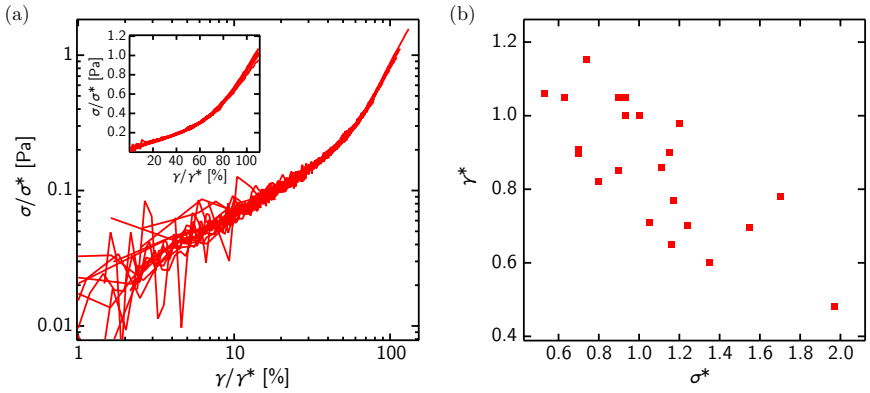

Figure 6.15: Rheological redundancy in the $\dot{\gamma}$-protocol: (a) 25 stress-strain curves for different T, L, c_A, and $\dot{\gamma}$ collapse onto a single master relation upon rescaling each curve by its characteristic strain and stress values. The spread of the data at low-strain values is due to instrument limitations causing measurement uncertainties. Inset: linear representation of the data. (b) The characteristic rescaling factors $\gamma^\star$ versus $\sigma^\star$ for the data shown in (a).

6.4 Discussion of the Mechanical Redundancy with the Inclusion of the Glassy Worm-Like Chain Theory

The mechanical response of reconstituted biopolymer networks, particularly in the nonlinear regime, is attracting a lot of attention [7, 139, 160]. Former studies explored the viscoelastic moduli in dependence of the deformation amplitude in an oscillatory manner, regardless of the non-sinusoidal stress response in the nonlinear regime [140, 160]. Recent investigations consider the differential elastic modulus $K'(\tau)$ measured in a prestress experiment where small stress oscillations are imposed onto the sample in addition to some (possibly) large prestress τ. A typical $K'(\tau)$ measured for biopolymer networks as well as for whole cells, in which the prestress may be self-generated, exhibits a continuous but sharp transition at a critical prestress τ_c from a linear response regime, where K' is independent of τ, to a (reversible) strain hardening elastic regime, where $K'(\tau)$ increases according to a power law $K' \propto \tau^x$ [7, 137, 139]. The exponent x and the critical prestress τ_c or the corresponding critical prestrain $\gamma_c \simeq \tau_c/K'_c$, respectively, vary somewhat with composition and polymer concentration but are generally found to lie in the range $x = 1 - 1.5$ and $\gamma_c = 1 - 200\,\%$ [7, 139, 161].

Competing interpretations have been proposed for the characteristic dimensionless numbers x and γ_c, either in terms of *affine stretching* [139, 160] or *non-affine bending* [137] of individual polymer strands. While both interpretations seem successful in rationalizing the experimental observations, they rest on incompatible — and so far not directly assessable — assumptions about how the macroscopic sample deformation is transmitted to the individual stress-bearing elements, predominantly the single actin filaments. For semidilute *solutions* of stiff polymers, on the other hand, in which the polymers form merely physically entangled networks, shear-thinning was theoretically predicted [162] and experimentally observed, even in the presence of small amounts of crosslinkers [139].

The strong dependence of x on experimental conditions presented in this chapter implies that the nonlinear response itself is a very sensitive indicator for molecular interactions present in the network – with probably only limited predictiveness on the deformation behavior dominating the network response. To determine the latter combined detailed structural insights and concentration dependencies of the mechanical response are mandatory [22, 163, 164]. While the overall functional form of curve $1/J(\sigma)$ in fig. 6.11 resembles very much that measured in crosslinked (and prestressed) *in vitro* samples or even whole cells, one notices some distinctive differences: In contrast to the latter case [137, 139], the power law exponent x apparently does not reflect a characteristic material property of the individual stress bearing elements, as it can be varied over a broad range by varying the shear rate, the temperature or the ionic strength. Although clearly the semiflexible nature of the filaments gives rise to the network response, the nonlinear response is not only dependent on the single filament stretching behavior, as suggested by [160], but rather sensitively dependent on structural details and molecular interactions [22].

Changes in the mechanical response with changing network or ambient parameters could only been observed in the nonlinear regime. This can be explained by a simple model of non-permanent shear induced interactions between individual filaments. The different exponents can then be attributed to differences in their density. This model rests on two hypothesis: First, on the general notion that F-actin solutions are stabilized by electrostatic repulsions that are, however, somewhat indented by an attractive contact force. The expected qualitative distance dependence of the direct pair interaction potential between two (non-parallel) actin filaments is schematically sketched in fig. 6.16. Secondly, one assumes that upon shearing the sample beyond a critical shear strain γ_c, adjacent actin filaments are pushed together such that their mutual electrostatic repulsion is overcome and a relative minimum in their pair interaction potential becomes accessible, which acts as a transient bond causing stress hardening. The differential modulus K increases in proportion to the number of these non-permanent bonds. The apparent power-law exponent x is found to shift continuously upon varying the ambient conditions (temperature, salt) and the shear rate, which presumably reflects the variable rate of transient bond formation. The critical shear strain γ_c is found to be about 25 %. This value is well accounted for by a speculative but straightforward *non-affine* version of the tube model of semidilute solutions of stiff polymers, introduced as the "dilatancy model" [165].

The interchangeability of temperature and time (fig. 6.14(b)) suggests that the effect of temperature (or filament length and concentration) on the nonlinear behavior amounts essentially to a rescaling in time. The changes in the regarded (or possible further) parameters, all seem to affect the rheological response chiefly by a stretching of the relaxation spectrum. This dependence on microscopic interactions can easily be incorporated by the recently introduced glassy worm like chain model [141, 166].

The Glassy Worm-Like Chain Model The glassy worm-like chain (GWLC) is a minimalistic model for solutions of polymers interacting via small adhesive patches. It

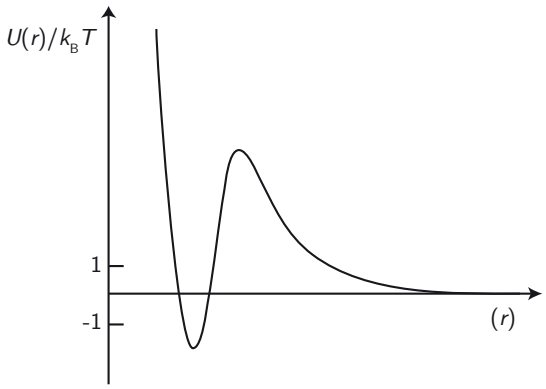

Figure 6.16: Schematic sketch of the hypothetical pair potential $U(r)$ as suggested in [141]. Long range electrostatic repulsion is combined with a short range attractive contact force.

is obtained from the ordinary, weakly bending WLC (sec. 6.1.1) by an exponential stretching of the relaxation spectrum. The relaxation times τ_n of eigenmodes with a wavelength $\lambda_n = L/n$ longer than a characteristic interaction length Λ are multiplied by an exponential stretching factor:

$$\tau_n \to \tilde{\tau}_n = \begin{cases} \tau_n & \text{if} \quad \lambda_n < \Lambda \\ \tau_n \mathrm{e}^{N_n \mathcal{E}} & \text{if} \quad \lambda_n > \Lambda \end{cases} \tag{6.21}$$

where N_n is the number of interactions per wavelength λ_n

$$N_n = \lambda_n / \Lambda - 1 \tag{6.22}$$

This modification is reminiscent of the generic nonequilibrium trap models of soft glassy rheology [167, 168], but concerns equilibrium dynamics here.

In a semidilute solution of polymers (as the entangled actin samples in this work), the characteristic lengthscale Λ corresponds to the entanglement length known from the tube model (sec. 6.1.1) and N_n corresponds to the number of entanglements an undulation of wavelength λ_n has to overcome to relax. The stretching parameter $\mathcal{E}$ controls the degree of slowing down caused by the interactions. In view of the sensitivity of the rheology to temperature and ionic strength reported above, it seems natural to think of $\mathcal{E}$ as the characteristic scale (in units of thermal energy) for energetic barriers. While protein interactions remain poorly understood, many observations hint at temperature-sensitive (unspecific) adhesive contact interactions incompletely screened by electrostatic repulsion [169], which would match well with this interpretation and with our observations. In the spirit of generic free-volume theories [170], the parameter $\mathcal{E}$ might moreover accommodate free energy contributions from caging and entanglement. In any case, simple exponential scaling of the relaxation times in the wavelength λ seems plausible. The GWLC model does only affect the relaxation times but not the amplitudes $\mathbf{a}_n$ (cf. eq. (6.2)). In principle, one could imagine that also the amplitudes of the eigenmodes are changed by the interaction with the disordered environment. However, already the slowing-down of the relaxation spectrum captures the most important mechanisms in the observed glass transition.

Appealing to the intuition of the stretching parameter as a (free) energy barrier, externally or internally generated stresses may arguably be expected to contribute additively to $\mathcal{E}$. The force therefore tilts the energy landscape in the spirit of a Kramers

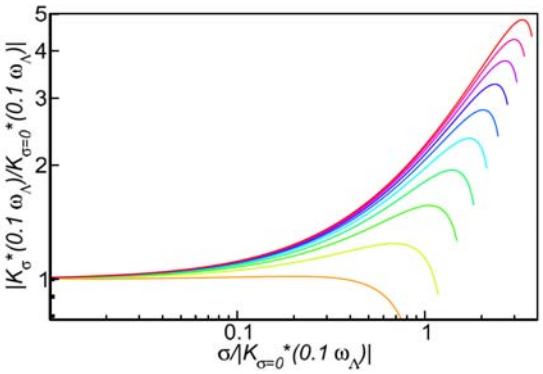

Figure 6.17: Nonlinear differential shear modulus $|K_\sigma^*(\omega)|$ of a glassy worm-like chain as function of prestress σ from ref. [171]. Both axes are normalized by the linear modulus $|K_{\sigma=0}^*(\omega)|$. The parameters pertaining for the free-energy wells are $\Delta = 0.25\,\mu m$, $\Lambda = 1.5\,\mu m$, and $\mathcal{E} = 4...40$ from bottom to top and were chosen to mimic the experimental data.

escape model and thus, it can either "help" the polymer to overcome the energy barrier, or trap the polymer deeper, dependent on the sign of the force. The stretching parameter $\mathcal{E}$ is then replaced by $\mathcal{E} - f/f_T$ where $f_T \equiv k_B T/\Delta$ represents some characteristic scale of the thermal equilibrium tension present in an unstressed sample so that Δ may be interpreted as a characteristic (effective) width of the energetic traps and barriers. It is important to note that the parameters $\mathcal{E}$ and Δ are to be understood as effective parameters. They cannot generally be interpreted as some distinct features in the interactio potential as sketched in fig. 6.16.

Analogously to the standard WLC model, various time dependent parameters can be calculated. Pertinent predictions suitable for a qualitative comparison with the rheology data in the nonlinear regime can be derived by subjecting the glassy worm-like chain to a prestress and calculating the complex frequency dependent shear modulus. Fig. 6.17 shows its absolute value $|K_\sigma^*(\omega)|$, evaluated at a fixed frequency $\omega = \tau_\Lambda^{-1}$ in the "slant-plateau" regime, as a function of the prestressing tension f, which is expressed as an equivalent prestress σ. The parameters were chosen to mimic the experimental conditions. Although the increase in the modulus is due to the stiffening of the polymers caused by the prestress, its sharp downturn signals the breakdown of the stretching of the relaxation spectrum when $f \approx \mathcal{E} f_T$ and the sticky contacts yield to the stress.

To support this theory of an exponentially stretched relaxation spectrum it would be desirable to measure the equilibrium long-time dynamics of the samples on microscopic and macroscopic scales. Because of the technical difficulty of low-frequency linear rheometry for such soft samples as entangled actin solutions, the linear response can better be probed by high-precision Dynamic Light-Scattering (DLS) over several orders of magnitude in time. The DLS data presented in [171] show that the scattering function acquires a pronounced logarithmic tail at low temperature T and large filament length L, in stark contrast to more fluid samples at higher temperature [172]. The slopes of these logarithmic tails determine the apparent power-law exponent characterizing the corresponding frequency-dependent microrheological moduli. These tails of curves measured at varying actin concentrations collapse on rescaling the time axis providing a further illustration of the superposition principle, here for the parameter c_A. Beyond an unambiguous demonstration of the stretching of the relaxation spectrum in form of the logarithmic decay, the DLS data represent strong independent evidence for the rheological redundancy inferred from the nonlinear rheological measurements shown

above.

It is an intriguing question as to what extent the results for pure actin solutions shown above are representative also for the mechanics of crosslinked networks and live cells. The here observed mechanical redundancy, where all system parameters can be interchanged and similar mechanical behavior can be obtained is far reaching: also for crosslinked networks such a multi-dimensional redundancy is present. For α-actinin the linear mechanical response was tunable not only by the crosslinker concentration but also by temperature variations [173]. The nonlinear behavior of bundled networks can be tuned either by strain rates or crosslinker concentration [174] – and it is conceivable, that different mesoscopic structures result in comparable linear and nonlinear responses. This variability is possibly an important prerequisite for the often observed genetically redundancy in living cells [175]. In the theoretical model of the GWLC, too, reversibly (or irreversibly) crosslinked networks are effectively contained (as the limiting case $\mathcal{E} \to \infty$). Actually, a comparison of computed linear rheology moduli with published microrheology data for live cells shows quite satisfactory agreement. This might be interpreted as further evidence that cells and multicellular organisms do indeed live at the edge of a glass transition [176, 177].

Chapter 7

Outlook

The present work has demonstrated that experiments on *in vitro* reconstituted actin networks are ideally suited to gain insights in intriguing cellular processes. The SAXS experiments on actin bundles described in section 4 suggest the discrepancy between the helical structure of the actin filament and the hexagonal packing inside the bundle to be the size limiting mechanism in bundle formation. This provides an explanation for the well-defined size of bundle structures observed *in vivo*. The ABPs fascin and espin, both, induce an overtwist of about 1° per actin residue in the filament to overcome the geometrical mismatch. While bundles formed by fascin or espin have approximately the same maximal width of about 20 filaments, a combination of both ABPs leads to thicker bundles.

The experiments on the depolymerization kinetics of crosslinked actin networks that have been presented in section 5 reveal a generic stabilizing effect of actin binding proteins. All proteins examined in this work decrease the depolymerization rate of actin filaments. Even the actin depolymerizing factor cofilin is not sufficient to facilitate a fast disintegration of highly crosslinked actin networks. This effect provides a powerful tool in stabilizing distinct stress bearing actin structures. Furthermore, it implies that cells need additive processes to disintegrate the bundle structures.

The last sections addressed the nonlinear mechanics of purely entangled actin solutions. First, the characterization of different measuring techniques has shown that the choice of the measuring protocol and the appropriate analysis are crucial to detect stress stiffening in such low-viscous systems. Instead of the universal power law reported earlier, a continuous transition from a regime of stress hardening to stress weakening is found, depending on various network parameters like temperature, salt concentration or filament length. Beyond the relevance for describing the mechanical behavior of living cells, this is particularly interesting if regarded in the framework of polymer physics.

More relevant for *in vivo* cytoskeletal networks is the investigation of crosslinked or bundled polymer systems. Concurrent studies have shown that the nonlinear response of ideally crosslinked networks can be understood in terms of entropic stretching of the filaments. On the other hand, a network of bundles can be described by enthalpic bending undulations.

While the mechanical response of actin networks is by now well understood, the underlying principles of the self-organization in actin bundles are still elusive. Different mechanisms seem to exist that can overcome the geometrical constraint on bundle di-

ameters. While the present measurements have shown that some ABPs overtwist the actin helix, others like filamin are thought to supertwist the entire bundle to adjust filament and bundle symmetries. Analogously to espin and fascin, a combination of TEM and SAXS measurements will corroborate (or disprove) this hypothesis. Determining the structure might also explain the tendency of filamin bundles to aggregate to larger structures virtually unlimited in size.

The first experiments performed in th framework of this thesis on composite networks featuring more than one ABP show an enlarged maximum diameter. However, the molecular assembly inside the bundle is still an open issue. *In vivo* experiments suggest that sub-bundles formed by one ABP are consecutively linked by the second one. *In vitro*, this spatial partition can be realized by a subsequent addition of the ABPs. Comparing the bundle structures polymerized in the presence of both ABPs and formed by a successive addition of the crosslinkers might shed some light on the bundle construction. Is there a difference in the mechanical properties of homogeneously or hierarchically formed bundles? This might also have a significant influence on the disintegration of the bundles.

As shown in this work, cells need additional processes to disintegrate highly crosslinked actin structures. The activity of the depolymerization factor cofilin on its own is not sufficient. A possibe mechanism is provided by the auxiliary addition of active molecular motors. The molecular basis of this disintegration is not yet understood. A possible approach is the measurement of the forces needed to pull out single actin filaments by an optical tweezer. If the process of bundling is highly cooperative as it is suggested for espin by the switch-like change in the twist-state, this might influence the integrity of the overall bundle.

Another factor influencing the bundle stability might be the impact of externsl forces. When filopodia are pushed by the retrograde flow into the lamellipodium, not only the action of myosin will disintegrate the bundles. Rather, the mechanical resistance of the dense actin network will influence the binding potential of the crosslinking proteins, which will in turn influence the depolymerization kinetics of the actin filaments. Furthermore, there is an ongoing discussion whether a distortion in the actin helix facilitates the binding of cofilin and thus accelerates disintegration [36, 37]. Certainly, it would be of adverse effect for a living organism if the application of external forces accelerates the disintegration of stress bearing elements in the cell. Indeed, an increase in tensile strength is reported to evoke a fortification of stress fibres and their focal adhesion points. This raises the question if the impact of forces depends on the direction of its application. Does pushing or stretching have different effects on the bundle stability or the mechano-sensing signaling cascades?

A detailed analysis of the properties of bundles subjected to an external force is mandatory. A first step could be performing depolymerization experiments under force combining shear and diffusion chamber. This will allow for a controlled deformation and simultaneous addition of depolymerization agents. The downside of this macrorheological approach is the averaging over several deformation modes in the sample. In a complex bundle network, some bundles will be stretched while others are compressed or twisted. Inevitably, this will require experimental techniques which enable manipulating a single bundle. First steps in combining multiple optical traps look promising.

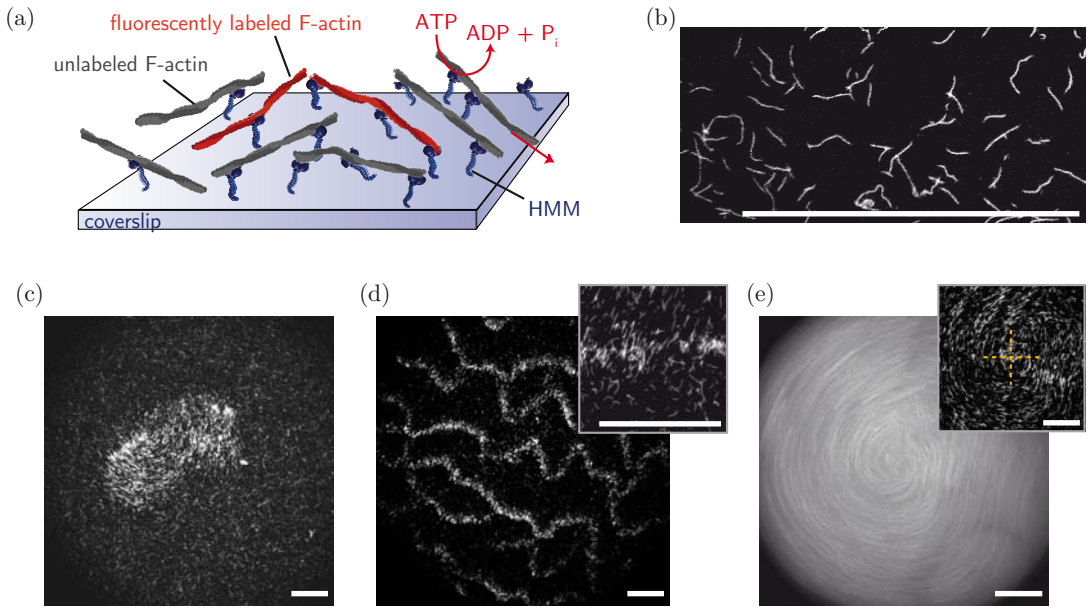

Figure 7.1: High density motility assay: (a) Schematic of the setup: HMM molecules are immobilized on a coverslip. The motion of the gliding filaments is visualized by a small fraction of fluorescently labeled reporter filaments. (b) For low actin concentrations, a disordered phase is found. The individual filaments perform persistent random walks without any specific directional preferences. At high filament density, patterns of collective motion emerge: (c) Above a critical filament density, small polar nematic clusters start to form. (d) Persistent density fluctuations lead to the formation of wave-like structures. (e) Collisions of different patterns lead to the formation of spirals. The swirling motion is visualized in a time overlay of ten consecutive images over 1.17 s, starting from the image depicted in the inset. Scale bars denote 50 µm.

Reconstituted actin networks are not only well-suited to study cellular processes but can furthermore act as an interesting model system for other physical objectives, for instance self-organizing processes. A remarkable example is the spontaneous emergence of collective motion from a disordered phase in active systems, like flocks of animals or self-propelled microorganisms [179, 180]. Similarities between these systems, such as the inherent polarity of the constituents, a density-dependent transition to ordered phases or the existence of very large density fluctuations suggest universal principles that underly the pattern formation. However, the complexity of interactions or the limited experimental control of the system parameters are often major obstacles in the understanding of the basic self-organization principles.

Actin networks provide a model system depending on only a few key parameters that can be adjusted independently (the filament length, density or the ambient salt concentration). The addition of molecular motors provides an active component to the system. Moreover, the molecular nature of this approach permits large system sizes. An interesting experiment for studying self-organization principles is the motility assay described in the following. Here, collective phenomena emerge at high densities of filament. To perform this experiment, HMM molecules are immobilized on a cover slip

(fig. 7.1(a)). Under consumption of ATP, actin filaments are driven over the surface by the power strokes of the motors. Their motion is visualized by a small fraction of fluorescently labeled filaments. For low actin concentration, a disordered phase is found, where the individual filaments perform persistent random walks without any specific preferences (fig. 7.1(b)). However, domains of collective motion appear above a critical concentration of about 5 filaments per square micrometer. Several different patterns occur, as illustrated in fig. 7.1(c)-(e): in an intermediate regime, small polar nematic clusters of coherently moving filaments start to form. The cluster size of these structures ranges from 20 to 500 µm in diameter. They exhibit an erratic motion with frequent directional reorientation. A further increase in filament density leads to wave-like structures where the filaments move predominantly in bands that are stable throughout the observation time. Filaments outside these bands perform persistent random walks. Beside the small clusters and wave-band structures, spirals of actin filaments can be observed which form spontaneously by collision of different patterns.

A detailed theoretical description of such phenomena in active fluids is still missing. The questions how order can emerge spontaneously from a disordered phase or what kind of interactions determine the pattern formation have been addressed by several theoretical approaches [181–183]. However, up to now, the common underlying principles could not be identified, arguably because an adequate model system is still missing. The high density motility assay described above provides at the first time a model system allowing for a direct comparison of theory and experiment [184, 185].

Appendix A

Calculation of *R**

An important control parameter for *in vitro* actin networks is the molar ration R between crosslinking molecules and actin subunits. Sometimes, it is more meaningful to consider the relative concentration of actually bound ABPs, R^*, regarding the equilibrium dissociation constant K_d. This can be derived by a simple model of bimolecular reaction between the actin molecule A and the ABP B:

$$A + B \rightleftharpoons AB \tag{A.1}$$

With the dissociation constant K_D this results in the law of mass action

$$K_D \;=\; \frac{c_A \cdot c_B}{c_{AB}} \tag{A.2}$$

where c denotes the respective concentration. The total actin concentration c_A^{tot} and the total ABP concentration c_B^{tot} are given by

$$c_A^{\mathrm{tot}} \;=\; c_A + c_{AB} \tag{A.3}$$

and

$$c_B^{\mathrm{tot}} \;=\; c_B + c_{AB} \tag{A.4}$$

The actin and ABP concentrations in (A.2) can be substituted with the expressions obtained by (A.3) and (A.4). In combination with the molar ratio of the ABP to actin, $R \;=\; \frac{c_B^{\mathrm{tot}}}{c_A^{\mathrm{tot}}}$, and the number of bound ABPs per G-actin molecule, $R^* \;=\; \frac{c_{AB}}{c_A^{\mathrm{tot}}}$, this leads to

$$R^{*2} + R^* \cdot \left(-1 - R - \frac{K}{c_A^{\mathrm{tot}}}\right) + R \;=\; 0 \tag{A.5}$$

Solving (A.5) and choosing the physical meaningful solution results in an expression for the molar ratio $R*$ of bound ABPs to actin:

$$R^* \;=\; \frac{1}{2}\left(\left(1 + R + \frac{K}{c_A^{\mathrm{tot}}}\right) - \sqrt{\left(1 + R + \frac{K}{c_A^{\mathrm{tot}}}\right)^2 - 4 \cdot R}\right) \tag{A.6}$$

This is plotted for various actin concentrations in fig. A.1. Deviations become most pronounced for low actin concentration and high R values. Therefore, the calculation of R^* is necessary if comparing measurements at different c_A or K_D values. Unfortunately, K_D is not known for all proteins used in this thesis. In this case, a description in R is used.

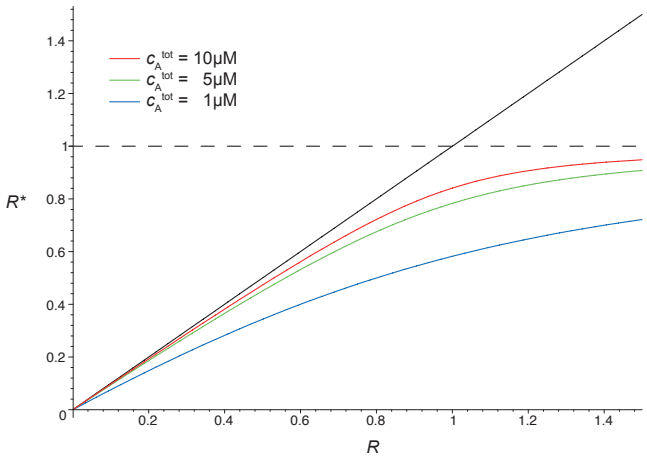

Figure A.1: The relative crosslinkerconcentration R^* corrected by K_d in dependence of the relative crosslinker concnetration R for different actin concentrations $c_\mathrm{A}^\mathrm{tot}$. K_d is chosen to be 0.3 µM as it is for fascin [42].

Appendix B

Pull Down Assay with Actin Bundles

The pull-down assay is a centrifugation method to elucidate *in vitro* interactions between macromolecules. They cannot only confirm the existence of a protein-protein interaction but also can give insights into the kinetics of this process. In the case of actin networks, one can get informations about the dissociation constant K_D of ABPs analyzing the concentrations of the protein in the pellet and the supernatant. Moreover, it offers an opportunity to measure the critical actin concentration c_{crit} in the presence of various crosslinking proteins which remains unpolymerized and thus suspended in the supernatant. If the ABPs change the effective polymerization/depolymerization rates of actin, this is also expected to influence $c_{crit} = k_{off}/k_{on}$.

For this purpose, actin networks in the presence of various bundling proteins are prepared in a centrifugation tube. After full polymerization, they are centrifuged at 435 400 g for 1.5 h. Fig. B.1 (a) shows a silver stained SDS-gel from the supernatants for various crosslinkers at $R = 1$ and $R = 0.1$ respectively. As can easily be seen, filamin and α-actinin increase the actin concentration in the supernatant; fascin and HMM do not seem to have any effect, or at least considerably less pronounced and not detectable with this method.

The increase of actin in the supernatant could be caused by the binding of filamin to G-actin monomers. At such a high molar ratio of $R = 1$ not every filamin molecule can bind to the actin network. The unsaturated filamin might bind actin monomers and thus increase the actin concentration in the solution. To test this hypothesis, the assay was done with varying amount of filamin and with actin and filamin in G-buffer (fig. B.1(b) and (c)). Surprisingly, the actin concentration is drastically increased even at very low filamin concentration. In contrast, filamin has only slight effect on unpolymerized actin. Therefore, it seems improbable that the increase is caused by unsaturated filamin catching actin monomers. This is supported by the fact that after centrifugation the supernatant polymerizes again into a homogenous filamin bundle network (fig. B.1(d)). If the bundles had existed already right after centrifugation, they would have form clusters rather than a homogenous network due to their non-equilibrium nature.

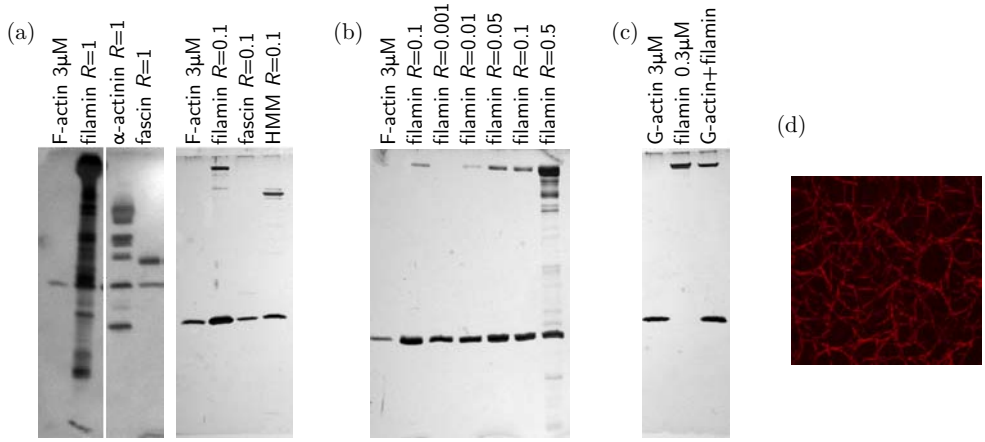

Figure B.1: Centrifugation assay with actin bundles. (a)-(c): Silver-stained SDS-Gels of the supernatants after centrifugation at 435 400 g for 1.5 h. (a) At high crosslinker ratio ($R = 1$), filamin and α-actinin significantly increase the actin concentration in the supernatant while fascin seems to have no effect. Similarly, at $R = 0.1$ filamin increases the actin concentration while fascin and also HMM does not change it considerably. (b) The concentration series of filamin reveals that even minimal amounts of filamin change the actin concentration significantly. (c) This increase does not seem to be caused by filamin catching actin monomers and thus increasing the critical concentration. Approximately the same actin concentration is measured in G-buffer with or without filamin. (d) Confocal micrograph of the supernatant approximatley 1 h after centrifugation at 100 000 g for 1.5 h. A homogenous network of filamin bundles originates indicating that the actin was in monomeric form after the centrifugation. Furthermore it supports the assumption that the actin in the supernatant is not equal to c_{crit}.

Appendix C

Model of Depolymerization

The model assumes a given distribution of filament lengths $V(x)$ where each filament depolymerizes with a constant rate k. Breaking of filaments is neglected. The important variables can be found in the following table:

x	...	filament length at time $t = 0$
$V(x)$	...	distribution of filament lengths
$G(x) = \int V(x)\mathrm{d}x$	...	antiderivatice of $V(x)$
k	...	rate of depolymerization
$x(t) = kt$	...	depolymerization length at time $t = 0$, independent of x
$L(x,t) = x - x(t)$	...	filament length at time t
x_c	...	cut-off length in microscope analysis
$P(t)$	...	measured signal in pyrene assay
$M(t)$	...	measured quantity in microscopy based analysis

Pyrene assay

In the pyrene assay, one measures the total length of actin polymerized in the sample, i.e. the signal in the pyrene assay $P(t)$ resembles the time course of total length of actin in the sample. This can be calculated as the integral over the length distribution times the actual length at time t:

$$\begin{aligned} P(t) &= \int_{x(t)}^{\infty} (x - x(t))V(x)\mathrm{d}x \\ &= [xG(x)]_{x(t)}^{\infty} - \int_{x(t)}^{\infty} G(x)\mathrm{d}x - x(t)[G(x)]_{x(t)}^{\infty} \end{aligned}$$

Assuming $\lim_{x\to\infty} xG(x) = 0$, this can be simplified to:

$$\begin{aligned} P(t) &= -x(t)G(x(t)) - \int_{x(t)}^{\infty} G(x)\mathrm{d}x - (-x(t)G(x(t))) \\ &= -\int_{x(t)}^{\infty} G(x)\mathrm{d}x \end{aligned} \tag{C.1}$$

Microscopy based analysis

This model assumes that the analysis based on fluorescence images of the filaments also counts the total length of polymerized actin, but disregards filaments/oligomers

below a critical cut-off length x_c. Thus, the integration starts at $x(t)+x_c$, the integrand remains the same. The influence of the 2d-projection of the filaments which will change the length distribution is neglected.

$$\begin{aligned} M(t) &= \int_{x(t)+x_c}^{\infty} (x - x(t))V(x)\mathrm{d}x \\ &= [xG(x)]_{x(t)+x_c}^{\infty} - \int_{x(t)+x_c}^{\infty} G(x)\mathrm{d}x - x(t)[G(x)]_{x(t)+x_c}^{\infty} \\ &= -(x(t)+x_c)G(x(t)+x_c) - \int_{x(t)+x_c}^{\infty} G(x)\mathrm{d}x - [-x(t)G(x(t)+x_c)] \\ &= -x_cG(x(t)+x_c) - \int_{x(t)+x_c}^{\infty} G(x)\mathrm{d}x \end{aligned} \tag{C.2}$$

Example 1: Exponential length distribution

$$V(x) = \mathrm{e}^{-ax} \Rightarrow G(x) = -\frac{1}{a}\mathrm{e}^{-ax} \Rightarrow \int G(x)\mathrm{d}x = \frac{1}{a^2}\mathrm{e}^{-ax}$$

The pyrene signal can then be calculated using (C.1):

$$\begin{aligned} P(t) &= -\left[\frac{1}{a^2}\mathrm{e}^{-ax}\right]_{x(t)}^{\infty} \\ &= -\left(-\frac{1}{a^2}\mathrm{e}^{-akt}\right) \\ &= \frac{1}{a^2}\mathrm{e}^{-akt} \end{aligned}$$

The microscopy-based signal $M(t)$ results from equation (C.2):

$$\begin{aligned} M(t) &= \frac{x_c}{a}\mathrm{e}^{-a(x(t)+x_c)} - \left[\frac{1}{a^2}\mathrm{e}^{-ax}\right]_{x(t)+x_c}^{\infty} \\ &= \frac{x_c}{a}\mathrm{e}^{-a(x(t)+x_c)} - \frac{1}{a^2}\mathrm{e}^{-a(x(t)+x_c)} \\ &= (ax_c+1)\mathrm{e}^{-ax_c}\frac{1}{a^2}\mathrm{e}^{-akt} \\ &= (ax_c+1)\mathrm{e}^{-ax_c}P(t) \end{aligned}$$

Thus, the microscopy signal follows the same exponential decay as the pyrene assay; the different prefactor would drop out by normalizing the signal by the initial value.

Example 2: Double-exponential length distribution

$$V(x) = A\mathrm{e}^{-ax} + B\mathrm{e}^{-bx} \Rightarrow G(x) = -\frac{A}{a}\mathrm{e}{-ax} - \frac{B}{b}\mathrm{e}^{-bx} \Rightarrow \int G(x) = \frac{A}{a^2}\mathrm{e}^{-ax} + \frac{B}{b^2}\mathrm{e}^{-bx}$$

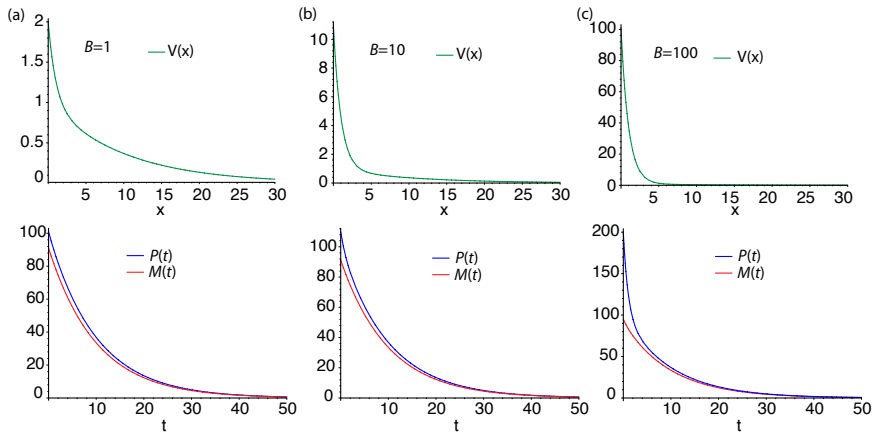

Figure C.1: Length distribution $V(x)$ and pyrene and microcopy signal $P(t)$ and $M(t)$ for the numeric example with different values for B. (a) $B = 1$, (b) $B = 10$, (c) $B = 100$.

$$
\begin{aligned}
P(t) &= -\left[\frac{A}{a^2}\mathrm{e}^{-ax} + \frac{B}{b^2}\mathrm{e}^{-bx}\right]_{x(t)}^{\infty} \\
&= \frac{A}{a^2}\mathrm{e}^{-akt} + \frac{B}{b^2}\mathrm{e}^{-bkt} \\
M(t) &= -x_c\left(-\frac{A}{a}\mathrm{e}^{-a(x(t)+x_c)} - \frac{B}{b}\mathrm{e}^{-b(x(t)+x_c)}\right) + \left(\frac{A}{a^2}\mathrm{e}^{-a(x(t)+x_c)} + \frac{B}{b^2}\mathrm{e}^{-b(x(t)+x_c)}\right) \\
&= (ax_c+1)\mathrm{e}^{-ax_c}\frac{A}{a^2}\mathrm{e}^{-akt} + (bx_c+1)\mathrm{e}^{-bx_c}\frac{B}{b^2}\mathrm{e}^{-bkt}
\end{aligned}
$$

Due to the prefactor A/a^2 (and B/b^2 respectively), the length distribution with shorter decay length and thus larger a (or b respectively) is weighted less than the other distribution. In order to produce a significant effect in the pyrene signal, the prefactor A (or B) of this distribution has to be significantly larger.

Numeric example: Given the following values for the model parameters:

$$
\begin{aligned}
A &= 1 \\
a &= 0.1 \\
k &= 1 \\
B &= 1 \text{ and } 10 \text{ and } 100 \\
b &= 1 \\
x_c &= 5
\end{aligned}
$$

The calculated time courses of $P(t)$ and $M(t)$ for three different double-exponential length distributions are shown in Fig. C.1.

This illustrates that only for $B \gg A$, the mass fraction of the shorter filament distribution carries significant weight in such a way that the double-exponential length

distribution appears in the pyrene signal. In this case, there is a significant difference between $P(t)$ and $M(t)$: While the pyrene assay is sensitive to the large fraction of short filaments, the microscopy based analysis neglects them at all and thus follows only the long distribution.

Bibliography

[1] J. R. Bartles, 2000. Parallel actin bundles and their multiple actin-bundling proteins. *Curr Opin Cell Biol*, 12(1):72–78.

[2] L. Tilney, P. Connelly, K. Vranich, M. Shaw, and G. Guild, 2000. Regulation of actin filament cross-linking and bundle shape in Drosophila bristles. *J Cell Biol*, 148(1):87–99.

[3] G. Guild, P. Connelly, L. Ruggiero, K. Vranich, and L. Tilney, 2005. Actin filament bundles in Drosophila wing hairs: Hairs and bristles use different strategies for assembly. *Mol Biol Cell*, 16(8):3620–3631.

[4] K. Cant, B. Knowles, M. Mooseker, and L. Cooley, 1994. Drosophila Singed, a Fascin Homolog, Is Required for Actin Bundle Formation during Oogenesis and Bristle Extension. *J Cell Biol*, 125(2):369–380.

[5] L. Zheng, G. Sekerkova, K. Vranich, L. Tilney, E. Mugnaini, and J. Bartles, 2000. The deaf jerker mouse has a mutation in the gene encoding the espin actin-bundling proteins of hair cell stereocilia and lacks espins. *Cell*, 102(3):377–385.

[6] P. Fernandez and A. Ott, 2008. Single cell mechanics: Stress stiffening and kinematic hardening. *Phys Rev Lett*, 100(23):238102.

[7] M. Gardel, F. Nakamura, J. H. Hartwig, J. C. Crocker, T. P. Stossel, and D. Weitz, 2006. Prestressed F-actin networks cross-linked by hinged filamins replicate mechanical properties of cells. *Proc Natl Acad Sci USA*, 103(6):1762–1767.

[8] A. R. Bausch and K. Kroy, 2006. A bottom-up approach to cell mechanics. *Nat Phys*, 2(4):231–238.

[9] J. X. Tang and P. A. Janmey, 1996. The polyelectrolyte nature of F-actin and the mechanism of actin bundle formation. *J Biol Chem*, 271(15):8556–8563.

[10] W. Kabsch, H. Mannherz, D. Suck, E. Pai, and K. C. Holmes, 1990. Atomic structure of the actin:DNase I complex. *Nature*, 347(6288):37–44.

[11] K. C. Holmes, D. Popp, W. Gebhard, and W. Kabsch, 1990. Atomic model of the actin filament. *Nature*, 347(6288):44–49.

[12] T. Oda, M. Iwasa, T. Aihara, Y. Maeda, and A. Narita, 2009. The nature of the globular-to fibrous-actin transition. *Nature*, 457(7228):441–445.

[13] K. C. Holmes, I. Angert, F. J. Kull, W. Jahn, and R. R. Schröder, 2003. Electron cryo-microscopy shows how strong binding of myosin to actin releases nucleotide. *Nature*, 425(6956):423–427.

[14] L. Otterbein, P. Graceffa, and R. Dominguez, 2001. The crystal structure of uncomplexed actin in the ADP state. *Science*, 293(5530):708–711.

[15] H. A. al Khayat, N. Yagi, and J. M. Squire, 1995. Structural changes in actin-tropomyosin during muscle regulation: computer modelling of low-angle X-ray diffraction data. *J Mol Biol*, 252(5):611–632.

[16] T. D. Pollard, 1986. Rate constants for the reactions of ATP- and ADP-actin with the ends of actin filaments. *J Cell Biol*, 103(6 Pt 2):2747–2754.

[17] J. Howard, 2001. *Mechanics of motor proteins and the cytoskeleton*. Sinauer Associates.

[18] A. Wegner, 1976. Head to Tail Polymerization of Actin. *J Mol Biol*, 108(1):139–150.

[19] C. G. dos Remedios, D. Chhabra, M. Kekic, I. V. Dedova, M. Tsubakihara, D. A. Berry, and N. J. Nosworthy, 2003. Actin binding proteins: regulation of cytoskeletal microfilaments. *Physiol Rev*, 83(2):433–473.

[20] N. Kureishy, V. Sapountzi, S. Prag, N. Anilkumar, and J. Adams, 2002. Fascins, and their roles in cell structure and function. *Bioessays*, 24(4):350–361.

[21] D. Vignjevic, D. Yarar, M. Welch, J. Peloquin, T. Svitkina, and G. Borisy, 2003. Formation of filopodia-like bundles in vitro from a dendritic network. *J Cell Biol*, 160(6):951–962.

[22] O. Lieleg, M. M. A. E. Claessens, C. Heussinger, E. Frey, and A. R. Bausch, 2007. Mechanics of bundled semiflexible polymer networks. *Phys Rev Lett*, 99(8):088102.

[23] J. Bartles, L. Zheng, A. Li, A. Wierda, and B. Chen, 1998. Small espin: A third actin-bundling protein and potential forked protein ortholog in brush border microvilli. *J Cell Biol*, 143(1):107–119.

[24] T. Stossel, J. Condeelis, L. Cooley, J. Hartwig, A. Noegel, M. Schleicher, and S. Shapiro, 2001. Filamins as integrators of cell mechanics and signalling. *Nat Rev Mol Cell Biol*, 2(2):138–145.

[25] Y. Tseng, K. M. An, O. Esue, and D. Wirtz, 2004. The bimodal role of filamin in controlling the architecture and mechanics of F-actin networks. *J Biol Chem*, 279(3):1819–1826.

[26] K. M. Schmoller, O. Lieleg, and A. R. Bausch, 2008. Internal stress in kinetically trapped actin bundle networks. *Soft Matter*, 4(12):2365–2367.

[27] O. Lieleg, K. M. Schmoller, C. J. Cyron, Y. Luan, W. A. Wall, and A. R. Bausch, 2009. Structural polymorphism in heterogeneous cytoskeletal networks. *Soft Matter*, 5(9):1796–1803.

[28] S. Lowey, H. Slayter, A. Weeds, and H. Baker, 1969. Substructure of the Myosin Molecule I. Subfragments of Myosin by Enzymic Degradation. *J Mol Biol*, 42(1):1–29.

[29] R. Tharmann, M. M. A. E. Claessens, and A. R. Bausch, 2007. Viscoelasticity of isotropically cross-linked actin networks. *Phys Rev Lett*, 98(8):088103.

[30] A. Wegner, 1979. Equilibrium of the Actin-Tropomyosin Interaction. *J Mol Biol*, 131(4):839–853.

[31] W. Morton, K. Ayscough, and P. McLaughlin, 2000. Latrunculin alters the actin-monomer subunit interface to prevent polymerization. *Nat Cell Biol*, 2(6):376–378.

[32] H. Sun, M. Yamamoto, M. Mejillano, and H. Yin, 1999. Gelsolin, a multifunctional actin regulatory protein. *J Biol Chem*, 274(47):33179–33182.

[33] P. A. Janmey, J. Peetermans, K. Zaner, T. P. Stossel, and T. Tanaka, 1986. Structure and Mobility of Actin Filaments as Measured by Quasielastic Light Scattering, Viscometry, and Electron Microscopy. *J Biol Chem*, 261(18):8357–8362.

[34] J. R. Bamburg, 1999. Proteins of the ADF/Cofilin Family: Essential Regulators of actin dynamics. *Annu Rev Cell Dev Biol*, 15:185–230.

[35] M. Carlier, V. Laurent, J. Santolini, R. Melki, D. Didry, G. Xia, Y. Hong, N. Chua, and D. Pantaloni, 1997. Actin depolymerizing factor (ADF/cofilin) enhances the rate of filament turnover: Implication in actin-based motility. *J Cell Biol*, 136(6):1307–1322.

[36] A. McGough, B. Pope, W. Chiu, and A. Weeds, 1997. Cofilin changes the twist of F-actin: implications for actin filament dynamics and cellular function. *J Cell Biol*, 138(4):771–781.

[37] E. M. De La Cruz, 2009. How cofilin severs an actin filament. *Biophys Rev*, 1(2):51–59.

[38] M. Oser and J. Condeelis, 2009. The Cofilin Activity Cycle in Lamellipodia and Invadopodia. *J Cell Biochem*, 108(6):1252–1262.

[39] J. A. Spudich and S. Watt, 1971. The regulation of rabbit skeletal muscle contraction. I. Biochemical studies of the interaction of the tropomyosin-troponin complex with actin and the proteolytic fragments of myosin. *J Biol Chem*, 246(15):4866–4871.

[40] T. Kouyama and K. Mihashi, 1981. Fluorimetry study of N-(1-pyrenyl)iodoacetamide-labelled F-actin. Local structural change of actin protomer both on polymerization and on binding of heavy meromyosin. *Eur J Biochem*, 114(1):33–38.

[41] J. Cooper, S. Walker, and T. Pollard, 1983. Pyrene actin: documentation of the validity of a sensitive assay for actin polymerization. *J Muscle Res Cell Motil*, 4(2):253–262.

[42] S. Ono, Y. Yamakita, S. Yamashiro, P. Matsudaira, J. Gnarra, T. Obinata, and F. Matsumura, 1997. Identification of an actin binding region and a protein kinase C phosphorylation site on human fascin. *J Biol Chem*, 272(4):2527–2533.

[43] K. R. Purdy, J. R. Bartles, and G. C. L. Wong, 2007. Structural polymorphism of the actin-espin system: A prototypical system of filaments and linkers in stereocilia. *Phys Rev Lett*, 98(5):058105.

[44] Y. Shizuta, H. Shizuta, M. Gallo, P. Davies, I. Pastan, and M. Lewis, 1976. Purification and Properties of Filamin, an Actin Binding Protein from Chicken Gizzard. *J Biol Chem*, 251(21):6562–6567.

[45] S. Craig, C. Lancashire, and J. Cooper, 1982. Preparation of smooth muscle α-actinin. *Method Enzymol*, 85:316–321.

[46] J. Uhde, M. Keller, E. Sackmann, A. Parmeggiani, and E. Frey, 2004. Internal motility in stiffening actin-myosin networks. *Phys Rev Lett*, 93(26):268101.

[47] E. Eisenberg and W. W. Kielley, 1974. Troponin-tropomyosin complex: Column chromatographic separation and activity of the three, active troponin components with and without tropomyosin present. *J Biol Chem*, 249(15):4742–4748.

[48] H. Kurokawa, W. Fujii, K. Ohmi, T. Sakurai, and Y. Nonomura, 1990. Simple and rapid purification of brevin. *Biochem Bioph Res Co*, 168(2):451–457.

[49] C. R. Cantor and P. R. Schimmel, 1980. *Techniques for the study of biological structure and function PartII: Techniques for the study of biological structure and function*. W.H. Freeman and company, new york edition.

[50] B. K. Vajnštejn, 1966. *Diffraction of X-rays by chain molecules*. Elsevier Publishing Company, Amsterdam - London - New York.

[51] R. Franklin and R. Gosling, 1953. Molecular configuration in sodium thymonucleate. *Nature*, 171(4356):740–741.

[52] R. Crowther, D. J. DeRosier, and A. Klug, 1970. The reconstruction of a three-dimensional structure from projections and its application to electron microscopy. *Proc R Soc Lon Ser-A*, 317(1530):319–340.

[53] R. Millane and W. Stroud, 1991. Effects of disorder on fibre diffraction patterns. *Int J Biol Macromol*, 13(3):202–208.

[54] W. Stroud and R. Millane, 1995. Diffraction by disordered polycrystalline fibres. *Acta Crystallogr A*, 51:771–790.

[55] K. Kopitzki and P. Herzog, 2007. *Einführung in die Festkörperphysik*. Teubner Verlag.

[56] A. Guinier, 1955. *Small-angle scattering of X-rays*. Wiley, new york edition.

[57] G. Stubbs, 1974. The Effect of Disorientation on Intensity Distribution of Non-crystalline Fibers. II. Applications. *Acta Crystallogr A*, 30:639–645.

[58] C. Sukow and D. J. DeRosier, 2003. Order, disorder, and perturbations in actin-aldolase rafts. *Biophys J*, 85(1):525–536.

[59] H. D. Deas, 1952. The Diffraction of X-rays by a Random Assemblage of Molecules Having Partial Alignment. *Acta Crystallogr*, 5(4):542–546.

[60] K. C. Holmes and J. Leigh, 1974. The Effect of Disorientation on the Intensity Distribution of Non-crystalline Fibres. I. Theory. *Acta Crystallogr A*, 30:635–638.

[61] T. T. Tibbitts and D. L. D. Caspar, 1993. Deconvolution of Disoriented Fiber Diffraction Data using Iterative Convolution and Local Regression. *Acta Crystallogr A*, 49:532–545.

[62] J. Torbet and M. Dickens, 1984. Orientation of skeletal muscle actin in strong magnetic fields. *FEBS Lett*, 173(2):403–406.

[63] M. M. A. E. Claessens, M. Bathe, E. Frey, and A. R. Bausch, 2006. Actin-binding proteins sensitively mediate F-actin bundle stiffness. *Nat Mat*, 5(9):748–753.

[64] L. Tilney, P. Connelly, K. Vranich, M. Shaw, and G. Guild, 1998. Why are two different cross-linkers necessary for actin bundle formation in vivo and what does each cross-link contribute? *J Cell Biol*, 143(1):121–133.

[65] E. Karsenti, 2008. Self-organization in cell biology: a brief history. *Nat Rev Mol Cell Biol*, 9(3):255–262.

[66] M. Hosek and J. Tang, 2004. Polymer-induced bundling of F actin and the depletion force. *Phys Rev E*, 69(5):051907.

[67] T. E. Angelini, H. Liang, W. Wriggers, and G. C. L. Wong, 2003. Like-charge attraction between polyelectrolytes induced by counterion charge density waves. *Proc Natl Acad Sci USA*, 100(15):8634–8637.

[68] D. Needleman, M. Ojeda-Lopez, U. Raviv, H. Miller, L. Wilson, and C. R. Safinya, 2004. Higher-order assembly of microtubules by counterions: From hexagonal bundles to living necklaces. *Proc Natl Acad Sci USA*, 101(46):16099–16103.

[69] C. Conwell, I. Vilfan, and N. Hud, 2003. Controlling the size of nanoscale toroidal DNA condensates with static curvature and ionic strength. *Proc Natl Acad Sci USA*, 100(16):9296–9301.

[70] P. Segre, V. Prasad, A. Schofield, and D. Weitz, 2001. Glasslike kinetic arrest at the colloidal-gelation transition. *Phys Rev Lett*, 86(26):6042–6045.

[71] A. Stradner, H. Sedgwick, F. Cardinaux, W. Poon, S. Egelhaaf, and P. Schurtenberger, 2004. Equilibrium cluster formation in concentrated protein solutions and colloids. *Nature*, 432(7016):492–495.

[72] M. Henle and P. Pincus, 2005. Equilibrium bundle size of rodlike polyelectrolytes with counterion-induced attractive interactions. *Phys Rev E*, 71(6):060801.

[73] G. M. Grason and R. F. Bruinsma, 2007. Chirality and equilibrium biopolymer bundles. *Phys Rev Lett*, 99(9):098101.

[74] T. Ikawa, F. Hoshino, O. Watanabe, Y. Li, P. Pincus, and C. R. Safinya, 2007. Molecular scale imaging of F-actin assemblies immobilized on a photopolymer surface. *Phys Rev Lett*, 98(1):018101.

[75] T. Huang, H. Toraya, T. Blanton, and Y. Wu, 1993. X-ray powder diffraction analysis of silver behenate, a possible low-angle diffraction standard. *J Appl Crystallogr*, 26(2):180–184.

[76] M. M. A. E. Claessens, R. Tharmann, K. Kroy, and A. Bausch, 2006. Microstructure and viscoelasticity of confined serniflexible polymer networks. *Nat Phys*, 2(3):186–189.

[77] D. J. DeRosier and R. Censullo, 1981. Structure of F-actin Needles from Extracts of Sea Urchin Oocytes. *J Mol Biol*, 146(1):77–99.

[78] J. Bryan and R. Kane, 1978. Separation and Interaction of the Major Components of Sea Urchin Actin Gel. *J Mol Biol*, 125(2):207–224.

[79] B. Ha and A. Liu, 1999. Kinetics of bundle growth in DNA condensation. *Europhys Lett*, 46(5):624–630.

[80] J. Kierfeld, O. Niamploy, V. Sa-Yakanit, and R. Lipowsky, 2004. Stretching of semiflexible polymers with elastic bonds. *Eur Phys J E Soft Matter*, 14(1):17–34.

[81] L. Haviv, N. Gov, Y. Ideses, and A. Bernheim-Groswasser, 2008. Thickness distribution of actin bundles in vitro. *Eur Biophys J*, 37(4):447–454.

[82] J. Groenewold and W. Kegel, 2001. Anomalously large equilibrium clusters of colloids. *J Phys Chem B*, 105(47):11702–11709.

[83] T. Svitkina, E. Bulanova, O. Chaga, D. Vignjevic, S. Kojima, J. Vasiliev, and G. Borisy, 2003. Mechanism of filopodia initiation by reorganization of a dendritic network. *J Cell Biol*, 160(3):409–421.

[84] A. Thess, R. Lee, P. Nikolaev, H. Dai, P. Petit, J. Robert, C. Xu, Y. Lee, S. Kim, A. Rinzler, D. Colbert, G. Scuseria, D. Tomanek, J. Fischer, and R. Smalley, 1996. Crystalline Ropes of Metallic Carbon Nanotubes. *Science*, 273(5274):483–487.

[85] L. Tilney, D. J. DeRosier, and M. MULROY, 1980. The Organization of Actin Filaments in the Stereocilia of Cochlear Hair Cells. *J Cell Biol*, 86(1):244–259.

[86] D. J. DeRosier, E. Mandelkow, A. Silliman, L. Tilney, and R. Kane, 1977. Structure of Actin-containing Filaments from Two Types of Non-muscle Cells. *J Mol Biol*, 113(4):679–695.

[87] V. E. Galkin, A. Orlova, G. F. Schroeder, and E. H. Egelman, 2010. Structural polymorphism in F-actin. *Nat Struct Mol Biol*, 17(11):1318–1324.

[88] E. Reisler and E. H. Egelman, 2007. Actin structure and function: What we still do not understand. *J Biol Chem*, 282(50):36133–36137.

[89] Y. Tsuda, H. Yasutake, A. Ishijima, and T. Yanagida, 1996. Torsional rigidity of single actin filaments and actin-actin bond breaking force under torsion measured directly by in vitro micromanipulation. *Proc Natl Acad Sci USA*, 93(23):12937–12942.

[90] D. J. DeRosier and L. Tilney, 1981. How Actin-Filaments Pack Into Bundles. *Cold Spring Harb Sym*, 46:525–540.

[91] G. H. Lai, R. Coridan, O. V. Zribi, R. Golestanian, and G. C. L. Wong, 2007. Evolution of growth modes for polyelectrolyte bundles. *Phys Rev Lett*, 98(18):187802.

[92] O. Lieleg, M. M. A. E. Claessens, and A. R. Bausch, 2010. Structure and dynamics of cross-linked actin networks. *Soft Matter*, 6(2):218–225.

[93] H. Shin, K. R. P. Drew, J. R. Bartles, G. C. L. Wong, and G. M. Grason, 2009. Cooperativity and Frustration in Protein-Mediated Parallel Actin Bundles. *Phys Rev Lett*, 103(23):238102.

[94] H. Shin and G. M. Grason, 2010. Structural reorganization of parallel actin bundles by crosslinking proteins: Incommensurate states of twist. *Phys Rev E*, 82(5):051919.

[95] G. M. Grason, 2009. Braided bundles and compact coils: The structure and thermodynamics of hexagonally packed chiral filament assemblies. *Phys Rev E*, 79(4):041919.

[96] M. Turner, R. Briehl, F. Ferrone, and R. Josephs, 2003. Twisted protein aggregates and disease: The stability of sickle hemoglobin fibers. *Phys Rev Lett*, 90(12):128103.

[97] J. W. Weisel, C. Nagaswami, and L. Makowski, 1987. Twisting of fibrin fibers limits their radial growth. *Proc Natl Acad Sci USA*, 84(24):8991–8995.

[98] L. Limozin and E. Sackmann, 2002. Polymorphism of cross-linked actin networks in giant vesicles. *Phys Rev Lett*, 89(16):168103.

[99] O. Pelletier, E. Pokidysheva, L. S. Hirst, N. Bouxsein, Y. Li, and C. R. Safinya, 2003. Structure of actin cross-linked with α-actinin: a network of bundles. *Phys Rev Lett*, 91(14):148102.

[100] T. E. Angelini, 2005. *Counterion Behavior in Biopolymers*. Dissertation.

[101] K. M. Schmoller, O. Lieleg, and A. R. Bausch, 2008. Cross-linking molecules modify composite actin networks independently. *Phys Rev Lett*, 101(11):118102.

[102] T. J. Mitchison and M. Kirschner, 1984. Dynamic instability of microtubule growth. *Nature*, 312(5991):237–242.

[103] R. Margolis and L. Wilson, 1998. Microtubule treadmilling: what goes around comes around. *Bioessays*, 20(10):830–836.

[104] S. Shaw, R. Kamyar, and D. Ehrhardt, 2003. Sustained microtubule treadmilling in Arabidopsis cortical arrays. *Science*, 300(5626):1715–1718.

[105] J. Howard and A. Hyman, 2003. Dynamics and mechanics of the microtubule plus end. *Nature*, 422(6933):753–758.

[106] T. P. Stossel, 1993. On the Crawling of Animal Cells. *Science*, 260(5111):1086–1094.

[107] M. Welch, A. Mallavarapu, J. Rosenblatt, and T. J. Mitchison, 1997. Actin dynamics in vivo. *Curr Opin Cell Biol*, 9(1):54–61.

[108] N. Watanabe and T. J. Mitchison, 2002. Single-molecule speckle analysis of Aactin filament turnover in lamellipodia. *Science*, 295(5557):1083–1086.

[109] H. Wendel and P. Dancker, 1986. Kinetics of actin depolymerization: influence of ions, temperature, age of F-actin, cytochalasin B and phalloidin. *Biochim Biophys Acta*, 873(3):387–396.

[110] E. Korn, M. Carlier, and D. Pantaloni, 1987. Actin Polymerization and ATP Hydrolysis. *Science*, 238(4827):638–644.

[111] J. Kuhn and T. Pollard, 2005. Real-time measurements of actin filament polymerization by total internal reflection fluorescence microscopy. *Biophys J*, 88(2):1387–1402.

[112] I. Fujiwara, D. Vavylonis, and T. D. Pollard, 2007. Polymerization kinetics of ADP- and ADP-P-i-actin determined by fluorescence microscopy. *Proc Natl Acad Sci USA*, 104(21):8827–8832.

[113] H. Y. Kueh, W. M. Brieher, and T. J. Mitchison, 2008. Dynamic stabilization of actin filaments. *Proc Natl Acad Sci USA*, 105(43):16531–16536.

[114] X. Li, J. Kierfeld, and R. Lipowsky, 2009. Actin Polymerization and Depolymerization Coupled to Cooperative Hydrolysis. *Phys Rev Lett*, 103(4):048102.

[115] H. Y. Kueh and T. J. Mitchison, 2009. Structural Plasticity in Actin and Tubulin Polymer Dynamics. *Science*, 325(5943):960–963.

[116] R. Mullins, J. Heuser, and T. Pollard, 1998. The interaction of Arp2/3 complex with actin: Nucleation, high affinity pointed end capping, and formation of branching networks of filaments. *Proc Natl Acad Sci USA*, 95(11):6181–6186.

[117] M. Carlier, 1998. Control of actin dynamics. *Curr Opin Cell Biol*, 10(1):45–51.

[118] S. Zigmond, R. Furukawa, and M. Fechheimer, 1992. Inhibition of Actin Filament Depolymerization by the Dictyostelium 30,000-D Actin-bundling Protein. *J Cell Biol*, 119(3):559–567.

[119] M. Cano, L. Cassimeris, M. Fechheimer, and S. Zigmond, 1992. Mechanisms Responsible for F-actin Stabilization after Lysis of Polymorphonuclear Leukocytes. *J Cell Biol*, 116(5):1123–1134.

[120] P. Loomis, L. Zheng, G. Sekerkova, B. Changyaleket, E. Mugnaini, and J. Bartles, 2003. Espin cross-links cause the elongation of microvillus-type parallel actin bundles in vivo. *J Cell Biol*, 163(5):1045–1055.

[121] M. Lebart, F. Hubert, C. Boiteau, S. Venteo, C. Roustan, and Y. Benyamin, 2004. Biochemical characterization of the L-plastin-actin interaction shows a resemblance with that of α-actinin and allows a distinction to be made between the two actin-binding domains of the molecule. *Biochemistry*, 43(9):2428–2437.

[122] A. Rzadzinska, M. Schneider, K. Noben-Trauth, J. Bartles, and B. Kachar, 2005. Balanced levels of espin are critical for stereociliary growth and length maintenance. *Cell Motil Cytoskel*, 62(3):157–165.

[123] L. Tilney, P. Connelly, L. Ruggiero, K. Vranich, and G. Guild, 2003. Actin filament turnover regulated by cross-linking accounts for the size, shape, location, and number of actin bundles in Drosophila bristles. *Mol Biol Cell*, 14(10):3953–3966.

[124] S. Mukhina, Y.-L. Wang, and M. Murata-Hori, 2007. α-actinin is required for tightly regulated remodeling of the actin cortical network during cytokinesis. *Dev Cell*, 13(4):554–565.

[125] K. Moriyama and I. Yahara, 1999. Two activities of cofilin, severing and accelerating directional depolymerization of actin filaments, are affected differentially by mutations around the actin-binding helix. *Embo J*, 18(23):6752–6761.

[126] K. Broschat, A. Weber, and D. Burgess, 1989. Tropomyosin Stabilizes the Pointed End of Actin Filaments by Slowing Depolymerization. *Biochemistry*, 28(21):8501–8506.

[127] S. Ono and K. Ono, 2002. Tropomyosin inhibits ADF/cofilin-dependent actin filament dynamics. *J Cell Biol*, 156(6):1065–1076.

[128] N. Medeiros, D. Burnette, and P. Forscher, 2006. Myosin II functions in actin-bundle turnover in neuronal growth cones. *Nat Cell Biol*, 8(3):215–226.

[129] R. Ishikawa, T. Sakamoto, T. Ando, S. Higashi-Fujime, and K. Kohama, 2003. Polarized actin bundles formed by human fascin-1: their sliding and disassembly on myosin II and myosin V in vitro. *J Neurochem*, 87(3):676–685.

[130] L. Haviv, D. Gillo, F. Backouche, and A. Bernheim-Groswasser, 2008. A cytoskeletal demolition worker: Myosin II acts as an actin depolymerization agent. *J Mol Biol*, 375(2):325–330.

[131] S. Kron and J. Spudich, 1986. Fluorescent actin filaments move on myosin fixed to a glass surface. *Proc Natl Acad Sci USA*, 83(17):6272–6276.

[132] M. Steinmetz, D. Stoffler, S. Muller, W. Jahn, B. Wolpensinger, K. Goldie, A. Engel, H. Faulstich, and U. Aebi, 1998. Evaluating atomic models of F-actin with an undecagold-tagged phalloidin derivative. *J Mol Biol*, 276(1):1–6.

[133] S. Huang, R. Robinson, L. Gao, T. Matsumoto, A. Brunet, L. Blanchoin, and C. Staiger, 2005. Arabidopsis VILLIN1 generates actin filament cables that are resistant to depolymerization. *Plant Cell*, 17(2):486–501.

[134] A. Michelot, J. Berro, C. Guerin, R. Boujemaa-Paterski, C. J. Staiger, J.-L. Martiel, and L. Blanchoin, 2007. Actin-filament stochastic dynamics mediated by ADF/cofilin. *Curr Biol*, 17(10):825–833.

[135] O. L. Mooren, T. I. Kotova, A. J. Moore, and D. A. Schafer, 2009. Dynamin2 GTPase and Cortactin Remodel Actin Filaments. *J Biol Chem*, 284(36):23995–24005.

[136] P. Fernandez, L. Heymann, A. Ott, N. Aksel, and P. A. Pullarkat, 2007. Shear rheology of a cell monolayer. *New J Phys*, 9:419.

[137] P. Fernandez, P. Pullarkat, and A. Ott, 2006. A master relation defines the nonlinear viscoelasticity of single fibroblasts. *Biophys J*, 90(10):3796–3805.

[138] B. Hinner, M. Tempel, E. Sackmann, K. Kroy, and E. Frey, 1998. Entanglement, elasticity, and viscous relaxation of actin solutions. *Phys Rev Lett*, 81(12):2614–2617.

[139] M. Gardel, J. Shin, F. C. MacKintosh, L. Mahadevan, P. Matsudaira, and D. Weitz, 2004. Elastic Behavior of cross-linked and bundled actin networks. *Science*, 304(5675):1301–1305.

[140] J. Xu, Y. Tseng, and D. Wirtz, 2000. Strain hardening of actin filament networks - Regulation by the dynamic cross-linking protein α-actinin. *J Biol Chem*, 275(46):35886–35892.

[141] K. Kroy and J. Glaser, 2007. The glassy wormlike chain. *New J Phys*, 9:416.

[142] F. Gittes, B. Mickey, J. Nettleton, and J. Howard, 1993. Flexural Rigidity of Microtubules and Actin Filaments Measured from Thermal Fluctuations in Shape. *J Cell Biol*, 120(4):923–934.

[143] S. Kaufmann, J. Käs, W. Goldmann, E. Sackmann, and G. Isenberg, 1992. Talin anchors and nucleates actin filaments at lipid membranes - A direct demonstration. *FEBS Lett*, 314(2):203–205.

[144] O. Kratky and G. Porod, 1949. Roentgenuntersuchung geloester Fadenmolekuele. *Recl Trav Chim Pay B*, 68(12):1106–1122.

[145] O. Hallatschek, E. Frey, and K. Kroy, 2007. Tension dynamics in semiflexible polymers. I. Coarse-grained equations of motion. *Phys Rev E*, 75(3):031905.

[146] M. Doi and S. F. Edwards, 1988. The Theory of Polymer Dynamics. *Oxford University Press*.

[147] P. De Gennes, 1971. Reptation of a Polymer Chain in the Presence of Fixed Obstacles. *J Chem Phys*, 55(2):572–579.

[148] D. C. Morse, 1998. Viscoelasticity of concentrated isotropic solutions of semiflexible polymers. 2. Linear response. *Macromolecules*, 31(20):7044–7067.

[149] H. Hinsch, J. Wilhelm, and E. Frey, 2007. Quantitative tube model for semiflexible polymer solutions. *Eur Phys J E*, 24(1):35–46.

[150] N. W. Tschoegl, 1989. The phenomenological theory of linear viscoelastic behavior. *Springer*.

[151] M. Wilhelm, 2002. Fourier-Transform rheology. *Macromol Mater Eng*, 287(2):83–105.

[152] R. M. Christensen, 1982. Theory of viscoelasticity: an introduction. *Academic Press*, New York(2nd edition).

[153] S. Ganeriwala and C. Rotz, 1987. Fourier transform mechanical analysis for determining the nonlinear viscoelastic properties of polymers. *Polym Eng Sci*, 27(2):165–178.

[154] R. H. Ewoldt, A. E. Hosoi, and G. H. McKinley, 2008. New measures for characterizing nonlinear viscoelasticity in large amplitude oscillatory shear. *J Rheol*, 52(6):1427–1458.

[155] A. C. Pipkin, 1972. Lectures on viscoelasticity theory. *Springer*, New York.

[156] P. De Gennes, 1979. Scaling Concepts in Polymer Physics. *Cornell University Press*.

[157] H. Isambert and A. Maggs, 1996. Dynamics and rheology of actin solutions. *Macromolecules*, 29(3):1036–1040.

[158] K. Schmoller, P. Fernández, R. Arevalo, D. Blair, and A. Bausch, 2010. Cyclic hardening in bundled actin networks. *Nat Commun*, 1(9):134.

[159] H. Kang, Q. Wen, P. A. Janmey, J. X. Tang, E. Conti, and F. C. MacKintosh, 2009. Nonlinear Elasticity of Stiff Filament Networks: Strain Stiffening, Negative Normal Stress, and Filament Alignment in Fibrin Gels. *J Phys Chem B*, 113(12):3799–3805.

[160] C. Storm, J. J. Pastore, F. C. MacKintosh, T. C. Lubensky, and P. A. Janmey, 2005. Nonlinear elasticity in biological gels. *Nature*, 435(7039):191–194.

[161] R. Tharmann, M. M. A. E. Claessens, and A. R. Bausch, 2006. Micro- and macrorheological properties of actin networks effectively cross-linked by depletion forces. *Biophys J*, 90(7):2622–2627.

[162] D. Morse, 1998. Viscoelasticity of tightly entangled solutions of semiflexible polymers. *Phys Rev E*, 58(2):1237–1240.

[163] P. Onck, T. Koeman, T. V. Dillen, and E. van der Giessen, 2005. Alternative explanation of stiffening in cross-linked semiflexible networks. *Phys Rev Lett*, 95(17):178102.

[164] C. Heussinger and E. Frey, 2006. Floppy modes and nonaffine deformations in random fiber networks. *Phys Rev Lett*, 97(10):105501.

[165] P. Fernandez, S. Grosser, and K. Kroy, 2009. A unit-cell approach to the nonlinear rheology of biopolymer solutions. *Soft Matter*, 5(10):2047–2056.

[166] K. Kroy, 2008. Dynamics of wormlike and glassy wormlike chains. *Soft Matter*, 4(12):2323–2330.

[167] P. Sollich, F. Lequeux, P. Hebraud, and M. Cates, 1997. Rheology of soft glassy materials. *Phys Rev Lett*, 78(10):2020–2023.

[168] L. Cipelletti and L. Ramos, 2005. Slow dynamics in glassy soft matter. *J Phys-Condens Mat*, 17(6):R253–R285.

[169] R. Piazza, 2004. Protein interactions and association: an open challenge for colloid science. *Curr Opin Colloid In*, 8(6):515–522.

[170] R. Stinchcombe and M. Depken, 2002. Marginal scaling scenario and analytic results for a glassy compaction model. *Phys Rev Lett*, 88(12):125701.

[171] C. Semmrich, T. Storz, J. Glaser, R. Merkel, A. R. Bausch, and K. Kroy, 2007. Glass transition and rheological redundancy in F-actin solutions. *Proc Natl Acad Sci USA*, 104(51):20199–20203.

[172] P. A. Janmey, S. Hvidt, J. Käs, D. Lerche, A. Maggs, E. Sackmann, M. Schliwa, and T. P. Stossel, 1994. The Mechanical Properties of Actin Gels - Elastic Modulus and Filament Motions. *J Biol Chem*, 269(51):32503–32513.

[173] M. Tempel, G. Isenberg, and E. Sackmann, 1996. Temperature-induced sol-gel transition and microgel formation in α-actinin cross-linked actin networks: A rheological study. *Phys Rev E*, 54(2):1802–1810.

[174] O. Lieleg and A. R. Bausch, 2007. Cross-linker unbinding and self-similarity in bundled cytoskeletal networks. *Phys Rev Lett*, 99(15):158105.

[175] F. Rivero, R. Furukawa, M. Fechheimer, and A. Noegel, 1999. Three actin cross-linking proteins, the 34 kDa actin-bundling protein, α-actinin and gelation factor (ABP-120), have both unique and redundant roles in the growth and development of Dictyostelium. *J Cell Sci*, 112(16):2737–2751.

[176] B. Fabry and J. Fredberg, 2003. Remodeling of the airway smooth muscle cell: are we built of glass? *Resp Physiol Neurobi*, 137(2-3):109–124.

[177] X. Trepat, G. Lenormand, and J. J. Fredberg, 2008. Universality in cell mechanics. *Soft Matter*, 4(9):1750–1759.

[178] S. Amelinckx, X. Zhang, D. Bernaerts, X. Zhang, V. Ivanov, and J. Nagy, 1994. A Formation Mechanism for Catalytically Grown Helix-Shaped Graphite Nanotubes. *Science*, 265(5172):635–639.

[179] I. Couzin, J. Krause, N. Franks, and S. Levin, 2005. Effective leadership and decision-making in animal groups on the move. *Nature*, 433(7025):513–516.

[180] I. Riedel, K. Kruse, and J. Howard, 2005. A self-organized vortex array of hydrodynamically entrained sperm cells. *Science*, 309(5732):300–303.

[181] A. Czirok and T. Vicsek, 2006. Collective behavior of interacting self-propelled particles. *arXiv*, cond-mat.stat-mech.

[182] R. Simha and S. Ramaswamy, 2002. Hydrodynamic fluctuations and instabilities in ordered suspensions of self-propelled particles. *Phys Rev Lett*, 89(16):058101.

[183] A. Baskaran and M. C. Marchetti, 2008. Enhanced diffusion and ordering of self-propelled rods. *Phys Rev Lett*, 101(26):268101.

[184] V. Schaller, C. Weber, C. Semmrich, E. Frey, and A. R. Bausch, 2010. Polar patterns of driven filaments. *Nature*, 467(7311):73–77.

[185] V. Schaller, C. Weber, E. Frey, and A. R. Bausch, 2011. Polar pattern formation: hydrodynamic coupling of driven filaments. *Soft Matter*, 7(5):3213–3218.

List of Publications

- C. Semmrich, K.M. Schmoller, A.R. Bausch (2011). *Slow down of actin depolymerization by cross-linking molecules*, Journal of Structural Biology, 173(2), 350-357
- C. Semmrich, A.R. Bausch (2011). *Protein crystals: How the weak become strong*, Nature Materials, 9(4), 293-295
- V. Schaller, C. Weber, C. Semmrich, E. Frey, A.R. Bausch (2010). *Polar patterns of driven filaments*, Nature, 467(7311), 73-77
- O. Lieleg, K.M. Schmoller, K.R. Purdy Drew, M.M.A.E. Claessens, C. Semmrich, L. Zheng, J. Bartles, A.R. Bausch (2010). *Structural and Viscoelastic Properties of Actin Networks Formed by Espin or Pathologically Relevant Espin Mutants*, ChemPhysChem, 10(16), 2813-2817
- C. Semmrich, R.J. Larsen, A.R. Bausch (2008). *Nonlinear mechanics of entangled F-actin solutions*, Soft Matter, 4(8), 1675-1680
- M.M.A.E. Claessens, C. Semmrich, L. Ramos, A.R. Bausch (2008). *Helical twist controls the thickness of F-actin bundles*, PNAS, 105(26), 8819-8822
- C. Semmrich, T. Storz, J. Glaser, R. Merkel, A.R. Bausch, K. Kroy (2007). *Glass Transition and Rheological Redundancy in F-Actin Solutions*, PNAS, 104(51), 20199-20203
- O. Lieleg, M. López-García, C. Semmrich, J. Auernheimer, H. Kessler, A.R. Bausch (2007). *Specific Integrin Labeling in Living Cells Using Functionalized Nanocrystals*, Small, 3(9), 1560-1565

Danksagung

Zuletzt möchte ich noch allen ganz herzlich danken, die zum Gelingen dieser Arbeit beigetragen haben:

Allen voran gilt mein Dank meinem Doktorvater Andreas Bausch, der nicht nur diese Arbeit mit einer stets offenen Tür hervorragend betreut hat, sondern mich auch im Hinblick auf meine fachliche, berufliche und persönliche Weiterentwicklung kontinuierlich gefördert hat. Seine außerordentliche Motivationsfähigkeit hat über so manchen Zweifel hinweg geholfen.

Ein großer Dank geht auch an die aktuellen und ehemaligen Mitglieder der Zell-/Zytoskelettgruppe für die angenehme und hilfsbereite Atmosphäre und die produktiven Diskussionen in den wöchentlichen Gruppentreffen.

Auch möchte ich mich bei allen Kooperationspartnern bedanken, die zusammen mit mir an den unterschiedlichen Projekten gearbeitet haben: Klaus Kroy und Jens Glaser, die mit dem Modell des glassy worm-like chain den theoretischen Hintergrund für die nichtlinearen Daten geliefert haben, danke ich für die hilfreichen Diskussionen. G. Wong und seiner Arbeitsgruppe möchte ich für die Möglichkeit danken, eine Strahlzeit mit ihnen erleben zu dürfen, um so einige Kniffe und Tricke für den Umgang mit SAXS-Proben zu erlernen. Kirstin und Tommy danke ich dabei besonders für die Beantwortung vieler Fragen zum Thema fibre diffraction und das Überlassen ihrer mathematica-Skripte. Mireille danke ich für die hervorragende Zusammenarbeit beim Thema der finiten Bündeldicken und den ersten Versuchen, unsere Streudaten zu erklären. Bei Kurt möchte ich mich für das außerordentliche teamwork bedanken, mit dem die Experimente zur Depolymerisationskinetik durchgeführt wurden. Ohne sein Geschick, die Diffusionskammern mit einer Unmenge an Vakuumfett dann doch noch abzudichten, wären wir noch sehr viel länger am Mikroskop gesessen.

Die Streuexperimente wären nicht ohne Mithilfe anderer möglich gewesen: Andreas, Mireille, Kurt und Schuppi danke ich für Hilfe bei der Vorbereitung der Proben und der Durchführung der Strahlzeiten am ESRF. Den Wissenschaftlern an der beamline ID02, Emanuela Di Cola und Michael Sztucki, danke ich für die Hilfe vor Ort und die Skripte für die nachträgliche Änderung des Strahlmittelpunkts.

Den TA's Gabi, Karin, Monika und Dani danke ich nicht nur für die hervorragende Präparation von Aktin und der verschiedenen aktinbindenden Proteine, sondern v.a. auch für die Aufrechterhaltung der für die tägliche Laborarbeit nötigen Ordnung und Sauberkeit. Den Sekretärinnen Iris, Nicole und Veronika danke ich dafür, dass sie soweit wie möglich allein den Kampf mit der Bürokratie führen und uns Doktoranden damit den Rücken freihalten.

Meinen Bürokollegen danke ich für einen unvergleichlichen Büroalltag: Jona, mit dem man zusammen den Nichten und Neffen Sandmännchenlieder vorsingen kann. Simone mit ihrer Begeisterung für Extremsport, was bei ihr Rodeln ausdrücklich mit

einschließt. Und Volker, der mit seinem wahrscheinlich unendlichen Fuhrpark als das wahre Mobbingopfer viel zu leiden hatte.

Felix und Melanie möchte ich nicht nur für die vielen hilfreichen Diskussionen und Anregungen, sondern auch für die langandauernde, gute Gemeinschaft am Lehrstuhl und im Central Perk danken. Es tut gut, wenn wenigstens ihr meine Geschichten aus "der guten alten Zeit" noch kennt.

Mein großer Dank gilt auch allen anderen Mitgliedern des Biophysik-Lehrstuhl-Clusters E22/E27 für die einzigartige Arbeitsatmosphäre und große Hilfsbereitschaft.

Ein großes Dankeschön geht an meine Eltern und Schwestern, die mir mit ihrer jahrelangen Unterstützung ein sorgenfreies Studium ermöglichten und immer wieder zeigten, dass es auch ein Leben neben der Physik gibt.

Meinem Mann Michael danke ich für so vieles, nicht nur für das sorgsame Korrekturlesen dieser Doktorarbeit, die so gar nicht in sein Themengebiet passt, und für viele hilfreiche Diskussion darüber. Mein Dank gilt im Besonderen der liebevollen Unterstützung während der gesamten Doktorarbeit und v.a. der letzten Schreibphase.